Incoherent Neutron Scattering Studies of Select Inorganic Systems

I. Nuclear Momentum Measurements of Multiple Masses

II. The Dynamics of Coordinated Ammonia in Zeolite A

Andrew G. Seel

A thesis submitted to the University of Oxford for the degree of Doctor of Philosophy

Supervisor

Prof. Peter P. Edwards FRS

Inorganic Chemistry Laboratory

The work described in this thesis was carried out in the Inorganic Chemistry Laboratory, University of Oxford from October 2008 until May 2012, under the supervision of Professor Peter P. Edwards. All of the work is my own unless otherwise stated, and has not been submitted previously for any degree at this or any other university.

Andrew G. Seel

May 2012

"Getting an education was a bit like a communicable sexual disease. It made you unsuitable for a lot of jobs and then you had the urge to pass it on."

Terry Pratchett, Hogfather

This thesis is dedicated to my parents. As ever there are no words, so here's to the end of a long but wonderful education, at least officially. Thank you.

Further inspiration for tackling this thesis is provided in Appendix D.

Acknowledgements

Prof. Peter Edwards is gratefully acknowledged for both allowing me to work in his group, and for giving me enough rope with which to tie myself to ISIS. I've been rather fond of working in his group over the last few years, and could never leave without also extending my heartfelt thanks to Linda Webb for all she's done to help, ease and generally smooth-over everyone's time here.

This thesis, and indeed the path I'm traipsing along in neutron science, could not have come to (eventual) light without the support and mentoring of instrument scientists at ISIS. Dr. Jerry Mayers, Prof. Felix Fernandez-Alonso and Dr. Timmy Ramirez-Cuesta have always been willing to teach a chemist about neutrons (and gently mock my clothing and general image of course) and I am not only staggered by their patience and support, but look forward to working with them in the future. In addition Dr. John Tomkinson, Dr. Victoria Garcia-Sakai, Dr. Stewart Parker and Dr. John Taylor are warmly thanked for their input and help.

Next up come the members of the Edwards Group, generally past but also some present. It has become an accepted fact that fellow DPhil students are more help, let alone support, than postdocs, and we have certainly proven this over the years. Dr. Kate Ryan should come back from Argonne *asap*, Philippe and Henry have been pretty damned good 'yearmates' and conference-buddies, but also I can (fleetingly) smile at having worked with the likes of Katie, Liang, Laura, Scott, Josh, Nazaneen and a whole fleet of Part IIs (particularly Ciaran and Mark). Let's face it, I've been a blast.

For her proofreading skills, advice and general awesomeness I would like to thank Dr. Sylvia McLain. My examiners, Dr. Andrew Goodwin and Prof. Neil Skipper, are also thanked for their input into this final version, and for a very enjoyable viva (3 hours to the minute was also quite impressive). Prof. Bill David has never been unsupportive of my love of neutron science, even though I have taken the Dynamics route, and he and Dr. Martin Owen-Jones are thanked for their part in my doctorate. Essential too has been the support of the ISIS technical staff, in particular Chris Goodway, Mark Kibble, Steve Cox, Dominic Chan and Jon Bones.

Dr. Michelle Ceriotti is gratefully acknowledged for calculations on LiF, and I look forward to future collaboration between DINS and theory. A theoretician with hearty respect for experimentation is hard to find! Dr. Matthew Lodge is thanked both for actually coming to and engaging in group lunches and for synthesis of the $Li(NH_3)_4$ samples. Dr. Asel Sartbaeva is acknowledged for providing the SiGNa and SiGNaH samples and for initiating the zeolite INS.

I refuse to write a thesis without acknowledging Moyas. Although the staff will likely never know of this, few of the Edwards group could have got through the (not so occasional) setbacks of their research without Moyas' cocktails and chips, and I *really* need to thank them for creating the Black Primordial Soup for us. Gothtastic.

You work, you strive and occasionally you cry with anger or frustration. Throughout all of this I have had my family, and it is never trite to state that I couldn't have even *begun* this thesis without them, let alone survived the numerous setbacks and detrimental influences. I am so astonishingly lucky to be able to write this, and with the greatest love in the world I thank my mother and father for supporting me through everything. Eight years as a chemist in training; we're nearly done! Thank you.

Abstract

Incoherent Neutron Scattering Studies of Select Inorganic Systems

Andrew G. Seel

Submitted for the degree of Doctor of Philosophy in Trinity Term 2012

Spectroscopic measurements are detailed within this thesis, utilising incoherent neutron scattering to examine the dynamics of various condensed-matter systems, from nanosecond to sub-femtosecond timescales. The body of this work is divided into two distinct areas of research.

I. Nuclear Momentum Measurements of Multiple Masses

Deep inelastic neutron scattering (DINS) is used to probe the nuclear momentum distributions and kinetic energies of individual atomic species in sodium hydride (both in bulk and as nanoparticulates within a silica matrix), enriched lithium-7 fluoride and lithium tetra-ammoniate. Extension of DINS to examine heavier (M>4amu) nuclei is detailed, accomplished by the application of a simple stoichiometric fixing technique within the standard DINS theory and analysis protocols. The validity and accuracy of such simultaneous measurements are discussed.

II. The Dynamics of Coordinated Ammonia in Zeolite A

Inelastic neutron scattering (INS) and quasielastic neutron scattering (QENS) are utilised in the examination of vibrational and stochastic dynamics of the ammonia molecule, as coordinated to the internal surface of a zeolite host. Both sodium- and copper-exchanged forms of zeolite-A are studied, with proton-weighted, low energy phonon-modes and rotational processes being observed and assigned.

Extended Abstract

Incoherent Neutron Scattering Studies of Select Inorganic Systems

I. Nuclear Momentum Measurements of Multiple Masses

II. The Dynamics of Coordinated Ammonia in Zeolite A

Andrew G. Seel

Submitted for the degree of Doctor of Philosophy in Trinity Term 2012

This thesis begins with an overview of neutron scattering as a tool for the study of condensed matter systems in *Chapter 1*, detailing the various forms of spectroscopy able to be performed by the incoherent scattering of incident neutrons. The historical overviews of both the emergence of deep-inelastic neutron scattering, and the application of neutron spectroscopy to zeolite-host systems are also detailed, with emphasis laid throughout on the applications of such from a chemical as well as physical perspective.

Chapter 2 details the theoretical framework of neutron spectroscopy, beginning with a short derivation of the scattering law, $S(\mathbf{q},\omega)$, and intermediate correlation function, $I(\mathbf{q},t)$, for the scattering of a neutron from a single atomic nucleus. From this, the various forms of $S(\mathbf{q},\omega)$ are discussed for each spectroscopic technique utilised within this thesis, namely inelastic neutron scattering (INS), quasielastic neutron scattering (QENS) and deep inelastic neutron scattering (DINS). The latter section of this chapter presents brief details of the individual instruments used for the various spectroscopic techniques, their setup and parameters encountered within the body of the thesis.

The chemistry and synthetic procedures (where appropriate) for each of the systems studied within this work are presented in *Chapter 3*. These systems are the sodium and copper exchanged forms of zeolite A, NaH, the gel encaspulates SiGNa and SiGNaH, LiF and $Li(NH_3)_4$.

Results from studies on the application of DINS to multiple masses, where $M >$ 4amu, are given in *Chapter 4*. Initially, the justification of stoichiometric fixing as an alteration to the standard analysis procedures of DINS is discussed, detailing how this arises from the Impulse Approximation in the count-rate of an indirect geometry time-of-flight spectrometer such as VESUVIO.

A study of NaH, nanoparticulate NaH in a silica gel (SigNaH) and sodium metal within silica gel (SiGNa) is then detailed, with both the proton momentum distri-

butions, proton mean kinetic energies and heavy mass mean kinetic energies being measured. It is shown that there exists a difference in the proton momentum distribution in NaH when on the nanoscale, with the mean kinetic energies being in agreement with that calculated previously from INS measurements. Momentum widths for Na are seen to demonstrate differences in the three samples, to be in agreement with a previous DINS study of metallic Na and agree with a chemical understanding of the systems.

The accuracy of simultaneous, multiple-mass measurements on VESUVIO is then pursued in a study of ^{7}LiF, with the momentum widths of ^{7}Li and ^{19}F being determined at temperatures in the range 4K-500 K. These are compared to those calculated by a quasiharmonic density functional approach, and are seen to be within 5% of the calculated values in all cases.

The proton momentum distributions and proton mean kinetic energies in the four solid phases of $Li(NH_3)_4$ are then determined by DINS, and are seen to exhibit no discernible change, even in the radial momentum distributions. In addition to this, the form of the momentum distribution is seen to vary from that of a harmonic system only insofar as a kurtosis in the momentum distribution, something that is perhaps strange considering the molecular nature of the solid (in terms of NH_3 units). Planned comparative measurements on NH_3 itself were not possible at the time of writing, due to unforeseen problems at the neutron source, and are scheduled for the near future. *Chapter 4* concludes with a brief discussion of the

current state of DINS.

Chapter 5 details spectroscopic neutron studies of NH_3 coordinated at low concentration to the internal surface of zeolite A, to both the Na- and Cu-exchanged forms of the zeolite. Initially INS measurements are presented for $NaA{\cdot}4NH_3$, detailing vibrational processes in the range 0-150 meV. Three distinct structural regions are witnessed in the spectra, and are assigned by comparison of modelling of phonon displacements at the level of fully periodic density functional theory and subsequent simulation of the INS spectra. A similar approach is then taken for the Cu-exchanged form of the zeolite. The relative energies of molecular bending, stretching, tilting and libration are determined in each system. The greatest discrepancy between measured and modelled system in each case is in the amplitude of the librational displacement of the NH_3 molecule, and reasoning for this is discussed. *Chapter 5* continues with a study of longer timescale processes in the NaA-NH_3 system, examined by QENS measurements. Noticeable quasielastic broadening is witnessed above 60 K, and is demonstrated to be a rotational process, or localised molecular diffusion. The activation energy for this process is seen to fit an Arrhenius model, though the calculated elastic incoherent structure factor is seen to differ from that of a 3-fold rotor.

Conclusions are drawn at the end of each section of this thesis, but are collected in brief in *Chapter 6*.

Contents

Chapter 1

Introduction

"The most merciful thing in the world, I think, is the inability of the human mind to correlate all its contents."

H.P. Lovecraft, *The Call of Cthulhu*

Chemical research is often born of a firm concept and develops within a concerted plan of action. Yet one of the most fantastically freeing aspects of scientific research (compared with more nebulous kinds, such as literary treatise) is that at some point a scientist can ask "what happens if we try *this*", and occasionally in the excited aftermath of physical data all thoughts of concept and plans are thrown to the wind. This is the reason given for the direction of this thesis being very much divided in two.

Initially this thesis was designed to study the manner in which ammonia, NH_3, interacts with a zeolite host at low concentrations, through an examination of its

short and longer timescale molecular dynamics as probed by neutron spectroscopy. To this end, data will be presented across neutron energy transfer ranges of a few micro-electronvolts through to tens of milli-electronvolts. Appreciably into the course of this DPhil, however, some measurements were taken at energy transfers significantly higher than this, of the order of several and tens of electronvolts. Whilst those initial measurements were not particularly fruitful for the zeolite systems investigated, a fresh impetus entered into the research, and the possible application of this 'deep-inelastic neutron scattering' to chemical systems was subsequently pursued in conjunction with the zeolite/ammonia project.

In deference to convention this chapter will give an historical overview of neutron spectroscopy, with emphasis on its application to zeolite systems. A relevant theoretical backdrop, crucial for the interpretation of results in this thesis, is left for the following chapter. The emergence and current extent of deep-inelastic scattering as a technique is also included in this chapter.

1.1 The Neutron as a Spectroscopic Probe

The physical discovery of the neutron was made by Chadwick in 1935, for which he was awarded the Nobel prize in physics, amidst additional experimental work by Joliot and Curie.[1] Previously to this the theoretical existence of such a neutrally charged particle being part of the atomic nucleus had been made by the likes of Rutherford and Ivanenko. One of the earliest pioneers of the interaction of neutrons

with matter, amongst a truly phenomenal number of fundamental achievements, was Fermi [2] (specifically his work on 'slow' neutrons contributed to his Nobel Prize in physics in 1938). Yet it was only with the advent of nuclear reactors that the application of neutrons to condensed matter was truly begun. Work at Oak Ridge National Laboratory (U.S.A.)[1] in the 1950s earned Schull and Brockhouse the most recent Nobel Prize awarded for neutron science (1994) [3], for pioneering the use of thermal neutrons to probe material structure and dynamics respectively.

The preceding sentence encapsulates the true power of thermal neutrons as a probe for condensed matter: the ability to examine both structure *and* dynamics, and to do so simultaneously (though it should be noted that modern neutron instruments are designed to study very specific facets within those two classifications). In order to study the structure of condensed matter a probe is needed that has a wavelength of the order of the interatomic spacing in the system, and to examine dynamics of a system the probe must have frequencies comparable to those of the dynamical process being studied. The archetypal spectroscopic probe can be said to be the photon, with X-rays having suitable wavelengths for crystallographic analyses, and infra-red/gamma radiation having frequencies suitable for studying vibrational dynamics. Taking the energy E of neutron to be

$$E = \frac{\hbar^2 k^2}{2m_n} = \frac{h^2}{2m\lambda^2}, \tag{1.1}$$

[1]Oak Ridge National Laboratory, 1 Bethel Valley Road, Oak Ridge, TN 37831, U.S.A.

where $\mathbf{k}$ is the wavevector, λ the de Broglie wavelength and m_n the mass of the neutron. Taking $m_n = 9.383 \times 10^8$ eV, and inserting into equation 1.1, it can be seen that

$$\frac{\hbar^2}{2m_n} = 2.08\,\text{meV}\text{Å}^2, \tag{1.2}$$

thus neutrons with wavevectors $\mathbf{k}$ of a few Å^{-1} are of energies a few meV, an energy concomitant with that of lattice vibrations in condensed matter [4, 5].

Of course it should be addressed that whilst neutrons *can* simultaneously examine structure and dynamics, whether there are tangible benefits of neutrons for a chemist over the use of various photon-based spectroscopies? Particularly as often a specific question pertaining to structure *or* dynamical processes is of interest. This thesis itself is concerned specifically with spectroscopic rather than crystallographic measurements, and indeed a problem arises in some of the data presented due to 'crystallographic' measurements being present in conjunction with spectroscopic information.

At an elementary level, the neutron as a chargeless particle is able to penetrate deep into matter before being scattered, not being dependant on the electron density within a sample, but rather on the strong nuclear force which is of incredibly short range [4]. This short range does, however, result in weak scattering, orders of magnitude weaker than for X-rays for example, and thus much larger samples

are required for neutron scattering investigations. Photon and electron scattering techniques involve interaction with electrons in the sample, and thus penetrate much less distance into a sample before being scattered. This is particularly true for the electron, itself a charged particle. Neutrons may therefore be deemed ideal for investigating bulk properties of a sample of interest, or for examining species absorbed within a zeolite framework, rather than being weighted towards the external surface. A general comparison of vibrational spectroscopy with neutrons and light will be given in section 1.4, and for further discussion the reader is directed to references [6, 7].

One of the greatest benefits to using neutrons is perhaps also the least understood fundamentally (despite the inherent irony of this, it has not hindered neutron scattering research as will be shown in chapter 2) and that is the difference in scattering magnitudes which occur throughout the periodic table. It is again convenient to draw comparisons to photon-spectroscopies at this juncture, specifically X-ray scattering cross sections. A full description of what is meant by 'neutron scattering cross-sections' will be presented in chapter 2, but here it is sufficient to say that a scattering cross-section is a measure of how strongly an element/isotope scatters a particular form of incident radiation.

The schematic of figure 1.1 shows the scattering cross-sections for a selection of element isotopes in the periodic table and illustrates the fundamental difference in the way in which neutrons and light scatter from a system. It can be seen that in

the case of X-rays, there is a linear increase in total scattering cross-section with electron density, i.e. a monotonic increase across the periodic table. This is due to the principal interaction of X-rays with matter being electromagnetic in nature, whereby the electron charge of a species interacts with the oscillating electric and magnetic fields of the incident X-ray.

A noticeable difference is seen when moving to neutron total scattering cross

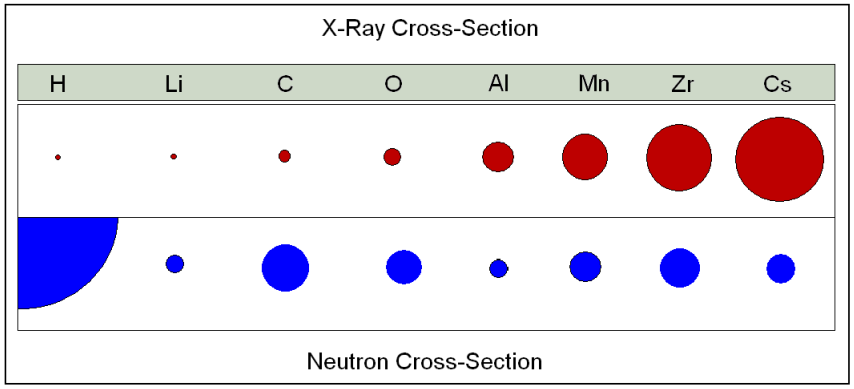

Figure 1.1: Diagram of neutron verses X-ray total scattering cross sections for example elemental species (principal isotope for each) [8]

sections, presented in figure 1.1. This scattering cross-section can be subdivided into cross-sections for coherent and incoherent scattering (*cf.* 2.2.1), but for now a simple comparison of total scattering of X-rays and neutrons is sufficient to exemplify the principal difference: there is no clear pattern for the scattering power of elements throughout the periodic table. Certainly the variance is not monotonic with atomic number, Z, as is the case for X-rays, and also distinctly different cross-sections can occur between elemental isotopes, as will be demonstrated by

hydrogen and deuterium in table 1.1. Whilst the mechanism for the electromagnetic interaction of X-rays with matter is well understood, the nucleon-nucleon interaction between a neutron and the nucleus of an atom involves the nuclear strong force, for which no such physical description exists. The elegant method for side-stepping a lack of mathematical description for the strong force is reproduced in the following chapter. What can immediately be gleaned from figure 1 as a whole is that, unlike for X-rays, neutrons are able to scatter from light elements just as well as (and in the case of hydrogen far more intensely than) heavier elements.

A much greater strength of neutron science is demonstrated when the concept of scattering is subdivided into that of *incoherence* and *coherence*. Table 1.1 lists the scattering cross sections for the same elements included in figure 1, but in this case the total scattering cross section, σ_{tot}, has been separated into its constituent coherent, σ_c and incoherent, σ_i, cross- sections

$$\sigma_{tot} = \sigma_c + \sigma_i. \tag{1.3}$$

There is also a finite possibility that a nucleus will absorb rather than scatter an incident neutron, as determined by the absorption cross-section, σ_a. This cross-section varies with incident neutron energy, and is presented as part of table 1.1 for 2200 ms^{-1} neutrons [9].

Table 1.1: *Select coherent (σ_c), incoherent (σ_i), total (σ_{tot}) and absorption (σ_a) neutron scattering cross-sections (barn)*

Isotope	σ_c	σ_i	σ_{tot}	σ_a
H	1.76	80.27	82.03	0.33
D	5.59	2.05	7.64	0.33
^{4}He	1.34	0.00	1.34	0.00
^{7}Li	0.62	0.78	1.40	0.045
^{14}N	11.03	0.5	11.51	1.90
^{27}Al	1.495	0.01	1.50	0.23
^{63}Cu	5.20	0.006	5.206	4.50

A formal description of incoherence and coherence is not required at this stage, and a qualitative description can be given in order to understand the difference and importance of each. Firstly, coherent scattering encompasses interference effects from scattering from other nuclei in the system, thus resulting in a geometrical dependance. Incoherent scattering, conversely, can be thought of as occurring from a single scattering centre with no interference effects from separate nuclei.

It is immediately apparent that for structural analysis, or to put it in a more fundamental light, a crystallographic examination of a system, it is the coherent scattering cross section that is of all importance. Incoherent scattering results in a large background for such analyses and is thus detrimental. From table 1.1, therefore, it can be understood why it is beneficial (and often a necessity) for hydrogenous compounds to be deuterated for neutron crystallography.

This thesis is concerned with incoherent spectroscopic measurements (where spec-

troscopy will henceforth be used to denote an examination of inelastic processes[2]), and thus it is the incoherent scattering cross-section that relates to the intensity of detected neutrons. The extremely high incoherent cross-section for hydrogen will thus dominate a spectrum. The greatest benefit of neutron spectroscopy for (most) systems in this thesis can be immediately elucidated, as it enables the isolation of the dynamics of hydrogen-containing molecules amidst a hydrogen-free framework.

1.2 The Kinematic Range of Neutron Spectroscopy

The wavevector or de Broglie wavelength of a neutron was related to its energy in equation 1.1. Whilst in a spectroscopic measurement it is the change in neutron energy that is of principal interest, instrument design is such that often incident neutrons need to be within a specific energy range. The relevant instrumentation used for this thesis are discussed in section 2.2, but in general neutrons can be broadly categorised by their energy thus

	E(meV)
$Cold$	$0.1 - 10$
$Thermal$	$10 - 100$
Hot	$100 - 500$
$Epithermal$	> 500

[2]Coherent inelastic processes are not examined in this thesis

The above nomenclature does not serve as standard definition, but has been reproduced following the classifications of Lovesey [4]. In general, the higher the energy of the neutron, the shorter the wavelength, and thus a tuning of incident neutron energy enables the examination of processes on vastly different timescales in the system of interest. A schematic linking the energy of a neutron to the dynamical processes of condensed matter is presented in figure 1.2.

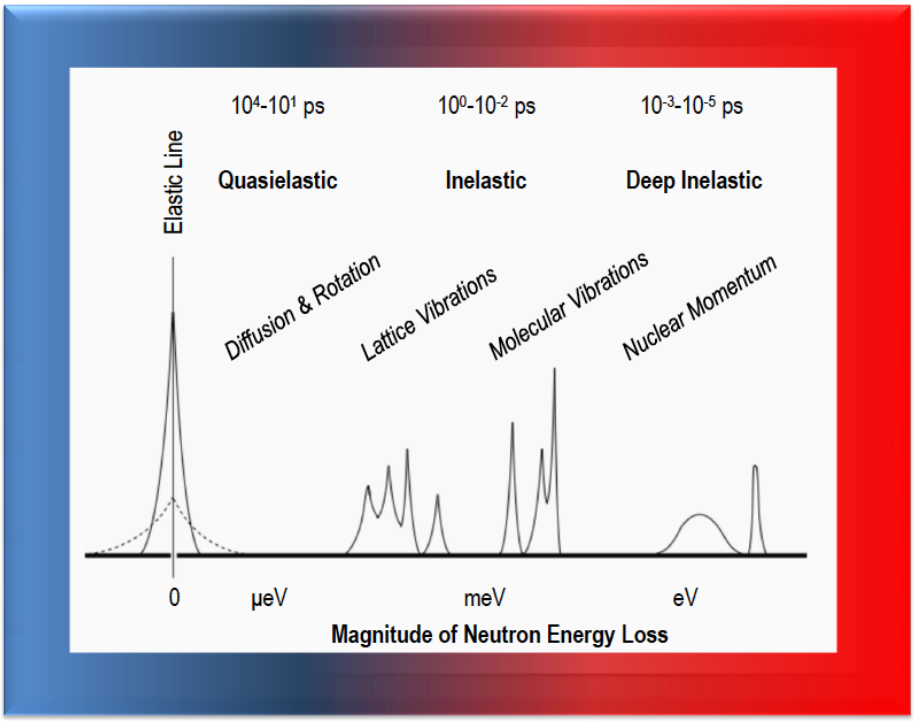

Figure 1.2: Schematic representation of neutron spectroscopies, demonstrating terminology in addition to the orders of magnitude of energy transfer. The dynamic processes and timescales examined are also included.

It can be seen that neutrons are able to act as a probe of processes on timescales differing by orders of magnitude, across an energy range of a few μeV up to tens of

eV. Quasielastic neutron scattering utilises cold neutrons to study long timescale and stochastic processes, such as molecular diffusion in liquids, or rotational reorientation (*cf.* 2.1.3). Rotational tunnelling is also able to be examined in this low energy region, with the tunnel-splitting of free-rotor fragments being of the order of 1 meV [10]. Lattice and low energy vibrational processes are probed via inelastic neutron spectroscopy, a broad term for studies using an instrument operating at energy transfers from a few to hundreds of meV, with intramolecular vibrational modes occurring at the higher energy range of inelastic processes (*cf.* 2.1.2). Finally, and of particular import to this thesis, deep inelastic scattering measurements have been made possible by utilising epithermal neutrons for energy transfers of eV magnitudes. The wavelength of neutrons at these energies are shorter than interatomic spacings, and thus scattering is from single nuclei with conservation of momentum (*cf.* 2.1.4). The emergence of neutron spectroscopy at these high energies is the topic of the next section.

1.3 The Advent of Deep Inelastic Neutron Scattering

Deep inelastic neutron scattering (DINS) enables an examination of momentum distributions and determination of the mean kinetic energies of atoms within condensed matter, and is the neutron analogue of Compton scattering of photons from electrons. The concept of DINS much predated it becoming an experimental actuality. Originally proposed by Hohenberg and Platzmann [11], with following

discussion by discussion by Gol'danski, Ivanov and Sayasov [12], it was theorised that neutrons of sufficiently high energy could be used to measure directly the momentum distribution of nuclei in condensed matter. There is direct analogy to the complementary technique of Compton scattering of high-energy photons from electrons, and thus DINS is often referred to interchangeably with 'neutron Compton scattering', NCS. To date, only one instrument has been able to conduct true DINS measurements, and that is the VESUVIO instrument at the ISIS source of pulsed neutrons (predecessor eVS). [3]

Considering the fundamental role of momentum in quantum mechanics, and indeed classical theories, the ability to measure accurately the momentum distributions in condensed matter is of great interest. This is particularly for cases where there is a distinct deviation from classical behaviour, as may commonly be the case for the proton, it being of relatively light mass. Historically the most important implementation of DINS has been in studying the superfluid, Bose-Einstein condensate phase of ^{4}He. The reader is referred to an extensive review of DINS [12] including the application to Bose-Einstein condensation [13, 14]. Studies have been conducted across a large phase range of liquid ^{4}He, following isochores across the superfluid transition, determining condensate fractions and mean kinetic energies. As such, deviations from classical behaviour have been, and continue to be well mapped.

[3]ISIS Facility, Rutherford Appleton Laboratory, Didcot, Oxfordshire OX11 0QX, U.K.

Beyond the study of Bose-Einstein condensation, DINS studies of ^{3}He [15] have been used to characterise an archetypal fermionic liquid/solid (despite the large absorption cross-section of approximately 5000 barn) and also mixtures of ^{4}He/^{3}He have been used to investigate Boson-Fermion interactions [16, 12]. These studies can be safely said to be far from the realms of chemistry, however, and a (chemically) much more important nucleus exists that has been studied extensively by DINS, and that is the proton.

Whilst DINS has proven vital in the study of molecular H_2 in both its ortho/para forms [17, 18], (and it should be said *vice versa*, with the early analysis of these systems constantly forcing reevaluation and refinement of how to interpret DINS data), it is the examination of the proton in chemical systems that is of import to this thesis, and thus the focus of this brief overview. The importance of DINS to the study of proton-containing systems must be emphasised, noting that even at room temperature, 99% of the proton kinetic energy, probed directly, comes from zero-point motion. DINS thus enables a 'quantum snapshot' of the proton.

Recently many studies have been conducted applying DINS to water in many different forms [19, 20, 21, 22, 23]. A string of investigations by Senesi, Andreani, Pietropaolo and Reiter have not only determined the momentum distribution of protons in liquid H_2O at room-temperature, but also up into the supercritical phase [24, 25], and perhaps most interestingly (and contentiously) down into the supercooled phase [26, 27]. It has been shown that moving from the supercritical phase

down to ambient H_2O there is a distinct softening of the ground state potential experienced by the proton, and decrease in momentum distribution width, due to the increasing network of hydrogen-bonds in the system. Measurements down into the supercooled phase, however, produced a particularly interesting and stark result; the appearance of second peak in the radially averaged momentum distribution. This has been linked to a very shallow, double-well potential, allowing the proton to tunnel through the potential barrier, effectively becoming delocalised between two sites. This is distinctly different from measurements of solid H_2O at the same temperature (*cf* section 5.5). Reiter *et al* also reported this second momentum peak in proton exchange membranes (Nafion 1120 and Dow 858) [28] and xerogels [29]. A narrowing of momentum width in confined water within carbon nanotubes [30], indicative of a distinct lessening of the intramolecular covalent bond, can also be explained by coherent delocalisation in a shallow well.

Very recently there has been a report from Reiter *et al* that the zero-point motion of protons accounts for the binding energy of water to *A*-phase DNA (which can be envisaged as the uncolied, hydrophobic form) and its transformation to the hydrated, double-helical *B*-phase [31]. Put in the bluntest way, quantum-motion of protons in the hydration shell of DNA is responsible for its dynamical uncoiling-coiling.

Moving beyond water, and DINS has been applied to a number of elements in their solid state. These include early measurements on Li [32] (enriched to ^{7}Li,

as DINS is sensitive to the isotopes of the lightest masses), Na [33], solid Ne [34] and graphitic C [35]. These studies were used both to compare the early DINS analysis protocols with theory, and to determine the level of anharmonicity across temperature ranges in these systems.

It is really only recently, within the last ten years, that the application of DINS has been extended to more complex systems, or to put this in a way more in line with this thesis, systems of a chemical interest. The proton momentum distributions and kinetic energies in binary metal hydrides, such as LiH [36], ZrH_2[37], LaH_2 and LaH_3 [38], have been determined. Protons in more complex salts have also begun to be investigated, and examples include $NaHF_2$ [39, 40] and $Rb_3H(SO_4)_2$ [41]. The latter case is particularly important, as a single crystal sample was used in conjunction with long run times to produce particularly high quality data, with the resultant, non-spherically averaged (essentially model free) proton momentum distribution being used to reconstruct the 3D Born-Oppenheimer potential for the proton. Single crystal measurements on KH_2PO_4 [42] were able to discern distinct anharmonicities in the unaveraged momentum distribution, shedding light on the ferroelectric phase transition.

Something that has been distinctly lacking in DINS, and is the focus of chapter 4 of this thesis, has been an extension of its application to heavier masses. As will be shown in chapter 2, and discussed in the results presented in chapter 5, the measurement of the momentum distribution in heavier masses faces a number

of distinct problems, and there is always the question as to why they should be measured in the first place. One particular mass of importance in applied science is Li, though this can not be strictly considered a 'heavy mass' in the framework of DINS (*cf* section 5.3). Currently there is only one study conducted to examine the momentum distribution of ^{7}Li in a complex salt, and that is on $LiTiS_2$ [43]. Other compounds were examined in this study, namely LiV_2O_5 and $Li_{0.45}MoO_3$, but these latter two suffered from both the low scattering cross-section of $^{6/7}$Li, and the earlier configuration of eVS, compared with the modern detector capabilities of VESUVIO.

There is one final thing remaining to be mentioned in this section, and that is the discovery by Chazidimitriou-Dreismann in 1997 of an anomaly in the measured scattering cross-section of the proton in DINS [44]. It was seen that in a comparison of stoichiometric mixtures of H_2O and D_2O, there was a deficit in the proton signal, contrary to the theory of DINS presented in chapter 2. This 'anomalous cross-section' has been witnessed in a number of further systems, including H_2/D_2 [18], LiH [45], C_6H_6, LaH_3 and LaH_2 [38, 46]. Currently no theoretical explanation as to the origin of this effect has proved conclusive, all accompanied by rigorous examination of the setup of VESUVIO, analysis and measurement protocols in DINS [47, 48]. These theories relate to the sub-femtosecond dynamics of the neutron-proton interaction, and include entanglement of spin and/or spatial degrees of freedom [49, 50], or a breakdown in the Born-Oppenheimer approximation [51] at these timescales. What *has* been determined, however, is that this

intensity deficit does not affect the measured momentum distributions in DINS, and thus whilst fascinating, can no more be termed detrimental to the technique than the difficulty of predicting intensities in Raman scattering of light.

1.4 Neutron Studies on Zeolite Frameworks

In keeping with the initial premise of this thesis, it is useful to explain the manner in which neutron spectroscopies have been applied to zeolite systems over the last twenty years, and emphasise the importance and scope of such studies to date. Initially in this section, a general overview of what is meant by 'zeolite' in terms of materials chemistry will be given, and then the distinctly different applications of quasielastic neutron scattering and inelastic neutron scattering will be discussed with relevant examples from the literature.

1.4.1 Zeolites and Their Uses

'Zeolite' is the term given to a family of aluminosilicate materials which are of a crystalline but highly (micro)porous structure. They have long been cherished in chemistry for their varied uses in selective catalysis, gas storage and as molecular sieves as will be exemplified below, and also due to their inexpensive and ready synthesis [52]. For these reasons they are almost certain to be encountered as part of an undergraduate course in materials chemistry.

The etymology of the name 'zeolite' is particularly entertaining in both its lit-

erality and contrary terminology. Combining the roots $\zeta\acute{\epsilon}\omega$ (*zeo*, to boil) and $\lambda\iota\theta o\varsigma$ (*lithos*, stone) it demonstrates the tendency for the early, naturally occurring zeolites to froth or bubble on the surface when heated. These 'boiling stones' are now known to exhibit this behaviour due to their porous structures absorbing water from the atmosphere and releasing it when heated. Zeolites and similar materials are still used as dessicants for this same absorbative purpose.

Whilst some zeolites can be prepared in a purely silicate form, in general they consist of structures composed of corner shared SiO_4 and AlO_4 tetrahedra. Assigning the formal charges Si^{IV} and Al^{III} resulting in any aluminosilicate framework having a net negative charge, which is counterbalanced by the existence of extra-framework cationic species. The frameworks themselves can take on a multitude of different geometries and sizes, due to the flexibility of the T-O-T bonds (where T denotes either a Si or Al tetrahedral centre) forming large networks of multidirectional channels and cage-like pores [53].

There are currently 197 zeolite framework topologies recognised by the zeolite community [54, 55], each assigned a three letter code in addition to its generic name. The zeolite framework type used in this thesis is denoted LTA (Linde Type A) and is discussed in detail in chapter 3. Four example structures along with their framework densities are given in figure 1.3.

The uses of zeolites are many, being related to structure, size and chemical com-

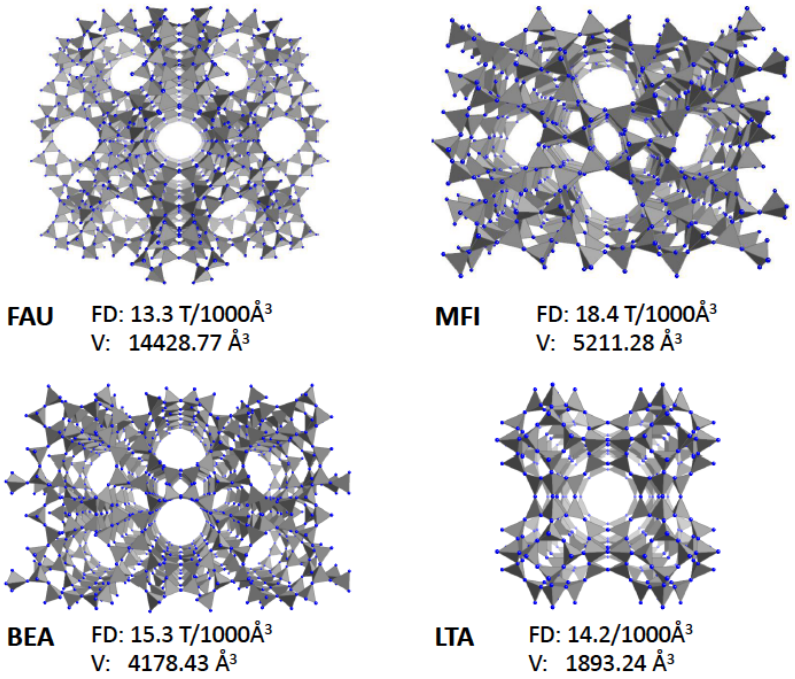

Figure 1.3: Example topologies for common zeolite frameworks, detailing framework densities (number of TO_4 tetrahedra per 1000 $Å^3$) and unit cell volume.

position, and unnecessary to delve into here as they are unrelated to the work encompassed by this thesis. Two of the more general uses of zeolites are worth mentioning, however, and that is their use in the fields of catalysis and for the storage of gaseous compounds [56].

Zeolites possess certain physical properties that have made them ubiquitous in industrial catalysis [57], which are coupled with their relative inexpense and ease of synthesis. Despite the large number of different frameworks in existence, a vast majority of processes employ only a small number of zeolites, namely forms of MFI, FAU, MOR and BEA. The large internal volume of zeolites dictates that almost

all catalytic activity takes place on the internal surface. The large 3-dimensional network of pores also facilitates diffusion of both reagents and products throughout the system. The true strength of zeolites in catalytic processes is perhaps the ease with which they can be altered or selectively 'designed' [58]. The various pore and cage sizes can enable a steric-selectivity in the reaction of interest, and the ability of extra-framework cation substitution or salt occlusion enables tailoring or introduction of active sites for catalytic processes [59]. Examples of common catalytic uses of zeolites is given in figure 1.4

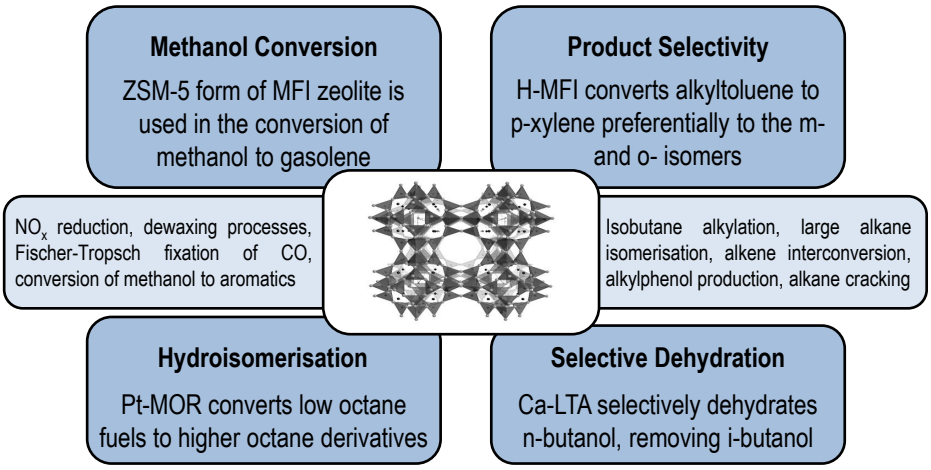

Figure 1.4: Example scope of zeolite use in industrial catalysis, denoting specific zeolites used in four areas [60].

The reversible storage of gaseous compounds is a continually growing field, particularly in recent years with the advent of research into the 'hydrogen economy'. Once it was recognised that a cleaner fuel economy could be realised if hydrogen

was utilised as the fuel source [61, 62], considering the specific energy density of hydrogen is $33.3\,\mathrm{kWkg^{-1}}$ compared to $12.8\,\mathrm{kWkg^{-1}}$ for standard petrochemical fuel sources, research was initiated into the problem of a suitable storage medium for it. The large internal surface area and inert nature of zeolite frameworks made them promising candidates for the large-scale storage of gaseous compounds, and it was also recognised early on that in addition to this large surface area for physisorbtion, the existence of extra-framework cations in the zeolite system would enable additional chemisorbative centres [63].

Initial measurements by Anderson *et al* demonstrated the ability of fully dehydrated zeolite systems to reversibly store hydrogen [64], with differing volumetric capabilities being demonstrated for different zeolite frameworks. Zeolites were soon discounted as applicable hydrogen stores, however, as their storage capacities were of the order of 1-2 wt%, far below the target value dictated by the United States Department of Energy [65], which specifies a minimum of a fully reversible 6 wt% at ambient conditions.

Despite being drastically out-performed by their organometallic analogues (metal organic frameworks, MOFs, and covalent organic frameworks, COFs), zeolites are still the workhorse for initial testing of gaseous storage capacities, moving beyond hydrogen into other important environmental molecules, such as CO_2 and NH_3 [63].

1.4.2 Quasielastic Neutron Studies

It has been mentioned above that the porous nature of zeolites enable them to readily absorb molecules, exemplified by their usage in either storage or catalytic processes. This absorption is obviously crucial for the application of zeolites in these fields, and neutrons enable a truly microscopic examination of processes by which absorption takes place. For a true investigation of molecular absorption into the zeolite framework, the dynamics of the molecule must be understood in terms of their diffusivity and intramolecular reorientations. Recalling figure 1.2 it can be seen that the use of cold neutrons with energy transfers of below 1 meV can be used to examine these long-timescale processes, termed 'quasielastic neutron scattering' (QENS) [66]. The theoretical backdrop of QENS is outlined in section 2.1.3, with only an outline of QENS as specifically applied to zeolite systems presented here, representing the scope of research detailed in the literature.

It is fair to state that the application of QENS to zeolite systems is dominated by the examination of diffusive processes, whereby molecular dynamics in the well-ordered, confined geometries of the zeolite pores can be studied. The determination of rates of diffusion for a variety of different organic molecules, through the porous frameworks of a number of different zeolites, have been reported, though studies have concentrated on the larger-pore zeolites.

For the NaZSM-5 form of the MFI zeolite framework [67], the self diffusivity (D_s)

of species such as methane, ethane, propane, butane and propene have been reported, and are presented as examples in table 1.2. In each case the process of diffusion is seen to not be continuous (Fickian) but proceed via a jump-diffusion model. The organic molecule diffuses in steps, whereby it occupies one site for a given residence time (τ) before moving an average distance (jump step, l) in a time interval far less than τ. After a large number of jumps, Fickian diffusion is observed.

Table 1.2: *Selected QENS Studies of Diffusion of Small Molecules in NaZSM-5*

Species	D_s ($10^{-5}\,\mathrm{cm^2 s^{-1}}$)*	τ ($10^{-12}\,\mathrm{s}$)	$\langle l \rangle$ (Å)*	T (K)
CH_4 [68]	2.8(2) - 2.9(8)	65	10.4(2) - 8.6(8)	200
C_2H_6 [69]	2.0(1) - 1.2(8)	100	7.5(8) - 11.0(1)	300
C_3H_8 [69]	1.2 (1.5) - 6.0 (8)	100	6.6(8) - 9.2(1.5)	300
n-C_4D_{10} [70] [a]	0.4(2)	108	5.9(2)	200

* values in parentheses give approximate loadings of organic molecule (/unit cell)
[a] QENS for deuterated samples strictly measure transport diffusion (D_T)

Another important, large-pore zeolite framework is FAU, particularly the forms denoted NaY [71] and NaX [72]. Due to its relevance in applied or industrial processes, and its ready availability, along side NaZSM-5, many QENS studies have been performed for organic molecules diffusing in NaY/NaX, and a small number are represented in table 1.3.

The values reported in tables 1.2 and 1.3 exemplify the application of QENS to diffusive processes in zeolites, and a few things are worth commenting on briefly.

Table 1.3: *Select QENS Studies of Diffusion of Small Molecules in FAU*

Species	D_s (10^{-5} cm^{2}s^{-1})*	τ (10^{-12} s)	$\langle l \rangle$ (Å)*	T (K)
CH_4 (NaY) [73]	5.2 (9.5) 7.9 (30.7) 6.7 (40.8)	-	-	200
H_2 (NaX) [74]	65.0 (7.5)	-	-	100
n−pentane (NaY) [75]	3.6 (1)	99.6, 620.6	-	360
isopentane (NaY) [75]	3.6 (1)	117.1	-	360
neopentane (NaY) [75]	4.2 (1)	85.2	-	360

* values in parentheses give approximate loadings of organic molecule (/unit cell)

Firstly, it may be obvious to point out that even in large pore zeolites, diffusivities of the same organic molecule can differ. This can be seen in the tables above for the cases of CH_4. Also determined in these studies was that the diffusivity of CH_4 was not affected by the presence of low concentrations of larger organics (such as deuterated n-butane) in the system. The reported values for pentane isomers in table 1.3 are particularly important, as that study was the first to experimentally demonstrate the 'levitation effect' in zeolites, whereby diffusion is accelerated for smaller molecular cross-section isomers, of the same mass and with essentially the same isomer-zeolite interaction potentials.

Finally it is worth noting that QENS measurements of protonated species (where scattering is essentially incoherent) enables determination of the self-diffusion coefficient, D_s, i.e. the progress of an individual proton/molecular species. By measuring deuterated samples the transport diffusion coefficient, D_T can be determined, although this is often complex in practice, and requires the self diffusion of hydrogen in the system to be known. Due to scattering from deuterium be-

ing both coherent and incoherent (*cf.* 2.1.1) both self and transport diffusion can be measured simultaneously, with the contribution from transport diffusion arising from the measurement of collective motions through the coherent cross-section[76].

QENS is by no means limited to the study of molecular diffusion, however, and the examination of processes on shorter timescales can be probed, most notably molecular rotations. Strictly speaking the experimentally determined scattering law is a convolution of individual scattering laws corresponding to translation, rotation and internal vibration (*cf.* section 2.1.3), but at the low energy transfers measured in QENS no internal vibrations are excited and the contribution is merely a flat background and negligible exponential (the Debye-Waller factor discussed in chapter 2).

Most QENS studies designed specifically to examine rotational characteristics of molecules are not for those encapsulated in zeolites (where molecules have a tendency to diffuse), and in recent years an increasing number of studies have been reported on solid materials containing molecular subunits. To this end the rotational nature of species such as borohydrides [77, 78], ammines [79], alanates [80] and amido-boranes [81] have been determined, as well as a vast number of studies on methyl-group rotations in organic compounds. In many cases QENS has been used to determine not simply an effective rate or rotation, but also the nature of rotation; examples being whether the molecular fragment is acting as a free-rotor, jumping around distinct angles on a circular path or rotating on the surface of a

sphere.

For studies on zeolite systems, larger aromatics or cyclic organic species encapsulated in ZSM-5 such as C_6H_6 [82], C_6H_{12} [83] and $Fe(C_5H_5)_2$ [84] have been reported, where diffusion is on timescale outside that being measured, allowing for the isolation of rotational dynamics. Smaller organics have also been studied, extracting contributions from rotational motion from the total scattering law. These include, but are not limited to C_3H_8 [85], C_3H_6 [86] C_2H_6 [69] and CH_4 [68].

1.4.3 Inelastic Neutron Studies

Whereas long-timescale dynamics are probed in quasielastic neutron spectroscopy, the use of thermal neutrons with energy transfers of several to hundreds of meV, termed inelastic neutron spectroscopy (INS), allows the investigation of vibrational processes [7]. As such it is appropriate to begin this section with a comparison with vibrational techniques more familiar in the study of chemical systems, infrared (IR) and Raman spectroscopy [87].

Photons with energies in the IR region are able to be absorbed by matter, through an electromagnetic interaction with the electronic wavefunction, and excite vibrational modes associated with the sample symmetry. For this to occur there is the gross selection rule that the electric dipole moment of the sample must change for the atomic displacements excited. In contrast to this absorptive process, Raman spectroscopy is a scattering technique, where incident photons lose or gain

energy (from excited systems) through interaction with the electronic wavefunction. The gross selection rule for Raman scattering is that the polarizability of the system must change for the atomic displacements examined. Both IR and Raman spectroscopies also exhibit the specific selection rule that the vibrational quantum number, ν, must only change by ± 1.

INS is not governed by the above selection rules, however, and thus whereas some vibrational modes and overtones are IR or Raman inactive, INS is sensitive to all vibrational modes, including overtones and combination modes. INS is, however, 'hindered' at higher energy transfers by the Debye-Waller factor, an exponential term discussed in the next chapter, and thus, while INS is ideal for the study of low energy phonon modes, unlike IR and Raman techniques, some intramolecular processes exhibit little intensity. The Debye-Waller factor also necessitates the use of cryogenic temperatures. Table 1.4 summarises the advantages and disadvantages of INS compared to the complimentary photon techniques [87].

Similarly to QENS, the high incoherent scattering cross section, σ_i, for H allows for the isolation of vibrational modes involving its displacement in INS. Due to a zeolite framework being (essentially) proton-free, this results in an INS spectrum of any proton-containing species introduced to the zeolite being representative of that species specifically. This enables adsorbate-zeolite interactions to be probed, or the manner in which the framework perturbs the vibrational modes of the introduced species.[4] Over the last 20 years there have been significant advances made

[4]This is by no means to say that INS is only useful for vibrational analysis of proton-containing

Table 1.4: *Comparrison of INS with IR and Raman Techniques*

Inelastic Neutron Spectroscopy	IR and Raman Spectroscopy
Sensitive to light elements, most notably H, with scattering related to σ_i.	Scattering scales monotonically with electron density.
Sensitive to isotope substitution	Insensitive to isotope.
Absence of vibrational selection rules.	Gross and specific selection rules.
Large sample sizes and long runtimes required	Small quantities of sample with very short runtimes.
Often suffers from low resolution	High resolution readily available
Penetrating radiation ideal for bulk analysis	Non-penetrating radiation leading to surface sensitivity
Ease of calculating intensity	Intensity rarely calculable
Low temperatures required	Large temperature range

by INS in terms of zeolite research, and notable studies or those relevant to this thesis will be briefly reviewed here.

Zeolite frameworks themselves have been studied, particularly those which contain protons directly attached to oxygen of the framework (acid zeolites, such as H-ZSM-5) or in cases where the extra-framework cations contain protons, as is the case for NH_4^+ [89, 90]. This has been particularly useful in understanding the mechanism by which NH_4^+ zeolites decompose to evolve NH_3 and create acid zeolites, which as shown in the previous section are important catalytic materials. One of the most important templating materials in zeolite synthesis is $N(CH_3)_4^+$, and the torsional and bending dynamics of the CH_3 groups have been studied in a number of different frameworks [91]. A recent paper in *Science* has suggested

compounds, and recently a particularly thorough study has been reported assigning each of the internal and external vibrational modes of C_{60} [88], noting that only 14 of the 46 internal modes are active in either IR or Raman spectroscopy.

that INS measurements on the lowest energy phonon modes may be critical in understanding the glass-transition in silicates [92]. This is unrelated to this thesis, but is enchanting and enforces the role of INS in studying this family of compounds.

As is always the case in neutron techniques, the study of H_2O in zeolites has been constant, and constantly reevaluated over the last decade [93]. The examination of H_2O-zeolite interactions by INS has revealed a number of interesting results, which include a ubiquitous distortion of the H-bonds in the H_2O network of hydrated zeolites [94], witnessed by a distinct lowering of the cutoff of librational bands. It has also been seen that the degree of distortion is related to the extra-framework cationic species present in the zeolite, with studies on the fully hydrated, small-pore NaA zeolite showing that as greater numbers of Na cations were replaced with Mg, the librational distortion decreased to approach that found in hexagonal ice, I_h [95]. INS has also been used to verify calculations and show that the interaction of H_2O with acid sites in a zeolite does not form a hydroxonium ion, but rather coordinates via a dual H-bond [96].

Whilst it was described above how zeolites are inefficient H_2 stores, they remain archetypes in the field of porous materials, and thus the interactions of H_2 with different frameworks have been extensively examined in INS. These studies include investigations into the rotational-vibrational characteristics of the H_2 molecule, the translational vibration of the H_2-cation interaction at low loadings being seen to scale with cation polarising ability [97], and a novel η^2-H_2 complex with Cu cations

being characterised in Cu-ZSM-5 [98]. There have also been studies applying INS to the fields of catalysis, endeavouring to explain specific parts of reaction pathways, or reactive intermediates. These include the reduction of Ag^{+} in zeolite A to clusters of Ag_3^{+2} by the introduction of H_2 [99], and the dissociation of H_2 on ceria-supported gold nanoparticles [100].

The studies of organic molecules within zeolites echo those studies referenced on H_2O, and predominantly involve a comparison of the bulk or unimolecular vibrational characteristics with those of the confined molecule. As such the proton-framework interactions in C_4H_4O (furan) [101], CH_3OH [102], $CHCl_3$ and CCl_2CHCl [103] have been examined, detailing how this affects the symmetry of the molecules and thus their vibrational characteristics. The examination of C_6H_6 at different loadings has also determined the inter-molecular interactions to be uniquely situated between that in the molecular liquid and solid [104].

CH_4 occupies a particularly interesting position in terms of INS, in that it is a small molecule that is subject to molecular recoil upon neutron impact. The concept of recoil will be discussed in detain in the results presented in chapter 5, but here it is sufficient to say that instead of witnessing distinct vibrational features in the INS spectrum, the transfer of momentum in addition to energy that is unique to neutron spectroscopies results in a broad, gaussian peak being witnessed in the spectrum, that can directly relate to the kinetic energy of the molecule as a whole. It was determined by Jobic *et al* [93, 105] that this kinetic energy differed from that

expected from a perfect gas to the extent that it inferred that CH_4 did not diffuse through the zeolite as though the framework was static, but was perturbed. This measurement corroborated and helped to evaluate further QENS measurements.

1.5 The Objectives of This Thesis

As has been stated in the opening paragraphs of this introductory chapter, the investigations comprising this thesis can be divided into two principal objectives:

- The first is to investigate and assess the use of deep inelastic neutron scattering in the examination of nuclear momentum of complex systems. Particular interest will be focused on the investigation of the nuclear momentum of masses heavier than ^{4}He, and the analysis of backscattered neutron measurements.

- The second objective of this thesis is to undertake studies into the dynamics of the NH_3 molecule absorbed at low concentrations into two zeolite frameworks, the Na and Cu exchanged forms of zeolite LTA, NaA and CuA. To this end, inelastic and quasielastic neutron spectrocopic data will be presented to characterise dynamics across a range of timescales, with the aim of determining binding characteristics and thermal behaviour of these absorbed molecules. The level to which neutron scattering can investigate framework-NH_3 interactions will also be commented upon.

In pursuit of the above objectives, and in addition to the underlying physics of the systems studied, emphasis will be laid on chemical interpretation. Neutron spectroscopy may be lagging slightly behind its crystallographic counterpart in acceptance in chemical research, but this is a paradigm politely being directed towards retirement.

Chapter 2

Neutron Spectroscopy

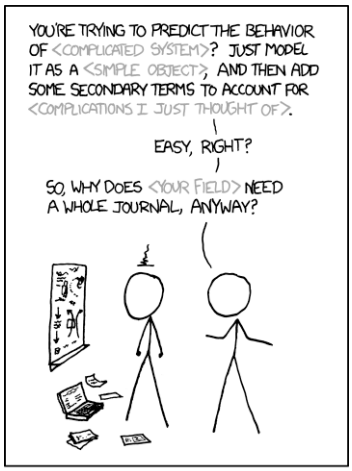

LIBERAL-ARTS MAJORS MAY BE ANNOYING SOMETIMES, BUT THERE'S *NOTHING* MORE OBNOXIOUS THAN A PHYSICIST FIRST ENCOUNTERING A NEW SUBJECT.

www.xkcd.com

Neutron spectroscopy is rarely encountered as part of an undergraduate course in chemistry[1], although there is little reason why neutron spectroscopy should be

[1]seeming to be regrettably ensconced in the minds of researchers as 'fiddly, unnecessary physics'. This is frankly quite ridiculous.

treated any differently by a chemist than the equally complex (yet commonly encountered) techniques such as NMR, Raman or Photoelectron Spectroscopy.

That being said, this chapter aims to reproduce a brief theoretical treatment of neutron scattering, in order to give the reader a suitable framework from which to understand the results and analysis routines presented in subsequent chapters. A full approach to the subject can be found in the works of Lovesey[4] or Squires[5], or references [6, 12, 66, 87, 106, 107]. Also included towards the end of this chapter is a brief discussion of the various spectrometers used to obtain the raw data for this thesis.

2.1 Neutrons and Scattering Theory

In this section, a quantitative description for the interaction of thermal neutrons with condensed matter is reproduced, principally following the approach of Squires[5]. Included is a description of how neutrons scatter from matter in a neutron experiment, what is actually measured and how this relates to the real properties of the system through the correlation functions encountered in this thesis. This has been the standard theoretical framework for neutron scattering, and is important to present here both for its elegance and for the understanding of data and refinements presented for each of techniques detailed in this work. As neutron energies from a few μeV to hundreds of eV have been used in the collection of raw data and subsequent results, the approximations inherent to these various

energy regimes are also discussed below. No part of this thesis is concerned with the magnetic scattering or polarisation of neutrons, and as such this chapter is limited to nuclear scattering alone.

2.1.1 The Scattering Law

The scattering of thermal neutrons from matter is weak. This statement may be simple, but within it is concealed a beautiful property of neutron scattering, and that is the use of the Fermi pseudopotential and single parameter, the scattering length, for the description of the scattering process.

The measurable quantity in a neutron scattering experiment is the differential cross section, $(d\sigma/d\Omega)_{\lambda\rightarrow\lambda'}$, for neutrons scattered into solid angle Ω. Denoting the initial and final states of the system as λ and λ' respectively, and the neutron wavevectors as $\mathbf{k}$ and $\mathbf{k'}$. The momentum transfer, $\mathbf{q}$, is related to the incident and final neutron wavevectors such that $\mathbf{q} = \mathbf{k} - \mathbf{k}'$. This is shown in figure 2.1 alongside a schematic for scattering of an incident neutron in a direction θ, ϕ. From figure 2.1 the differential cross section is defined as

$$\left(\frac{d\sigma}{d\Omega}\right)_{\lambda,\lambda'} = \frac{1}{\Phi}\frac{1}{d\Omega}\sum_{\mathbf{k}'} W_{\mathbf{k}\lambda,\mathbf{k}\lambda'}, \tag{2.1}$$

where $W_{\mathbf{k}\lambda,\mathbf{k}\lambda'}$ is the rate of transition between initial and final states of the scattering system and Φ is the flux of incident neutrons. Following standard theory, the sum in the right hand side of equation 2.1 can be expressed through Fermi's

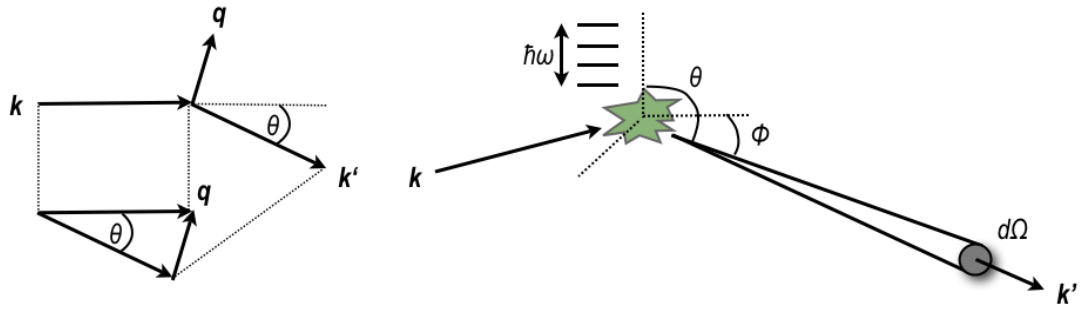

Figure 2.1: *left*: The 'scattering triangle' demonstrating incident neutron wavevector, **k**, final neutron wavevector, **k'**, and momentum transfer, **q**. *right*: Schematic for the scattering of incident neutrons into angle $\Omega(\theta,\phi)$

Golden Rule, thus the probability of the transition from initial to final state (per until time) is given by

$$\sum_{\mathbf{k}'} W_{\mathbf{k}\lambda,\mathbf{k}\lambda'} = \frac{2\pi}{\hbar}\rho_{\mathbf{k}'}|\langle \mathbf{k}'\lambda'|\mathbf{V}|\mathbf{k}\lambda\rangle|^2, \tag{2.2}$$

where $\rho_{\mathbf{k}'}$ is the density of final scattering states and $\mathbf{V}$ the interaction potential between neutron and system. The former can be determined along with the explicit form of Φ by the standard, yet artificial process of 'box normalisation'.[2] This technique is not reproduced here, as it is sufficient at this stage to state that substituting equation (2.2) into (2.1) with the explicit forms of $\rho_{\mathbf{k}'}$ and Φ yields

$$\left(\frac{d\sigma}{d\Omega}\right)_{\lambda,\lambda'} = \frac{k'}{k}\left(\frac{m}{2\pi\hbar^2}\right)^2 |\langle \mathbf{k}'\lambda'|\mathbf{V}|\mathbf{k}\lambda\rangle|^2. \tag{2.3}$$

By use of a δ-function allowing for a transfer of energy between neutron and system whereby total energy is conserved

[2] A particularly clear verification of this concept is presented in the work of Squires cited at the beginning of this chapter.

$$\left(\frac{d\sigma}{d\Omega dE'}\right)_{\lambda,\lambda'} = \frac{k'}{k}\left(\frac{m}{2\pi\hbar^2}\right)^2 |\langle \mathbf{k}'\lambda'|\mathbf{V}|\mathbf{k}\lambda\rangle|^2 \delta(\hbar\omega + E_\lambda - E_{\lambda'}). \tag{2.4}$$

Here E_λ and $E_{\lambda'}$ are the initial and final energies of the system, and $\hbar\omega$ the change in energy of the neutron.

The matrix element above can be evaluated for a normalised neutron wavefunction, described by a plane-wave $\exp(i\mathbf{k}.\mathbf{r})$, at position $\mathbf{r}$ interacting with nuclei j of coordinates $\mathbf{R_j}$ such that the total potential for the system if given by

$$\mathbf{V} = \sum_j \mathbf{V_j}(\mathbf{r} - \mathbf{R_j}). \tag{2.5}$$

Although the scattering of neutrons from matter is weak, the interaction between neutron and nucleus is through the Strong Nuclear Force, the form of which is unknown but known to be of very short range, far shorter than the wavelength of the incident neutron. Formally this results in isotropic scattering described by a single parameter, termed the scattering length, b, and the potential can be approximated as the Fermi pseudopotential

$$\mathbf{V}_{Fermi}(\mathbf{r}) = \frac{2\pi\hbar^2}{m}\sum_j b_j \delta(\mathbf{r} - \mathbf{R_j}), \tag{2.6}$$

and the matrix element is written explicitly as

$$\begin{aligned}\langle \mathbf{k}'\lambda'|\mathbf{V}_{Fermi}|\mathbf{k}\lambda\rangle &= \frac{2\pi\hbar^2}{m}\sum_j b_j \int d\mathbf{r}\ \exp(-i\mathbf{k}'\cdot\mathbf{r})\ \delta(\mathbf{r}-\mathbf{R_j})\ \exp(i\mathbf{k}\cdot\mathbf{r}) \\ &= \frac{2\pi\hbar^2}{m}\sum_j b_j \exp(i\mathbf{q}\cdot\mathbf{R}_j), \end{aligned} \tag{2.7}$$

where we have defined again $\mathbf{q} = \mathbf{k} - \mathbf{k}'$ as in figure 2.1. It is simple to show that equation (2.4) now reduces to

$$\begin{aligned}\left(\frac{d\sigma}{d\Omega dE'}\right)_{\lambda,\lambda'} &= \frac{k'}{k}\left|\sum_j b_j \langle\lambda'|exp(i\mathbf{q}\cdot\mathbf{R_j})|\lambda\rangle\right|^2 \delta(\hbar\omega + E_\lambda - E_{\lambda'}) \\ &= \frac{k'}{k}\sum_{jj'} b_{j'}b_b \langle\lambda|\exp(-i\mathbf{q}\cdot\mathbf{R_{j'}})|\lambda'\rangle\langle\lambda'|\exp(i\mathbf{q}\cdot\mathbf{R_j})|\lambda\rangle \\ &\quad \times\delta(\hbar\omega + E_\lambda - E_{\lambda'}). \end{aligned} \tag{2.8}$$

The delta-function can be written in integral form, and making use of the relation $\exp(-iE_\lambda t/\hbar)|\lambda\rangle = \exp(-iHt/\hbar)|\lambda\rangle$, where H is the Hamiltonian for the system, equation (2.8) can be expanded further to give

$$\delta(\hbar\omega + E_\lambda - E_{\lambda'}) = \frac{1}{2\pi\hbar}\int_{-\infty}^{\infty} \exp\{i(E_\lambda - E_{\lambda'})t/\hbar\}\ \exp(-i\omega t)dt \tag{2.9}$$

, where $\hbar\omega$ is defined as in equation (2.4)

$$\left(\frac{d\sigma}{d\Omega dE'}\right)_{\lambda,\lambda'} = \frac{k'}{k}\frac{1}{2\pi\hbar}\sum_{jj'} b_{j'}b_b \int_{-\infty}^{\infty} \langle\lambda|\exp(-i\mathbf{q}\cdot\mathbf{R}_{\mathbf{j}'})|\lambda'\rangle \times\langle\lambda'|\exp(iHt/\hbar)\exp(i\mathbf{q}\cdot\mathbf{R}_{\mathbf{j}})\exp(-iHt/\hbar)|\lambda\rangle\ \exp(-i\omega t)dt. \tag{2.10}$$

This complicated expression for the partial differential cross section for the scattering process is still between two states, λ and λ'. The expression is greatly simplified[3] by noting that the second matrix element in equation (2.10) can be expressed in terms of the Heisenberg operator $\mathbf{R}_j(t)$ such that

$$\exp\{i\mathbf{q}\cdot\mathbf{R}_{\mathbf{j}}(t)\} = \exp(iHt/\hbar)\exp(i\mathbf{q}\cdot\mathbf{R}_{\mathbf{j}})\exp(-iHt/\hbar). \tag{2.11}$$

Making use of the closure relation, and defining the partial differential cross section as the thermal average of that given above for two states, we can write

$$\left(\frac{d\sigma}{d\Omega dE'}\right) = \frac{k'}{k}\frac{1}{2\pi\hbar}\sum_{jj'} b_{j'}b_j \int_{-\infty}^{\infty} \langle\exp\{-i\mathbf{q}\cdot\mathbf{R}_{\mathbf{j}'}(0)\}\exp\{i\mathbf{q}\cdot\mathbf{R}_{\mathbf{j}}(t)\}\rangle\ \exp(-i\omega t)dt. \tag{2.12}$$

The thermal average (denoted by the use of $\langle ...\rangle$) is termed the correlation function, with the sum over all j for this defining the Intermediate Function, $I(\mathbf{q},t)$

[3] at least visually

$$I(\mathbf{q},t) = \frac{1}{N}\sum_{jj'}\langle \exp\{-i\mathbf{q}\cdot\mathbf{R}_{\mathbf{j}'}(0)\}\exp\{i\mathbf{q}\cdot\mathbf{R}_{\mathbf{j}}(t)\}\rangle. \tag{2.13}$$

At this juncture the emergence of coherence and incoherence (discussed in section 1.1) can be understood, as the scattering length averages across the system, $\langle b_j b_{j'}\rangle$, can be written as $\langle b^2\rangle$ or $\langle b\rangle^2$ for $j = j'$ and $j \neq j'$ respectively. Thus equation 2.12 can be split into two terms

$$\begin{aligned}\frac{k}{k'}(2\pi\hbar)\left(\frac{d\sigma}{d\Omega dE'}\right) &= \langle b^2\rangle \sum_j\sum_{j'}\int \langle \exp\{-i\mathbf{q}\cdot\mathbf{R}_{\mathbf{j}'}(0)\}\exp\{i\mathbf{q}\cdot\mathbf{R}_{\mathbf{j}}(t)\}\rangle\ \exp(-i\omega t)dt \\ &\quad +(\langle b^2\rangle - \langle b\rangle^2)\int \sum_{j'}\langle \exp\{-i\mathbf{q}\cdot\mathbf{R}_{\mathbf{j}'}(0)\}\exp\{i\mathbf{q}\cdot\mathbf{R}_{\mathbf{j}'}(t)\}\rangle\ \exp(-i\omega t)dt.\end{aligned} \tag{2.14}$$

By now defining the neutron cross-sections, σ, encountered in section 1.1, as $\sigma_i = 4\pi(\langle b^2\rangle - \langle b\rangle^2)$ and $\sigma_c = 4\pi\langle b^2\rangle$, this allows us to write a further function, $S(\mathbf{q},\omega)$, defined for coherent (c) and incoherent (i) scattering as

$$\left(\frac{d\sigma}{d\Omega dE'}\right) = \frac{N}{4\pi}\frac{k'}{k}\left(\sigma_c S(\mathbf{q},\omega)_c + \sigma_i S(\mathbf{q},\omega)_i\right), \tag{2.15}$$

with related intermediate functions

$$S(\mathbf{q},\omega)_c = \frac{1}{2\pi\hbar}\int I(\mathbf{q},t)_c \exp(-i\omega t)dt \tag{2.16}$$

$$S(\mathbf{q},\omega)_i = \frac{1}{2\pi\hbar}\int I(\mathbf{q},t)_i \exp(-i\omega t)dt. \tag{2.17}$$

This function, $S(\mathbf{q},\omega)$ is termed the Response Function. It has a central place in neutron scattering and historically is also referred to as the dynamic structure factor or scattering law.

This thesis is almost exclusively focussed on incoherent scattering investigations (whereby $S(\mathbf{q},\omega)_i >> S(\mathbf{q},\omega)_c$). This is due, in the case of systems containing hydrogen, to σ_i^H being far in excess of σ_i for all other species in the system, and also of σ_c^H. Deep Inelastic Neutron Scattering is an important deviation from this, in that *all* scattering is assumed to be incoherent, as will be detailed in section 2.1.4.

Further sections in this chapter are concerned by the forms adopted in each kinematic regime by the function $I(\mathbf{q},t)$, which is dimensionless and therefore $S(\mathbf{q},\omega)$, with units of energy^{-1}.

2.1.2 Inelastic, One-Phonon Scattering

Processes whereby the incident neutron exchanges energy with the sample are termed inelastic, which for thermal neutrons are at magnitudes of energy trans-

fer to create phonons in the system. Whilst coherent inelastic scattering can be utilised in the study of phonon-dispersion for single crystal samples, this thesis is only concerned with incoherent inelastic neutron scattering, IINS,[4] due to the examination of protons within a system (remembering that the incoherent scattering cross section for the proton is far larger than its coherent cross section) and their isotropic nature.

Taking as a suitable model a Bravais crystal; for each nucleus in the system, j, their position at time t can be expressed by their equilibrium position $\mathbf{l}$ and a displacement, $\mathbf{u}_j(t)$ for internal modes ν

$$\mathbf{R}_j(t) = \mathbf{l} + \mathbf{u}_j(t). \tag{2.18}$$

This expression can be substituted into the correlation function of equation (2.13) to yield the one dimensional scattering law in the form

$$S(\mathbf{q},\omega) = \frac{1}{2\pi\hbar}\int \langle \exp\{-i\mathbf{q}\cdot\sum^{\nu}\mathbf{u}_j(0)\}\exp\{i\mathbf{q}\cdot\sum^{\nu}\mathbf{u}_j(t)\}\rangle \exp(-i\omega t)dt, \tag{2.19}$$

which when summed over all modes (assumed to be harmonic and dynamically decoupled) becomes the product[5]

[4] commonly abbreviated to INS in the literature

[5] This form of nomenclature has been adopted from reference [7], whereby the displacement of atom j for an internal mode ν is given by ${}^{\nu}\mathbf{u}_j$.

$$S(\mathbf{q},\omega) = \frac{1}{2\pi\hbar}\prod_{\nu=1}^{\nu=3N}\int \langle \exp\{-i\mathbf{q}\cdot^{\nu}\mathbf{u}_j(0)\}\exp\{i\mathbf{q}\cdot^{\nu}\mathbf{u}_j(t)\}\rangle \exp(-i\omega t)dt. \quad (2.20)$$

By using the identity $\langle \exp U \exp V\rangle = \exp\langle U^2\rangle \exp\langle UV\rangle$, where U and V are defined as $\exp\{-i\mathbf{q}\cdot^{\nu}\mathbf{u}_j(0)\}$ and $\exp\{i\mathbf{q}\cdot^{\nu}\mathbf{u}_j(t)\}$ respectively, and taking the second term in the expansion [$\exp\langle UV\rangle = 1+\langle UV\rangle + \frac{1}{2}\langle UV\rangle^2 + ...$] , the Response Function of (2.20) for an incoherent one-phonon process, at the given energy ω_ν, can be written as

$$S(\mathbf{q},\omega_\nu)^{1p} = \frac{1}{2\pi\hbar}\int \exp -\langle\{\mathbf{q}\cdot\mathbf{u}_j(0)\}^2\rangle \exp\langle\{\mathbf{q}\cdot\mathbf{u}_j(0)\}\{\mathbf{q}\cdot\mathbf{u}_j(t)\}\rangle \exp(-i\omega t)dt,$$

where

$$I_\nu(\mathbf{q},t)^{1p} = \exp -\langle\{\mathbf{q}\cdot\mathbf{u}_j(0)\}^2\rangle \exp\langle\{\mathbf{q}\cdot\mathbf{u}_j(0)\}\{\mathbf{q}\cdot\mathbf{u}_j(t)\}\rangle. \quad (2.21)$$

Within this framework, each term in equation (2.21) can be determined individually, under the assumption that at cryogenic temperatures the system is harmonic. For a given mode, ν, the energy levels available are labelled by quantum state n and, following explicitly the approach of Lovesey [4], it can be shown that

$$\begin{aligned}\exp -\langle\{\mathbf{q}\cdot\mathbf{u}_j(0)\}^2\rangle &= \exp -\{\mathbf{q}\cdot^{\nu}\mathbf{u}\}^2(2\langle n\rangle + 1)\\ &= \exp -\{\mathbf{q}\cdot^{\nu}\mathbf{u}\}^2 \coth\left(\frac{\hbar\omega_\nu}{2k_BT}\right), \quad (2.22)\end{aligned}$$

and

$$\begin{aligned}\exp\langle\{\mathbf{q}\cdot\mathbf{u}_j(0)\}\{\mathbf{q}\cdot\mathbf{u}_j(t)\}\rangle &= \exp\left[\{\mathbf{q}\cdot^{\nu}\mathbf{u}\}^2\left\{(\langle n\rangle+1)\exp(-i\omega t)+\langle n\rangle\right)\exp(i\omega t)\right\}\right] \\ &= \exp(in\omega t)\frac{\exp\left(\frac{n\hbar\omega_\nu}{2k_BT}\right)}{\exp\left(\frac{|n|\hbar\omega_\nu}{2k_BT}\right)}\frac{(\{\mathbf{q}\cdot^{\nu}\mathbf{u}\}^2)^{|n|}}{|n|!}. \qquad (2.23)\end{aligned}$$

In the above, n designates the final state of the system, i.e. a one phonon creative process would be $n = 1$, and k_B is the Boltzmann constant. A full derivation of the above, and extension over three dimensions is a particularly involved process, and is detailed in the references given at the beginning of this chapter. The standard result is reproduced here, whereby the Response Function for the ν^{th} normal mode, excited at low temperature to the n^{th} harmonic is given by

$$S(\mathbf{q},\omega_\nu)^{1p} = \frac{\{\mathbf{q}\cdot^{\nu}\mathbf{u}\}^{2n}}{n!}\exp\left\{-\left(\mathbf{q}\cdot\sum_{\nu}{}^{\nu}\mathbf{u}\right)^2\right\}\delta(E_i - E_f + n\hbar\omega_\nu), \qquad (2.24)$$

or assuming at the response function is evaluated at a given transition, the intensity arising from a single atom l is given by

$$\begin{aligned}S(\mathbf{q},\omega_\nu)_l^n &= \frac{\sigma_l}{4\pi}\frac{\{\mathbf{q}\cdot^{\nu}\mathbf{u}_l\}^{2n}}{n!}\exp\left\{-\left(\mathbf{q}\cdot\sum_{\nu}{}^{\nu}\mathbf{u}_l\right)^2\right\} \qquad (2.25)\\ &= \frac{\sigma_l}{4\pi}\frac{\{\mathbf{q}\cdot^{\nu}\mathbf{u}_l\}^{2n}}{n!}\exp\{-(2W)\}.\end{aligned}$$

The above equation is for the creation of a phonon by neutron energy loss, which at the cryogenic temperatures for INS measurements far outweighs phonon anni-

hilation, or energy gain. It can be seen that the scattering intensity at a given frequency is related to the mode eignevector, $\mathbf{u}_l$, giving a direct link to calculation via methods such as DFT (discussed further in Appendix B). The argument of the exponential term of equation (2.25) is the Debye-Waller factor discussed in more detail in subsequent chapters, for which the full expression (i.e. not in the low temperature limit) can be written as

$$2W = \left(\mathbf{q} \cdot \sum_{\nu} \left\{ {}^{\nu}\mathbf{u}_l \coth \left(\frac{\hbar\omega_\nu}{2k_B T} \right) \right\} \right)^2 . \tag{2.26}$$

It must be stressed that equations (2.21) and (2.25) are for a single-phonon process. Generalising for multi-phonon processes (which importantly are measured in INS, as both overtones and combination modes) is ostensibly simple, involving further expansion of $[\exp\langle UV\rangle = 1 + \langle UV\rangle + ... + \frac{1}{n!}\langle UV\rangle^n]$, for n-phonon processes in equation (2.21).

One final point of discussion for INS is the link between $S(\mathbf{q}, \omega)$ and the vibrational density of states $Z(\omega)$. For incoherent scattering there are no interference conditions as there are for coherent scattering, and thus at a given incident wavevector and crystal alignment, incoherent, one-phonon processes cover a range of final wavevectors. Incoherent, inelastic scattering is therefore dependant on *all* normal modes satisfying the condition of ω_ν, i.e. the number of modes at a given phonon frequency. In principal, therefore, it is possible to directly calculate $Z(\omega)$ in an INS experiment, although in principal the corrections for multiphonon-processes

in particular, in addition to sample environment and neutron absorption make the determination of $Z(\omega)$ from INS difficult. Comparison with calculated $Z(\omega)$ is often simpler through the momentum distribution and DINS, as will be seen in Chapter 4 and Appendix A.

2.1.3 The Quasielastic Regime

The above section demonstrated the form of $I(\mathbf{q},\omega)$ for vibrational excitations, where neutron energy losses are of the order of a few to hundreds of meV. For energy transfers of a few to hundreds of μeV, however, longer timescale processes such as translation and diffusion can be examined. This low energy and wavevector transfer range defines the quasielastic region.

The form of $I(\mathbf{q},\omega)_i$ can be best understood in the quasielastic regime by first expanding it in the form [66]

$$I(\mathbf{q},\omega)_i = I(\mathbf{q},\omega)_i^R \cdot I(\mathbf{q},\omega)_i^L \cdot I(\mathbf{q},\omega)_i^V, \tag{2.27}$$

where the superscripts R, L and V relate to rotation, lattice modes and internal vibrations respectively. For a liquid sample and additional translational, T, term is included which can describe diffusion.. In writing the intermediate function in this way, dynamical independence between the different contributions has been assumed for equation (2.27). This is clearly true for internal vibrations, where the energies are of the order of hundreds of meV, compared to a few μeV for rotations.

For lattice modes this is not always the case.

The corresponding response functions can be written as convolutions

$$S(\mathbf{q},\omega)_i = S(\mathbf{q},\omega)_i^R \otimes S(\mathbf{q},\omega)_i^L \otimes S(\mathbf{q},\omega)_i^V. \tag{2.28}$$

Theoretically the functions for $S(\mathbf{q},\omega)_i^V$ should be sharp, and are centred at far higher ω values to that examined in a quasielastic experiment, and thus there is no contribution to the quasielastic scattering law. $S(\mathbf{q},\omega)_i^L$ can be shown to be a slowly varying term [106], which can be seen as a flat background in the quasielastic region.

Rewriting the incoherent intermediate function from (2.13) in the limit of $t \to \infty$

$$\begin{aligned} I(\mathbf{q},\infty)_i &= \frac{1}{N}\sum_j \langle \exp\{-i\mathbf{q}\cdot\mathbf{R_j}(0)\}\exp\{i\mathbf{q}\cdot\mathbf{R_j}(\infty)\}\rangle \\ &= \frac{1}{N}\left|\sum_j \exp(i\mathbf{q}\cdot\mathbf{R}_j)\right|^2, \end{aligned} \tag{2.29}$$

which arises from there being no correlation between displacement at time $t = 0, \infty$. The sum in equation (2.25) can be taken across the total number of sites visited by a single particle by a stochastic motion in these large timescales.

By now taking the intermediate function at a time, t, a separation into time

independent and dependant contributions can now be made, with a subsequent transform to the response function [66, 106]

$$I(\mathbf{q},t)_i = I(\mathbf{q},\infty)_i + I(\mathbf{q},t)_i \quad (2.30)$$

$$S(\mathbf{q},\omega)_i = I(\mathbf{q},\infty)_i\delta(\omega) + S(\mathbf{q},\omega)_i^Q. \quad (2.31)$$

The response function is thus comprised of a purely elastic component, $I(\mathbf{q},\infty)_i\delta(\omega)$ superimposed onto a quasielastic component for which the broadening is related to the timescale of particle motion, $S(\mathbf{q},\omega)_i^Q$.

Importantly, $I(\mathbf{q},\infty)_i$ has the dimensions of a structure factor (hence being termed the elastic incoherent structure factor, EISF) and can be measured directly in an incoherent quasielastic neutron scattering (IQENS) experiment, the shapes of which can be calculated for distinct geometries and diffusional models and will be discussed in section 5.4. For stochastic processes that are spatially restricted, $I(\mathbf{q},\infty)_i$ is finite, whereas for dynamical translational disorder $I(\mathbf{q},\infty)_i$ vanishes.

2.1.4 The Impulse Approximation

Neutrons of several to hundreds of eV in energy, available in Deep Inelastic Neutron Scattering (DINS), are very much in excess of the energy states available in a system under study. The timescales of interaction are sub-femtosecond ($1\,\mathrm{fs} = 10^{-15}\,\mathrm{s}$) with the highest energy neutrons available on the VESUVIO spectrometer

having interaction times on the attosecond timescale ($1\,\text{as} = 10^{-18}\,\text{s}$). As such the correlation function in DINS can be evaluated at short timescales. The formal approximation for this is termed the 'Impulse Approximation' and is expressed as

$$\mathbf{R}_{j'}(t) = \mathbf{R}_{j'}(0) + \frac{t}{M_{j'}}\mathbf{p}_{j'}, \tag{2.32}$$

where $\mathbf{R}_{j'}(t)$ and $\mathbf{p}_{j'}$ are the position at time t and momentum of nucleus j' respectively and $M_{j'}$ the nuclear mass. This expression can be substituted into the expression for the sum in the intermediate function (2.13)

$$I(\mathbf{q},t) = \frac{1}{N}\sum_{jj'}\langle \exp\{-i\mathbf{q}\cdot\mathbf{R_j}(0)\}\exp\{i\mathbf{q}\cdot\mathbf{R_{j'}}(0) + \frac{it}{M_{j'}}\mathbf{q}\cdot\mathbf{p}_{j'}\}\rangle. \tag{2.33}$$

Operators of position and momentum commute such that $[\mathbf{R}_{\alpha\mathbf{j}'}, \mathbf{p}_{\beta\mathbf{j}'}] = i\hbar\delta_{jj'}\delta\alpha\beta$ and thus using the approximation $\exp(\mathbf{A})\exp(\mathbf{B}) = \exp(\mathbf{A} + \mathbf{B} + \frac{1}{2}[\mathbf{A},\mathbf{B}])$ allows the intermediate function to be expanded thus [4]

$$\begin{aligned} I(\mathbf{q},t) &= \frac{1}{N}\sum_{jj'}\left\langle \exp\left(-i\mathbf{q}\cdot\mathbf{R_j}(0) + i\mathbf{q}\cdot\mathbf{R_{j'}}(0) + \frac{it}{M_{j'}}\mathbf{q}\cdot\mathbf{p}_{j'}\right.\right. \\ &\quad \left.\left. + \frac{1}{2}[\mathbf{q}\cdot\mathbf{R}_j(0), (\mathbf{q}\cdot\mathbf{R}_{j'}(0) + \frac{it}{M_{j'}}\mathbf{q}\cdot\mathbf{p}_{j'}]\right)\right\rangle \\ &= \frac{1}{N}\sum_{jj'}\exp\left(\frac{i\hbar t q^2}{2M_j}\delta_{jj'}\right)\left\langle \exp(i\mathbf{q}\cdot\{\mathbf{R'_j}(0) - \mathbf{R_j}(0)\} + \frac{it}{M_{j'}}\mathbf{q}\cdot\mathbf{p}_{j'})\right\rangle. \end{aligned} \tag{2.34}$$

This second step follows from the fact that position operators at time t commute. A further simplification of the above is the reduction of the double sum by enforcing $j' = j$. Conceptually this arises from the high energy neutrons possessing wavelengths far shorter than interatomic spacing, thus no collective motions are involved in the scattering process, and all scattering is incoherent. Formally this is true in the limit of high q, where no $j \neq j'$ terms are retained [12].

The dynamic structure factor (which is now solely the incoherent dynamic structure factor) within the impulse approximation can be written as

$$S(\mathbf{q},\omega) = \frac{1}{2\pi\hbar N}\sum_j \int_{-\infty}^{\infty} \exp\left(-i\omega t + \frac{i\hbar t q^2}{2M_j}\right)\left\langle \exp(\frac{it}{M_j}\mathbf{q}\cdot\mathbf{p}_j)\right\rangle dt. \qquad (2.35)$$

The expectation term in the above can be expressed in terms of momentum states, $\mathbf{p}$ and the single particle momentum distribution, $n(\mathbf{p})$

$$\left\langle \exp(\frac{it}{M_j}\mathbf{q}\cdot\mathbf{p}_j)\right\rangle = \int n(\mathbf{p}) \exp\left(\frac{it\hbar}{M}\mathbf{q}\cdot\mathbf{p}\right) d\mathbf{p}. \qquad (2.36)$$

This can be inserted into equation 2.18 and yields, after performing the integral over time, the dynamic structure factor in terms of momentum states for the Impulse Approximation

$$S(\mathbf{q},\omega)_{IA} = \hbar \int n(\mathbf{p})\delta\left(\hbar\omega - \frac{\hbar^2 q^2}{2M} - \frac{\hbar}{M}\mathbf{q}\cdot\mathbf{p}\right) d\mathbf{p}. \qquad (2.37)$$

This form of the dynamic structure factor is delightfully simple and yet deserving of a short discussion. Under the framework of the Impulse Approximation, equation 2.33 states that scattering occurs from single nuclei with conservation of momentum and kinetic energy, with the scattering nucleus behaving as if it were a free particle. Importantly, for these high energy collisions there is now a link between the experimental measurable, $S(\mathbf{q},\omega)$, and the momentum distribution of the nucleus, $n(\mathbf{p})$. Physically, each nuclear species j is observed in (q,ω) space as a peak centred at its recoil energy, $\frac{\hbar^2 q^2}{2M}$, and is broadened to an extent related to $\mathbf{q}$ and the mean-squared velocity of the nucleus as described in more detail below and in chapter 5.[6]

One final aspect of DINS that needs to be mentioned here is that of y-scaling. Often a large emphasis has been placed on expounding the origins, adherence and importance of this scaling within the framework of the Impulse Approximation, but the general acceptance of such for modern VESUVIO data means that a simple statement of y-scaling being true shall suffice. At the limit of infinite momentum transfer, $\mathbf{q}$, the dynamic variables ω and q can be coupled through the scaling variable, y, occasionally denoted the West variable after the originator of such a seemingly bizarre device

[6]This separation of species by M is the origin of DINS being termed a 'neutron mass-spectrometry' technique. This is particularly unfair, as it is the broadening of the spectral line [and therefore $n(\mathbf{p})$] that is the measurable of interest, which places DINS absolutely into the realms of spectroscopy.

$$y = \frac{M}{\hbar^2 q}(\hbar\omega - \frac{\hbar^2 q^2}{2M}), \tag{2.38}$$

and so the dynamic structure factor can be rewritten in terms of the neutron Compton profile, $J_M(y, \hat{q})$

$$S(\mathbf{q}, \omega)_{IA} = \frac{M}{\hbar q} J(y, \hat{q}), \tag{2.39}$$

$$J(y, \hat{q}) = \hbar \int n(\mathbf{p}')\delta(\hbar y - \mathbf{p}'.\hat{q}) d\mathbf{p}'. \tag{2.40}$$

Now $\hat{q}$ is a unit vector, and $J_M(y, \hat{q})$ represents the probability of a nucleus having momentum parallel to $\hat{q}$ between $\hbar y$ and $\hbar(y + dy)$. For isotropic systems the direction of $\hat{q}$ is immaterial, with the neutron Compton profile being given by

$$J(y) = 2\pi\hbar \int_{|\hbar y|}^{\infty} p n(p) dp. \tag{2.41}$$

The importance of y-scaling is that the recoil peak for a nucleus of a particular species is centred at 0 in y-space, with the y-transform allowing detector banks at distinct angles to be summed to increase statistics.

2.2 Instrumentation

Within this section, a brief outline of the instruments used to collect neutron data for this thesis is presented.[7] This enables a discussion of what is actually measured, and of course why, with factors such as resolution, which areas of (q,ω) space are sampled by each and limitations being discussed.

All instruments used for this work are based at the ISIS source of pulsed-neutrons (STFC, Chilton, UK) and thus the determination of the energy of incident or scattered neutrons is done by time-of-flight, ToF. For each process occurring within neutron spectroscopy, both the magnitude of wavevector change, q, and energy transfer, $\hbar\omega$, need to be determined.

2.2.1 TOSCA and MARI

The INS measurements detailed in chapter 5 were conducted on two, fundamentally different neutron spectrometers, TOSCA and MARI.

The primary spectrometer used was TOSCA [108, 109], a high-resolution, inverse geometry ToF spectrometer at ISIS. As such, the detected energy of scattered neutrons is fixed, and the incident neutron energy allowed to vary across a given range. Scattered neutrons are detected at a final energy of 3.5 meV.

[7] Thanks is extended to the Rutherford Appleton Laboratory for permission to reproduce instrument schematics

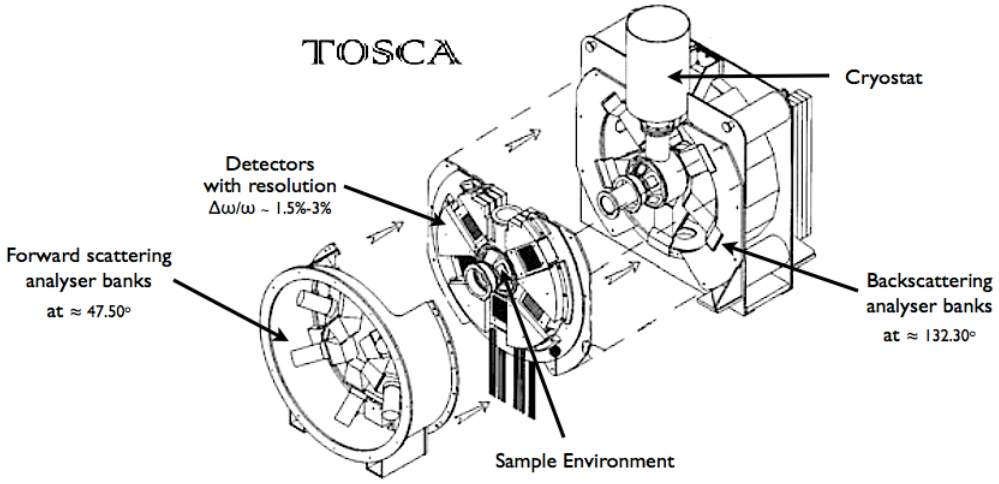

Figure 2.2: Schematic layout of the TOSCA instrument [108]

As can be seen from figure 2.2, TOSCA is arranged with two sets of detector banks, at fixed angles for forward scattering and backscattering of 47.50° and 130.30° respectively. Final energy is selected by pyrolytic graphic analysers, orientated to scatter incident neutrons into the (002) plane. Higher order reflections from this plane are removed by a cooled Be filter placed between analyser and ^{3}He detector.

The resolution of TOSCA is given by $\Delta\omega/\omega \simeq 1.5 - 3\%$, which gives high resolution at lower energy transfers. q rises swiftly with ω, and the arrangement of forward and backscattering detectors at fixed angles enables two close (yet different) q, ω trajectories to be measured.

Conversely, MARI [7, 110] is a direct geometry inelastic spectrometer, whereby the incident neutron energy is fixed and that of the detected neutron allowed to

vary, over which a large area of $(\mathbf{q}, \omega)$ space can be sampled. A comparison of indirect and direct geometry operation in time of flight is demonstrated schematically in figure 2.3. TOSCA follows two, very close trajectories in $(\mathbf{q}, \omega)$ space, whereas MARI samples across a range of trajectories dependant on detector angle.

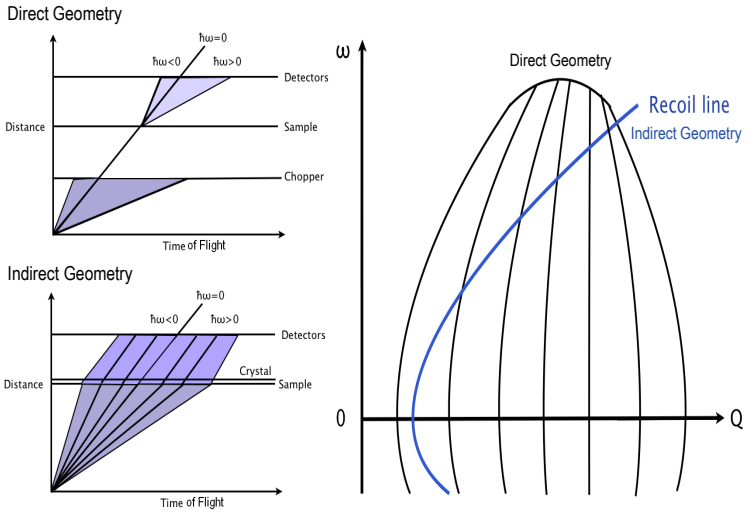

Figure 2.3: Direct verses indirect geometry in time of flight (*left*) and the regions of $(\mathbf{q}, \omega)$ space examined

The MARI spectrometer layout is shown in figure 2.4. The direct geometry of MARI requires a large detector array, which are arranged in a vertical array as large plates of detectors at identical final flightpaths from the sample (allowing for identical resolution functions for each detector bank). This allows for a good coverage of $(\mathbf{q}, \omega)$ space, determined by incident neutron energy as selected by the phasing of the Fermi chopper. The detectors on MARI are based around ^{3}He, covering an angular coverage of 3-135°. For the measurements presented here,

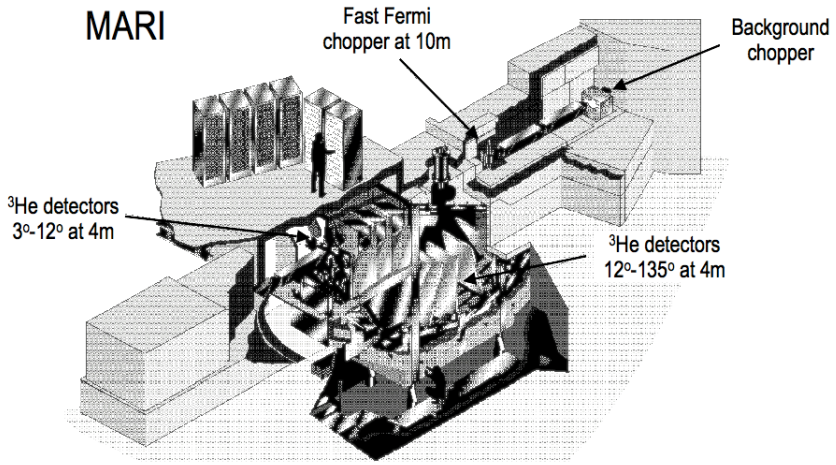

Figure 2.4: Schematic layout of the MARI spectrometer [110]

incident neutron energies were fixed between 50-200 meV, and the resolution of MARI is approximately 3-5% of the incident neutron energy.

2.2.2 IRIS

IRIS [111] is a spectrometer designed for the examination of quasielastic and very low energy transfer inelastic processes. similar to TOSCA it operates in inverse geometry, whereby the final/detected energy of scattered neutrons is selected, as determined by the backscattering crystal analysers. The incident neutron energy is allowed to vary around these detected energy windows, whilst avoiding frame overlap in a given pulse from a previous one, which for IRIS is achieved by the use of two disk choppers, situated 6.3 m and 10 m away from the sample. The range of energy examined in an IRIS experiment can be chosen by varying the phasing of these choppers. The incident flightpath on IRIS is 36.5 m from source to target.

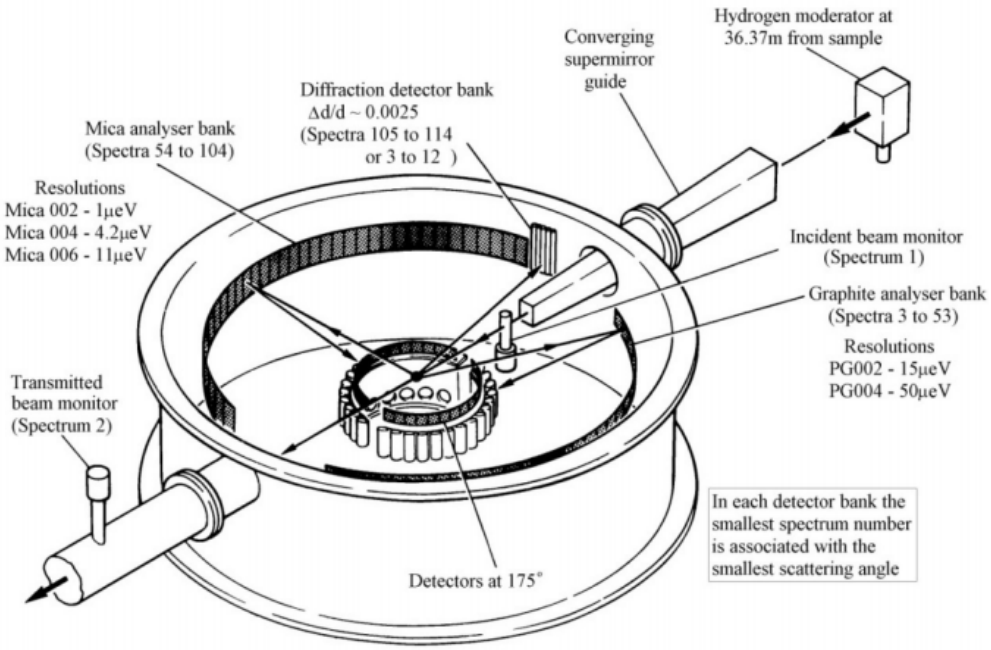

Figure 2.5: Schematic layout of the IRIS instrument [111]

As can be seen in figure 2.5, IRIS consists of two arrays of crystal analyser banks each operating close to backscattering angles. These are pyrolytic graphite (pg, analysers 3-53) and mica (analysers 54-104) single crystal analysers shown. These analysers are perfect single crystals and by selecting different reflections (for example pg002 and pg004), a different dynamical range and resolution can be selected, where each reflection is centred around $\hbar\omega = 0$ for quasielastic studies. IRIS also has a high resolution diffraction detector bank (detectors 105-114) as shown in figure 2.5. The detector arrays on IRIS are composed of ZnS scintillators and ^{3}He gas-tubes for diffraction measurements.

Table 2.1: *Common Dynamical Ranges of the IRIS Spectrometer*

Analyser	pg002	pg002-offset	mica006	mica004
Energy Range (meV)	-0.4 to 0.4	-0.3 to 1.2	-0.4 to 0.4	-0.15 to 0.15
Resolution (μeV)	17.5	17.5	11.0	4.5
Q (Å^{-1})	0.42 to 1.85	0.42 to 1.85	0.40 to 1.87	0.26 to 1.24

The dynamical range examined by some of the more common chopper phasings on IRIS is detailed in table 2.1. The mica006 and pg002 arrays use the same chopper phasing, with data for these analysers thus collected simultaneously. The pg002-offset setting allows a higher energy range to be examined, and the use of mica004 enables a high resolution at the sake of flux (0.15 that of pg002).

2.2.3 VESUVIO

The VESUVIO instrument [12, 112] is currently unique, being the only instrument currently operational that is able to utilise neutrons of high enough energy for the Impulse Approximation in DINS to hold.[8] Typically the kinematic regime for VESUVIO measurements are for energy transfers in the range $1< \omega <50\,\text{eV}$ with wavevector transfers of $40< q <150\,\text{Å}^{-1}$. The schematic layout of VESUVIO is shown in figure 2.6.

As can be seen from figure 2.6, the detector layout of VESUVIO consists of several banks at forward-scattering angles in the rangle 30°-70° (detector numbers 135-

[8]although a recent neutron study on ^{4}He analysed under the Impulse Approximation, using the ARCS instrument at ORNL. The far lower energy and momentum transfers than VESUVIO result in strict corrections for final state effects, FSEs, defined later.

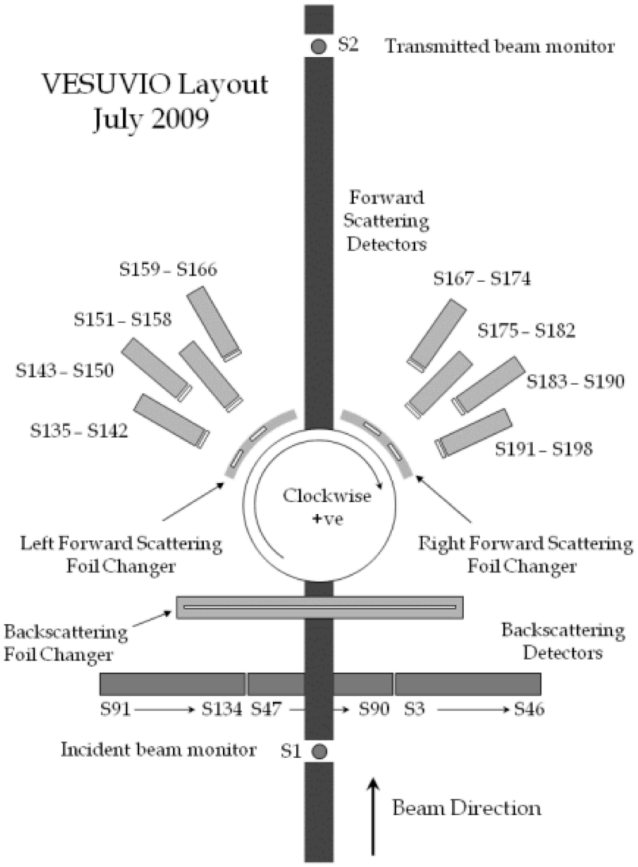

Figure 2.6: Schematic layout of the VESUVIO instrument [112]

198, although in this work only detectors 135-182 were operational, with those at 183-198 not currently optimised for γ-background removal) and three banks at back-scattering angles in the range 130°-170°(detector number 3-134). Due to the mass of the proton being approximately equivalent to the neutron, all scattering from the proton is in the forward direction.

VESUVIO operates in inverse-geometry where the final energy of the neutron that is fixed by the use of gold-foil covered detectors. The nuclear resonance at 4.9eV

ensures only scattered neutrons at this energy are detected. A recent upgrade to the VESUVIO instrument saw the installation of secondary gold foils in an array between the fixed sample and detectors. By cycling these foils so that measurements are taken with them directly between the sample and detector (termed 'in') and not (termed 'out') the resolution of VESUVIO was improved by an order of magnitude.

As it is the γ-radiation resulting from the nuclear resonance of the gold that is detected in a VESUVIO measurement, the use of secondary foils results in an additional background signal. The forward detectors (YAP, yttrium aluminium perovskite) are particularly sensitive to this background, and so as part of standard analysis protocol this signal is accurately modelled and removed. The backscattering detectors are comprised of ^{6}Li and are less sensitive to this additional background.

Chapter 3

Sample Chemistry and Preparation

"How ghastly for her, people actually thinking, with their brains, and right next door. Oh, the travesty of it all."

Gail Carriger, Soulless

As is apparent from the preceding chapters, this thesis is divided into two sections, each detailing results from the application of neutron spectroscopic techniques. Initially, the application of deep inelastic neutron scattering (DINS) to systems of mixed masses are presented, followed by an examination of the short to long-timescale dynamics of NH_3 coordinated within a zeolite framework. Whilst a broad introduction to neutron studies on zeolites and the emergence of DINS were detailed in chapter 1, the specific chemistry and (where appropriate) synthesis of samples used in this work are detailed in this chapter.

3.1 Zeolites NaA and CuA

Zeolite A (strictly Linde Type A, IZA code LTA) is one of the archetypal, cubic zeolite frameworks, crystallising in the the $Pm\bar{3}m$ spacegroup.[113] Adherence to the Löwenstein principle,[114] whereby Al and Si tetrahedral units alternate, results in a doubling of the unit cell size and symmetry change to $Fm\bar{3}c$. It is one of the more dense frameworks, with framework density[1] quoted as 12.9 T/1000Å^3, and comprised of 8-ring channels in all three crystallographic directions.

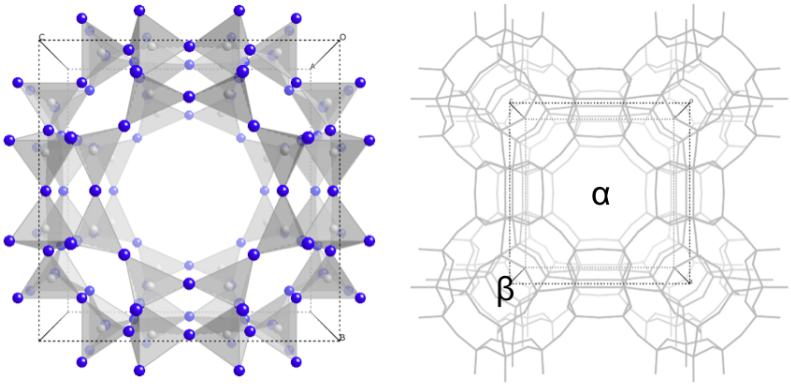

Figure 3.1: Framework schematic for zeolite A detailing *left*: unit cell and *right*: distribution of α- and β-cages. Si/Al tetrahedral units are shown grey, with oxygen atoms in blue.

As can be seen in figure 3.1, the interconnecting channels in zeolite A result in two cage environments, labelled α and β by convention. The larger α-cages exist at the centre of the crystallographic unit cell, and have apertures of 4-, 6- and 8-membered tetrahedral rings. The β-cages are smaller, comprising only 6- and

[1] ie the number of tetrahedral units per unit volume

4-membered rings, and are situated at each vertex of the cubic unit-cell.

For the non-silaceous forms of zeolite A, whereby there is a distribution of Si and Al in tetrahedral sites, the net negative charge of the framework is countered by the presence of extra-framework cations. Two forms of zeolite A were used for the zeolite studies in this thesis, NaA and CuA. The former has exclusively Na-cationic species, and the latter predominantly Cu(II)-cations (although full exchange to Cu(II) is rarely achieved, a predominately Cu(II)-containing zeolite A is termed CuA by convention in the literature).

The positioning of extra-framework cations in zeolite A are within the larger α-cages, with cations positioned in the centre of the 6-membered rings.[115] This is shown in figure 3.2 for Na and Cu(II)-cations, with stronger coordination of the Cu(II) to framework oxygen resulting in a puckering of the 6-membered ring.[116] For zeolites of high Al content, additional cations may be present distributed over crystallographic sites in the centre of the 8-membered ring face of the α-cages. It should be noted at this stage that the precise positioning of the extra-framework cations (and to an extent the framework itself) is variable with respect to the ring-faces and dependant upon additional species within the porous network.[117, 118, 119] Zeolite synthesis is almost exclusively hydrothermal, as will be detailed in the next subsection, and as such there is a large H_2O con-

tent within zeolite pores/cages. This water can coordinate to framework cations, drawing them slightly out of their ring environment, but is carefully removed for subsequent absorption reactions.

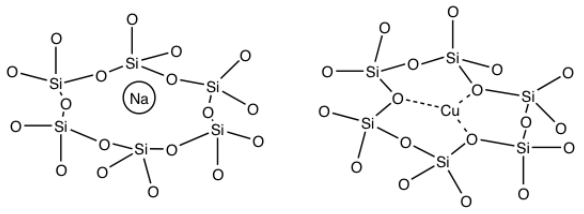

Figure 3.2: Diagram showing cation positions in 6-membered rings for zeolite A [116]

One final aspect of zeolite chemistry is worth noting here, and this is the concept of an electronic ground-state. Taking a zeolite as being comprised of an extended network of tetrahedral units, each of partial negative charge, the delocalisation results in a surface charge that is balanced by the uncoordinated (in the extreme case of purely electrostatic interaction between framework and cation) or weakly coordinated cationic species. The silyl bridges, the term for T-O-T vertex linkages whereby T is a tetrahedral Si/Al species, are themselves flexible[120, 121]. Whilst the internal angles of each tetrahedral unit has a defined energetic minimum, these silyl bridges can take a range of angles, commonly found to be between 130° and 170°. For each zeolite there is an average angle for each crystallographically independent silyl bridge, but the shallow potential for angular changes results in an ill-defined electronic ground-state for the system framework. This is particularly important for model calculations as described in chapter 5.

3.1.1 Synthesis, Exchange and Dehydration of Zeolite A

The synthetic routes to zeolite A are well documented in the literature, all operating under a simple hydrothermal principal of 'silica source, alumina source, water and base'.[2] For all zeolites, the initial synthesis is of the Na-form of zeolite A, NaA, and the procedures detailed by Thomson and Franklin,[55, 122] and Hopkins [123] (identical bar the use of a small quantity of tetramethylammonium hydroxide in addition to sodium hydroxide) were followed.

Initially 2.89g of sodium hydroxide (NaOH, Sigma Aldrich) was fully dissolved in 320 ml of deionised water, with the resultant solution divided equally in two. 160 ml of this solution was used to dissolve 33.03g of sodium aluminate ($NaAlO_2$, Sigma Aldrich); the other 160 ml being used to dissolve 61.92g of sodium metasilicate (Na_2SiO_3). The silicate solution was poured swiftly into the aluminate solution whist being stirred vigourously. The resultant gel was continually stirred and allowed to homogenise for 1 h. After this time, the gel was sealed in an airtight polypropylene container and heated at 372 K for 4 h.

The resultant suspension (a white solid within a clear solution) was removed from its heat source and allowed to cool to room temperature before being filtered under vacuum. The powdered white solid product was washed repeatedly with deionised water, and subsequently fully dried overnight at 383 K. Crystallinity and phase

[2] As zeolite chemistry operates almost exclusively around this principal, it is common within the zeolite community to use the truly awful term 'recipe' as opposed to synthetic procedure.

were confirmed as zeolite NaA by powder XRD, as seen in figure 3.3. The competing aluminosilicate phase, FAU, was estimated from the powder XRD as being <5% abundance in all cases. The Si : Al ratio was determined by elemental analysis (Warwick Analytical Service, using Inductively Coupled Plasma - Optical Emission Spectroscopy, ICP-OES) as 1.05 : 1.00.

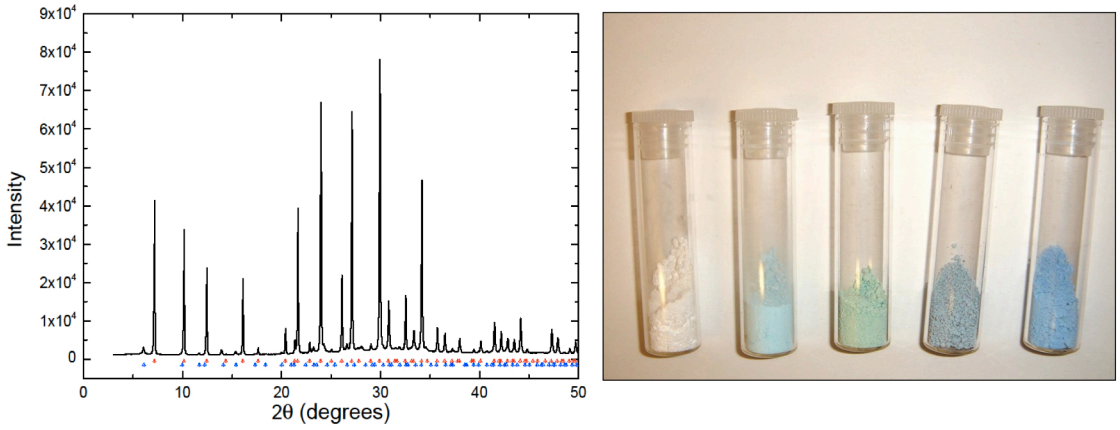

Figure 3.3: *Left*: Typical powder XRD for synthesised NaA (black) denoting reflections from LTA (red) and competing phase FAU (blue). *Right*: Colour changes for exchanged zeolite synthesis. From left to right: NaA (dehydrated), CuA·xH$_2$O, CuA (dehydrated), CuA·3NH$_3$. Far right is a more completely ammoniated CuA·xNH$_3$ system.

The Cu-exchanged form of zeolite A was produced from NaA following a standard cation-exchange reaction [124, 125, 126]. Approximately 15g of zeolite NaA was placed in a 0.05M solution of Cu(NO$_3$)$_2$ and stirred continuously at 313K for 3 hrs. The solution was then decanted and a fresh 0.05M solution introduced to the zeolite and the process repeated. This was done 3 times to ensure a high degree of exchange, determined by ICP-OES as Na : Cu 3.6 : 8.4. The zeolite was then filtered under vacuum, washed with deionised water and dried overnight at 383 K.

The zeolite, at this stage had taken on a green-blue colour. The colour changes involved in the the complete NaA·xH$_2$O→CuA·3NH$_3$ are also shown in figure 3.3.

Dehydration of zeolites is essential for neutron work, as the presence of H_2O protons swamps all spectra. This is besides the mere fact that absorbed H_2O may interact with both the zeolite and other absorbents. The dehydration process was thus conducted carefully for each zeolite sample prior to conduction of neutron experiments. The zeolite was placed in a vertical furnace and equilibrated under a vacuum of $< 10^{-3}$ mbar. This level of vacuum was maintained as the sample was slowly heated at a rate of $1\,\mathrm{K\,s^{-1}}$ in two steps. Initially the zeolite was heated and held at 483 K for 1 h, then to 573 K and held for 2 h. Care was taken to ensure the zeolite, a light, friable powder was kept within the heat-source. Post dehydration the NaA samples were, as expected, still white, whereas the CuA samples had altered colour from blue-green to a much lighter-green, indicating removal of cation-coordinated in addition to physisorbed H_2O. Confirmation of full dehydration was confirmed during neutron runs on the 'bare' zeolite systems.

3.1.2 Ammoniation of Zeolite A

There are few detailed examinations of the absorption isotherms of NH_3 within zeolite frameworks, particularly not for zeolite A. What is clear from isothermal studies on forms of zeolite NaX and NaY (FAU topology) [127, 128], calorimetric studies [129] and temperature programmed desorption [130], is that coordination is not stepwise, with control of the degree of ammoniation being particularly dif-

ficult and non-uniform. For the purposes of this work, however, only a low degree of absorption is required, in order to reflect initial coordination.

For the *ex situ* ammoniation process (the *in situ* INS measurements are detailed in chapter 4) the zeolite samples were placed under a 1 bar pressure of anhydrous NH_3 and equilibrated for 4 hrs at 353 K. The sample was then cooled to room temperature and placed under low vacuum ($\sim 10^{-1}$ mbar) for a further 1hr. Studies detailing full ammoniation are conducted at much higher temperatures, and for population of β cages large pressures of NH_3 are required[130]. The extent of ammoniation for samples has been determined by elemental analysis or comparative proton density neutron measurements. For the NaA·$x$$NH_3$ sample used for INS measurements elemental analysis yielded the stoichiometry NaA·4NH_3. Comparative proton density measurements against a pure H_2O standard was used to determine the extent of ammoniation for the CuA sample, yielding the stoichiometry CuA·3 NH_3.

3.2 SiGNa and SiGNaH

Silica Gel (SiG) is an amorphous form of silica, SiO_2, akin to zeolites in that it is composed of vertex-sharing SiO_4 tetrahedra. The porous networks throughout the gel structure are of dimensions on the order of nanometers rather than angstroms, and do not share the long-range interconnectivity of zeolites.

In 2005, Dye *et al* detailed the synthesis of a system whereby metallic sodium, Na^0, was absorbed into the SiG network, a compound henceforth denoted SiGNa.[131, 132] Interestingly, the state of Na^0 in SiGNa is itself amorphous or pertaining no long-range order within the system, with X-ray diffraction data resembling that of silica gel. ^{23}Na MAS NMR measurements reveals a coexistence of Na^0 and Na^+ [131], with the ratio of Na^0:Na^+ being witnessed to vary with temperature and loading of Na, with the lowest loading (not commercially available) or heating of the sample seen to favour Na^+. It should be noted that the state of the electron species is unknown, possibly existing as an electride. At room temperature, Na enters the silica gel with no discernible ionisation.

The overarching principle in the production of SiGNa is as a passivated source of Na^0 for organic synthesis (such as the Birch reduction) with compounds able to be handled briefly in air, yet still be highly reducing. In light of this, Sartbaeva *et al* reported the conversion of Na^0 to NaH in SiG by simple exposure of SiGNa to H_2.[133] The form of NaH within this product was of nanoparticulate crystallites embedded within the gel, with diameters between 20-50nm. This system is henceforth denoted SiGNaH.

For the DINS measurements detailed in chapter 5, SiGNa samples were purchased from Sigma Aldrich and SiGNaH provided by Sartbaeva. All samples were handled and stored under an inert Ar atmosphere.

3.3 LiF

LiF is a simple crystalline solid, familiar as an ionic archetype of the rock-salt. It is isostructural to NaH, each crystallising in the $Fm\bar{3}m$ spacegroup as shown in figure 3.4. Lattice parameters at room-temperature are a=b=c=4.027 Å, and $\alpha = \beta = \gamma = 90°$. There is negligible difference in lattice constants (<0.001Å) between ^{6}LiF and ^{7}LiF as shown by Thewlis [134]. LiF is non-hygroscopic and inert, thus is able to be handled under ambient conditions.

The ^{7}LiF sample used for DINS measurements detailed in chapter 5 was pur-

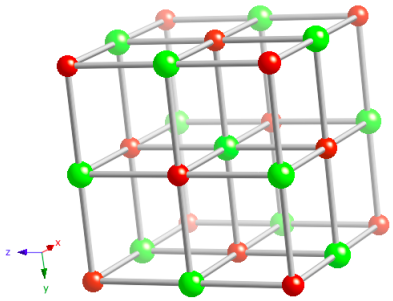

Figure 3.4: Structure of LiF/NaH unit cell detailing cation (red) and anion (green) positions

chased from the ISOTEC branch of Sigma-Aldrich, (P.N. 601497) specified as being 98% isotopically enriched.

3.4 $Li(NH_3)_4$

The systems formed upon the exposure of elemental Li to anhydrous NH_3 demonstrate one of the most venerable insulator to metal transitions known, with the basic model of solvated Li and solvated electron exiting within the NH_3 system [135]. These solutions of dissolved Li are conventionally described by their molar percentage of metal (MPM), with the saturated solution being that at 20 MPM, i.e. $Li(NH_3)_4$. The lower concentrations are semiconducting in nature, appearing as blue liquids, and undergo the transition to a bronze, metallic liquid at 8 MPM.

There exists extensive literature on the electronic state, or more precisely the nature of the valance/conduction electron in these Li-NH_3 systems (see for example the recent review article in reference [136]). For the neutron studies in this work this is not necessarily of import, but it is still interesting to note that at a mere 0.5 MPM the solvated electron species do not exist as singlet states, but rather have paired to such an extent as 90%. Only at 8 MPM can these electrons be described as fully delocalised in the system, with the dilute solutions comprising semi-localised electronic states, migrating through the liquid via what is understood to be a hopping mechanism. It is needless to state that the power of spin-chemical techniques such as NMR and EPR [137, 138, 139], particularly since the advent of pulsed methods [140], have played one of the most significant roles in understanding the nature of these electronic states. An outline of the phase diagram for Li-NH_3 solutions and solids is given in figure 3.5. It is partic-

ularly intriguing to notice that near the insulator-metal transition, there exists a liquid-liquid phase separation, whereby the metallic phase floats upon the denser semiconducting solution.

However, such an interesting electronic system, even in the liquid phase, can

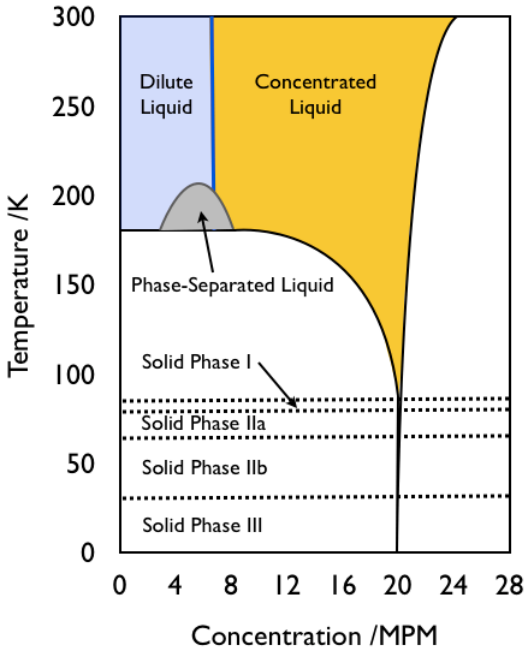

Figure 3.5: Schematic phase diagram for the Li-NH_3 system, adapted from reference [141]

be expected to give rise to fascinating structure and dynamics. The addition of an electron species to the system progressively disrupts the hydrogen-bonded NH_3 network, and is seen to be of a greater extent than if ionic solvation were the sole cause[142, 143]. It should be noted that any changes in the bulk properties of the NH_3 proton-binding, i.e. this hydrogen-bonded network, would be quantitatively reflected in a change in momentum distribution, as probed in deep-inelastic neu-

tron scattering experiments.

It has been shown that the NH_3 'cages' which solvate the electron species are constructed of multiple NH_3 units with their N atoms pointing out.[144] This has led to theoretical models whereby H↔H interactions between neighbouring NH_3 molecules exists, most recently in a density functional study utlising a molecular approach (whereby these cages are constructed as molecular subunits with the atomic orbitals as a basis set).[136]

A solid phase exists for the concentrated $Li(NH_3)_4$ solution,[145, 141] and is itself a truly fascinating compound.[3] To date it is the lowest melting point metal known, freezing at 88.8K as shown in figure 3.5. Cooling further results in a number of phase transitions, remarkable in such a small and cryogenic temperature range, whereby proton-ordering occurs in the cubic, plastic-phase I at 82.2K to give rise to a cubic phase IIa/IIb (differing phase suggested by change in resistivity at 69K). Skipper *et al* have demonstrated through QENS measurements that in phase I of the solid there still exists a level of diffusion in the proton dynamics,[146] with localisation to pure, stochastic rotational motion resulting in phases IIa and IIb. Finally an antiferromagnetic phase III forms by cooling to 25K. It is interesting to note that only phases II and III are witnessed in the case of $Li(ND_3)_4$;[147] a strong isotope effect that will have great bearings on the short-timescale dynamics

[3]The solidification of solutions of lower MPM by quenching result in glass-like metallic phases, named for their discoverer as Ogg glasses.

of the solid.

In addition to the extremely low melting point of $Li(NH_3)_4$, the large separation between molecular fragments (defined as the units giving rise to the eventually itinerant electron species) demonstrates the assignation of $Li(NH_3)_4$ as an expanded metal. At 40 K and 1 atm pressure the shortest separation of radical centres is 5.25Å [141].

3.4.1 $Li(NH_3)_4$ Sample Preparation and Handling

The synthesis of Li-NH_3 solutions are conceptually very simple, involving the condensation of anhydrous NH_3 onto Li metal in specific molar quantities. The handling of such is a different matter, particularly in neutron experiments whereby standard Al cans or teflon lining will be reduced by the resultant solutions. There is also the problem of sample decomposition if prepared at anything less than the highest purity.

Samples in this work were prepared using anhydrous NH_3 that underwent an additional purification process to ensure ostensibly complete removal of N_2 and H_2O. The specifically designed gasline setup is shown in figure 3.6.[4] A stoichiometric amount of NH_3 was condensed onto high purity Li metal (Sigma Aldrith, >99.99% purity) in a specially prepared quartz container of flat geometry, suitable for measurements on VESUVIO. The solid $Li(NH_3)_4$ phase was subsequently frozen, sealed

[4]Thanks is extended to Dr. M. Lodge for both expertise in synthesis and for figure preparation.

under vacuum and kept at cryogenic temperatures henceforth. The NH_3 and ND_3 samples were prepared *in situ*, being condensed into specialised Ti/Zr-alloy cans, as used in references [142, 146] to avoid any form of corrosion.

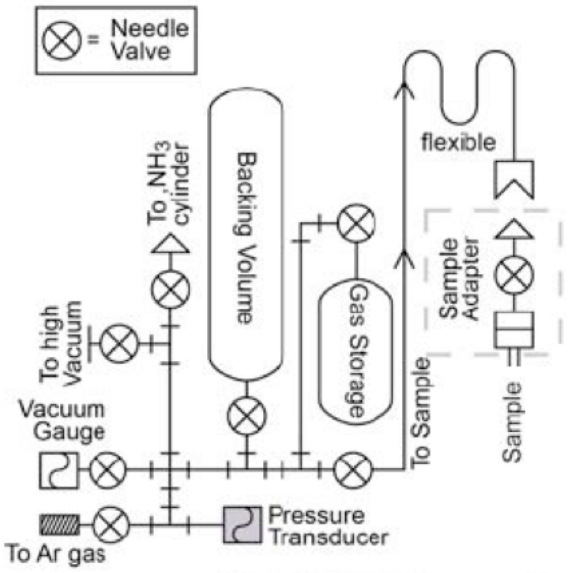

Figure 3.6: Schematic gas-line setup for $Li(NH_3)_4$ preparation.

Chapter 4

DINS of Mixed Mass Systems

"They both savoured the strange warm glow of being much more ignorant than ordinary people, who were only ignorant of ordinary things."

Terry Pratchett, *Equal Rites*

The emergence of deep inelastic neutron scattering as a spectroscopic technique was detailed in section 1.4. The theoretical framework encompassing the scattering of high energy neutrons in condensed matter, reproduced in section 2.1.3, demonstrated that for incident neutrons sufficiently high in energy, the impulse approximation is valid. As such, the wavelength of the neutron is small (shorter than interatomic spacing) thus no collective motion is examined and all scattering is incoherent in nature. For the high energy and momentum transfers of DINS, in the ranges $1\,\mathrm{eV} < \hbar\omega < 20\,\mathrm{eV}$ and $20\,\mathrm{\AA}^{-1} < q < 250\,\mathrm{\AA}^{-1}$ respectively for a VESUVIO measurement, scattering occurs from single nuclei with conservation of

the total kinetic energy and momentum of the neutron and nucleus [12].

This chapter is designed to extend the field of DINS to the measurement of nuclear momentum and kinetic energy for multiple masses in a system simultaneously, something that hitherto has not been demonstrated. Results for example systems shall be detailed, with the accuracy and pitfalls of such measurements discussed. Underlying the entirety of this chapter is a fundamental difference in the manner in which raw time-of-flight (ToF) data is refined and analysed, compared to 'standard' DINS measurements, and this is initially explained below.

4.1 Time of Flight Analysis and Mixed Masses

4.1.1 Count Rate on VESUVIO

From the definition of the partial differential cross section, $\frac{d2\sigma}{d\Omega dE_1}$ described in section 2.1.1, for neutrons scattering from a system of N identical atoms, the number of neutrons with incident energies in the range E_0 to $E_0 + dE_0$ detected with final energies in the range E_1 to $E_1 + dE_1$ can be given as [148]

$$C_D(E_0, E_1)dE_0dE_1 = I(E_0)D(E_1)\frac{d^2\sigma(E_0, E_1, \theta)}{d\Omega dE_1}d\Omega dE_0dE_1, \tag{4.1}$$

where the neutrons have been scattered into the solid angle, Ω, at a scattering angle, θ. C_D is the count number, $I(E_0)dE_0$ the number of incident neutron in a unit area with energies between E_0 and $E_0 + dE_0$, and $D(E_1)$ the probability of

the neutron of final energy E_1 being detected.

Defining the velocity of the scattered neutron as

$$\nu_1 = \sqrt{\frac{2E_1}{m}}, \tag{4.2}$$

with a similar expression for the velocity of the incident neutron, ν_0. m is the neutron mass. This enables the time of flight for the neutron, t, to be defined as

$$t = \frac{L_0}{\nu_0} + \frac{L_1}{\nu_1}, \tag{4.3}$$

where L_0 and L_1 are the incident and scattered flightpath respectively. Combining equations (4.2) and (4.3) and rearranging for E_0 gives

$$E_0(E_1, t) = \frac{m}{2}\left(\frac{L_0\nu_1}{\nu_1 t - L_1}\right)^2, \tag{4.4}$$

which can be substituted into equation (4.1), and integrated over time to yield an expression for the total number of detected neutrons in a period t to $t + dt$

$$C(t)dt = \int C_D[E_0(E_1, t), E_1]\frac{dE_0(t, E_1)}{dt}dE_1 dt. \tag{4.5}$$

As VESUVIO is an inverse geometry ToF spectrometer (see section 2.2.4) values for L_0, L_1 and θ are known, [1] and $D(E_1)$ can be defined as $D(E_R)\delta(E_1 - E_R)$, since the final energy, E_R is selected.

[1] This is under the assumption that the spectrometer is ideal, a wishful albeit useful fiction.

Combining equations (4.1), (4.4) and (4.5) yields the standard expression for the count-rate of an inverse geometry ToF spectrometer [149]

$$C(t) = 2\left(\frac{2}{m}\right)^{\frac{1}{2}} \frac{E_0^{\frac{3}{2}}}{L_0} I(E_0) D(E_R) N \frac{d^2\sigma}{d\Omega dE_1} d\Omega. \tag{4.6}$$

As has been noted in section 2.1.2, due to the short wavelength of incident epithermal neutrons in DINS, scattering occurs from single atomic species, and is entirely incoherent in nature. For the system of different masses, M, equation (4.6) becomes

$$C(t) = 2\left(\frac{2}{m}\right)^{\frac{1}{2}} \frac{E_0^{\frac{3}{2}}}{L_0} I(E_0) D(E_R) \sum_M N_M \frac{d^2\sigma_M}{d\Omega dE_1} d\Omega, \tag{4.7}$$

where σ_M is the total scattering cross-section for species M. Noting the relationship between partial differential scattering cross-section and $S(q,\omega)$, and substituting the form of the scattering law under the impulse approximation, IA, from equation (2.35) it can be shown that for isotropic scattering [4, 12]

$$\frac{d^2\sigma_M}{d\Omega dE_1} = \mid b_M \mid^2 \sqrt{\frac{E_1}{E_0}} S(q,\omega) = \mid b_M \mid^2 \sqrt{\frac{E_1}{E_0}} \frac{M}{q} J_M(y_M), \tag{4.8}$$

remembering from the definition of the neutron Compton profile, $J_M(y_M)$, in equation (2.39) and the y_M scaling factor. The entity b_M in the above expression is the total, 'bound' scattering length for nuclear species M.

By combining equations 5.7 and 5.8 the count rate for VESUVIO, operating under the IA, can be written

$$C(t) = \frac{E_0 I(E_0)}{q} \sum_M A_M M J_M(y_M), \tag{4.9}$$

where

$$A_M = \frac{2}{L_0} D(E_R) \sqrt{\frac{2E_R}{m}} \Delta\Omega N_M b_M^2. \tag{4.10}$$

4.1.2 Standard Fitting Routines

It should be noted above that the form of $C(t)$ is for an ideal inverse geometry ToF spectrometer, when in reality values for L_0, L_1, θ and E_1 are not exact, and more accurately described by a probability distribution, $P(L_0, L_1, \theta, E_1)$. This distribution governs the instrument resolution, but rather than evaluating a four-dimensional integral for each point of data, the instrument resolution is represented as a convolution in t, with a mass dependant resolution function $R_M(t)$ [48]

$$C(t) = \frac{E_0 I(E_0)}{q} \sum_M A_M M J_M(y_M) \otimes R_M(t). \tag{4.11}$$

For the fitting of experimental data in DINS, the form of $J_M(y_M)$ is assumed to have a normalised Gaussian form

$$J_M(y_M) = \frac{1}{\sqrt{2\pi\varsigma_M^2}} \exp\left(\frac{-y_M^2}{2\varsigma_M^2}\right), \tag{4.12}$$

related to the mean kinetic energy of the particle by[150]

$$\langle E_K \rangle = \frac{3\hbar^2 \varsigma_M^2}{2M}, \tag{4.13}$$

where ς_M defines the Gaussian width for each peak, the centroid of which is determined by M as derived in section 2.1.3, in y-space. It should be stressed that the form of equation (4.12) is for an isotropic system, independent of the direction of momentum transfer, $\hat{q}$, and in a harmonic potential. Anharmonicities leading to a departure from Gaussian behaviour in $J_M(y_M)$ are incorporated in DINS analysis when fitting to obtain $n(p)$. The isotropic neutron Compton profile is expanded in a set of Hermite polynomials, $H_n(y)$ with coefficients a_n [12, 151]

$$J_M(y_M) = \frac{\exp\left(\frac{-y_M^2}{2\varsigma_M^2}\right)}{\pi^{1/2}} \sum_n a_n H_{2n+1}(y). \tag{4.14}$$

Inversion of this Radon transform (from the relation of $J_M(y_M)$ to $n(p)$ in section 2.1.2) yields the fitted momentum distribution

$$n_M(p) = \frac{\exp\left(\frac{-p_M^2}{2\varsigma_M^2}\right)}{\pi^{3/2}} \sum_n 2^{2n+1} n! (-1)^n a_n L_n^{l+1/2}(p^2), \tag{4.15}$$

where $L_n^{l+1/2}(p^2)$ is a Laguerre polynomial.

To summarise; for the fitting of DINS data, two variables are fitted for each mass, M, in the reduced ToF data. These are the Gaussian width, ς_M, of the neutron Compton profile (equation 5.12) and the integrated peak intensity (or amplitude

factor), A_M (equation 5.10). The different approach developed in this thesis, compared to previous isotropic DINS studies, concerns the expression for A_M.

4.1.3 The Case of Multiple Masses

Recapping from section 2.1.4, it was shown that for a species of mass M within the framework of the IA, the maximum of S($\mathbf{q}$, ω), for a given value of q is given by $\hbar q^2/2M$. Due to the mass of the proton being equivalent to that of the neutron, it was demonstrated that scattering from protons only occurs for angles $2\theta < 90°$, whereas for heavier masses, scattering occurs across the full range of $0° < 2\theta < 180°$. It was demonstrated in equation 2.37, and is shown schematically in figure 4.1 that the separation of maxima for two masses, $M_1 < M_2$, increases with scattering angle. Thus, for the examination of proton momentum, only the forward scattering banks of VESUVIO are used, whereas for heavier species the full 2θ range can be examined.

There is, however, an inherent problem in the study of heavy masses, and that is the rapid decrease in the separation of peak maxima with increasing mass. The distinction of intensity arising from a deuteron is easily distinguishable in ToF to that from Li, for example, but the same cannot be said to be true when examining C in conjunction with N. Even at larger 2θ values a supposition of peaks occurs, and thus a single 'peak' in the backscattering range on VESUVIO invariably requires decomposing into those of its constituent masses.

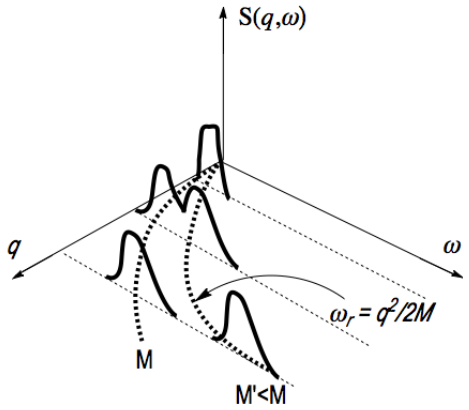

Figure 4.1: Demonstration of increased separation of mass-specific contributions to the structure factor in DINS, with q and therefore detector angle. Figure adapted from reference [12]

Figure 4.2 demonstrates this problem with the example case of three masses, $M_1 < M_2 < M_3$. In the ToF spectrum for a detector at given angle, θ (and thus a given value for q), each mass will give rise to a gaussian, with respective maxima at $\hbar q^2/2M_i$. In order to fit the resultant, measured spectrum (shown by the red line), each gaussian will have to be fitted, refining both width, ς_M (equation5.12) and amplitude factor, A_M (equation 5.10). Thus for three masses there are six variables to refine to give a best-fit to one measured peak. Since fitting this many variables, or more for more complex systems, has been described as a 'black art',[2] it is necessary to reduce this number if possible.

As seen in the preceding section, whilst ς_M is a direct measurement of the width of the momentum distribution for mass M in y-space (being related to the oscilla-

[2]Dr. J. Mayers, during many private communications on this topic

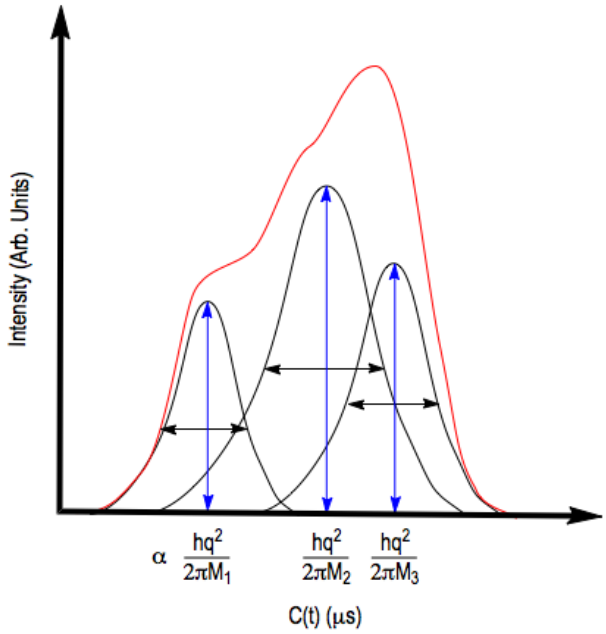

Figure 4.2: Schematic representation of fitting parameters for raw VESUVIO ToF data. The red line is the 'measured' spectrum, with black lines denoting constituent gaussians for each mass, centered on values proportional to those shown. Blue arrows represent the gaussian peak intensity, and black arrows denote gaussian widths.

tion frequency and mass of the nucleus), A_M is directly proportional to the total scattering cross-section of M, multiplied by the number of nuclei in the system (equation 4.10). Notably, all other terms in the expression for A_M are instrument parameters. In a DINS measurement, therefore, a comparison of A_M for each mass will yield the sample stoichiometry through the relation

$$\frac{A_1}{A_2} = \frac{N_1 \sigma_1^T}{N_2 \sigma_2^T}, \tag{4.16}$$

where N_i is the number of atoms of species i and σ_i^T is the relevant total neutron scattering cross-section.

If the sample stoichiometry is known, however, as if often the case in chemical investigations, values for N and thus A_M, or rather the ratio of A_M can be fixed in subsequent fitting-routines, effectively halving the number of variables as only ς_M are allowed to refine.

With this approach at mind, this chapter will present results on a number of systems with the aim of using DINS to address specific properties of each. These studies may be into the nature of the system under investigation, or into the accuracy and ability of the VESUVIO instrument in the investigation of heavy masses.

4.2 NaH, SiGNaH and SiGNa: DINS of Two-Tiered Systems

Section 3.2 discussed the chemical properties and synthetic routes to preparing SiGNa and SiGNaH. To briefly recap, SiGNa is the designated name for a system of Na-metal, encapsulated within a matrix of amorphous silica (SiO_2) gel [131]. There is some evidence for the surface 'layer' of this amorphous Na being ionised near close approaches with the Si-O-Si bridges of the gel, with a slight net negative charge across the O-Na gel-metal boundary.

SiGNaH is the hydride product of exposing SiGNa to H_2, and is noticeably different in structure [133]. Whereas the Na in SiGNa is amorphous in nature, the

NaH in SiGNaH exists as crystalline nanoparticles embedded within the silica gel matrix. These particles are of the order of 20-50 nm in diameter. The INS spectra for SiGNaH show discrepancies compared to those of bulk NaH, but as has been stated, these are in regions of phonon energy where the resolution of TOSCA is more questionable than areas for each spectra that match. This DINS study was designed in order to further elucidate whether there is any significant difference in the proton environment in SiGNaH and NaH, bearing in mind the resolution of VESUVIO for protons is particularly high, where any difference in environment will result in a change in proton momentum distribution.

It can immediately be seen why a DINS study on these systems will be fundamentally different from previous measurements discussed in section 1.4. The SiGNa and SiGNaH materials can be envisioned as being two-tiered, with the encapsulating gel, SiO_2 being essentially the same in each (although this is not strictly true, considering O-encapsulated interactions) and the encapsulated system, the amorphous Na and nanoparticulate NaH respectively, being distinctly different. Whilst the examination of scattering from protons in NaH and SiGNaH is readily performed in DINS, with the intensity separated from all other masses in ToF, the examination of other masses (O, Na and Si) in each of the three systems will require the application of the method outlined above in section 4.1.

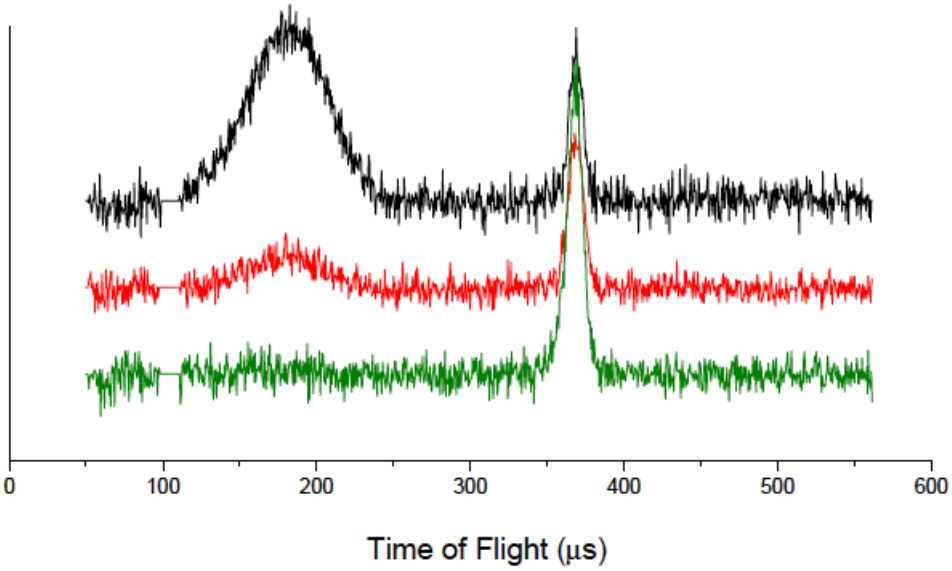

Figure 4.3: DINS ToF spectra for bulk NaH (black), SiGNaH (red) and SiGNa (green). Data are presented offset, with arbitrary intensity, and are collected from only the first bank of detectors on VESUVIO

4.2.1 Forward Scattering

Figure 4.3 presents example forward-scattering spectra for each of bulk NaH, SiGNa and SiGNaH. It can be remembered from section 2.2.4 that the VESUVIO instrument comprises six forward detector banks (182 detectors in total) in addition to those for backscattering. The data presented in figure 4.3 are only from the first detector bank. Following standard procedure [148] the data have been corrected for multiple-scattering,[152] and for the gamma background arising from gamma-radiation from secondary gold foils in the forward scattering YAP (yttrium aluminium perovskite) detector array.[153] The break in data in figure 4.3 around 100 μs is due to a 60 eV Au resonance appearing in all data from VESUVIO, which is simply removed for all forward scattering spectra, being at shorter ToF values

than any scattering occurring from the sample.

In each of the three example spectra, there is a peak occurring between ToF values of 350-400 μs. This is the peak containing a supposition of scattering from all masses in the system, with the exception of the proton in SiGNaH and NaH. As was outlined in sections 2.1.3 and 5.1, the separation of signal from different masses increases with scattering angle, and thus this peak is not fitted in forward scattering (particularly not for the low angular range in the first detector bank). The peak appearing at lower ToF in figure 4.3 is that from the proton, and thus is only seen in the systems containing this nucleus, i.e. SiGNaH and NaH. The greater intensity for NaH reflects the greater stoichiometric percentage of the proton in this sample, compared to SiGNaH, and is a suitable exemplification of the link between peak intensity in DINS and the number of atoms (equation 4.15).

Before detailing the investigation of heavier masses, it is felicitous at this stage to concentrate on the proton signal, and to examine whether there is indeed a difference in environment between bulk NaH and its nanoparticulate, encapsulated form in SiGNaH, hinted at in the INS measurements reported.

Following the standard treatment outlined in section 5.1, figure 4.4 presents the resultant neutron Compton profiles, $J(y)$ for the proton in both NaH and SiGNaH, for the angular range $30° < 2\theta < 70°$, in addition to the symmetrized raw-data in y-space. It can immediately be seen that the distributions of $J(y)$ in each case are

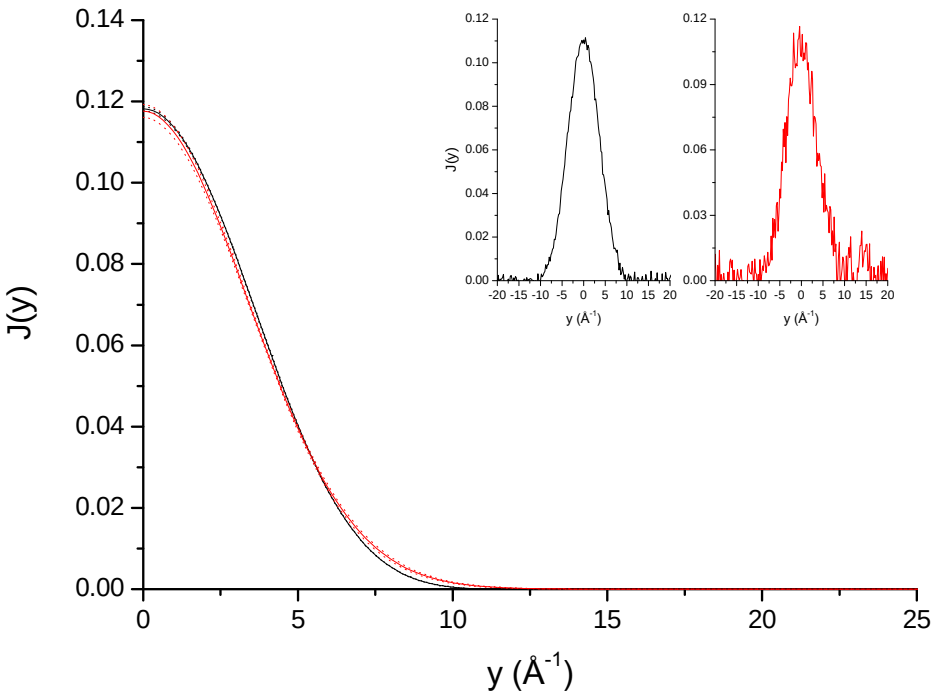

Figure 4.4: Neutron Compton Profile of bulk NaH (black) and SiGNaH (red). Error limits are shown as dashed lines, but are too small to see at higher values for $J(y)$. Inset: Raw data in y-space.

very similar. Due to the higher statistical scattering from protons in NaH, the error limits are particularly low, whereas in the case of SiGNaH the error at low values for y render $J(y)$ indistinguishable from that of NaH at these limits. It should be noted that the absolute count rates in each case are high, with integrated proton currents of 2267.2 μAh and 2650.8 μAh for bulk NaH and SiGNaH respectively.

The profile width of $J(y)$, ς_H, for bulk NaH is measured as 3.323 $\pm$ 0.015 Å^{-1}, and that for SiGNaH is 3.280 $\pm$ 0.070 Å^{-1}. Noting the relation between ς_H and

the mean kinetic energy of the proton, $\langle E_K \rangle_H$, shown in equation 4.13, values for $\langle E_K \rangle_H$ can be calculated as 69.40 ± 0.70 meV for NaH and 66.18 ± 3.49 meV for SiGNaH. These values are in excellent agreement with that calculated from INS data for bulk NaH reported by Colognesi *et al*, which puts the value at 66.39 meV [36]. It should be noted that despite this agreement, DINS is a more sensitive and direct probe for $\langle E_K \rangle_H$, and our measurements were performed at 4 K, rather than the 20 K used for INS.

In order to fully elucidate whether there is a difference in momentum distribution between NaH and SiGNaH, the radial momentum distribution expressed by $[p^2 n(p)]$ was calculated and is presented in figure 4.5.

The radial momentum distribution for the protons would be expected to emphasise any small differences in $J(y)$, and as it can be seen from figure 4.5 this is indeed the case. There is a shift in line shape to higher momentum values in SiGNaH, compared to bulk NaH, and whilst this difference is slight, it is still greater than experimental error. This shift to higher momentum states, and the narrowing of ς_H, is indicative of an increased potential experienced by the proton, or rather an increased localisation through the relationship between momentum and position described by the Heisenberg uncertainty principal.

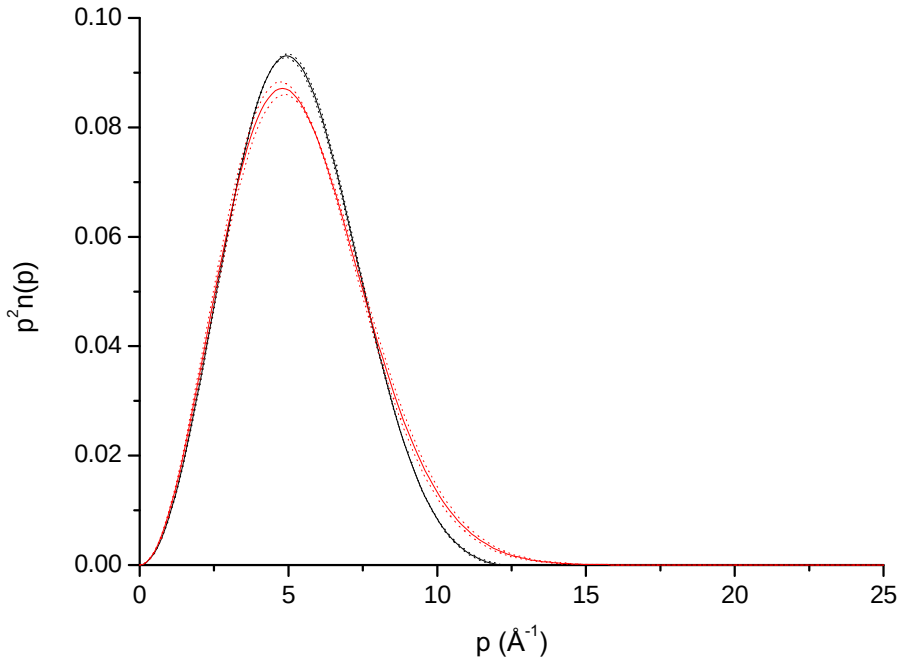

Figure 4.5: Radial momentum distributions, $p^2n(p)$, for bulk NaH (black) and SiGNaH (red). Error limits are shown by dashed lines.

4.2.2 Backscattering

Turning to the analysis of data from the backscattering detectors, the approach to heavier masses is distinctly different than for the protons above. In the case of SiGNa and SiGNaH, the measured peak in ToF consists of a summation of peaks from O, Na and Si in addition to that of the Al sample container. For NaH the peak will only include intensity for Na and Al, noting in all cases that no scattering from protons appears in backscattering angles due to the mass of the proton being equivalent to that of the incident neutron.

In order to refine the raw ToF data for backscattering, multiple scattering events must first be calculated and subtracted out, since it has been shown that multiple scattering from protons results in an increased intensity at ToF values for scattering from heavier masses, resulting in a non-zero background. The calculation of this intensity by Monte-Carlo integration is dependant on sample thickness and geometry, with the removal of such from weak and moderate scattering samples (a definition in which the systems of this study fall) being standard procedure during the VESUVIO analysis protocols [154].

The subtraction of Al intensity is now also standard procedure, if an empty can run is included at the temperatures studied. It has been shown that multiple scattering effects in the empty can is negligible (*cf.* section 4.3).

Figure 4.6 is akin to figure 4.3 and shows example raw data from the first bank of back scattering detectors on VESUVIO, for the samples of bulk NaH, SiGNaH and SiGNa. For backscattering, each sample gives rise to a single peak, or rather the supposition of peaks for each mass. Even for bulk NaH this peak includes intensity from Al and Na, and for SiGNa and SiGNaH there are also contributions from Si and O. Once the sample can (for all intents and purposes the signal from Al) has been removed from the samples, the technique of fixing relative stoichiometry discussed in section 4.1.3 can be used to determine the profile widths for each mass. Since the relative position of these peaks changes with angle in ToF, these widths are fitted for each of the 134 detectors on VESUVIO separately, with deviations

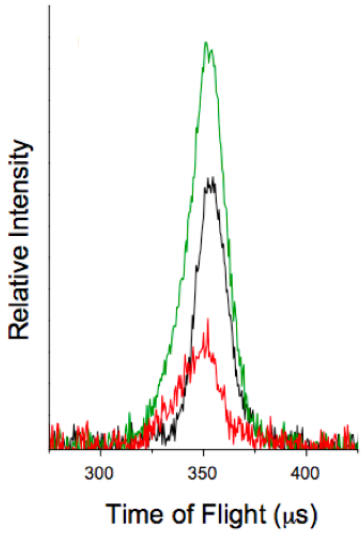

Figure 4.6: Raw data for bank 1 of backscattering detectors on VESUVIO for bulk NaH (black), SiGNaH (red) and SiGNa (green).

Table 4.1: *Summary of profile widths ($Å^{-1}$) and proton kinetic energies (meV)*

System	H width	$\langle$ K.E. $\rangle_{proton}$	Na width	Si width	O width
NaH (bulk)	3.323 ± 0.015	69.40 ± 0.70	7.242 ± 0.365		
SiGNaH	3.280 ± 0.070	66.18 ± 3.49	6.263 ± 0.709	12.473 ± 2.954	11.045 ± 0.529
SiGNa			5.329 ± 0.243	12.250 ± 1.543	12.779 ± 0.284
NaH (INS, 20 K)[36]		66.39			

from the mean calculated along with average values. Any visible presentation of the data presented across a sum of detectors are thus physically meaningless, but do serve as a point of clarity. Figure 4.7 gives an indication of fit across one of the backscattering detector banks on VESUVIO.

The resultant profile width analyses for each of the masses in bulk NaH, SiGNa and SiGNaH including the proton are presented in table 4.1, and it is here that

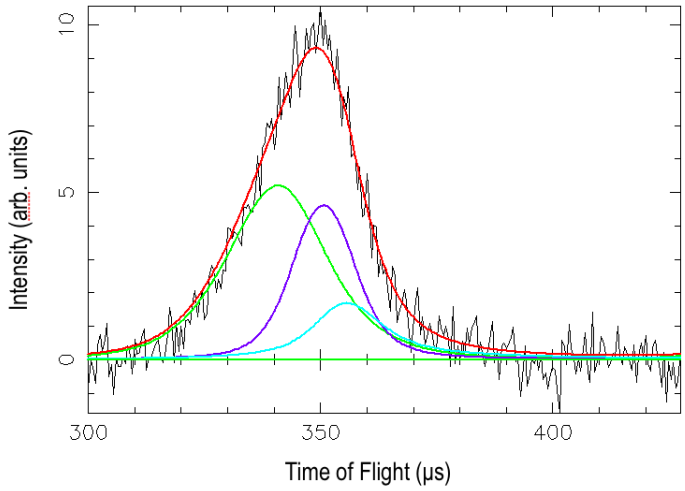

Figure 4.7: Summated fit (red) for refined backscattering data (black) of SiGNa, showing peaks arising from O (green), Na (purple) and Si (turquoise).

the elegance of DINS begins to be seen. Examining the Na nucleus, it is shown that the fitted profile width is lower in the case of SiGNa than in bulk NaH, with the value for SiGNaH lying approximately half way between the two. The first internal check in this analysis is that the value of 5.427 Å^{-1} for ς_{Na} in SiGNa is in agreement with the width extracted from elemental Na by Fulton *et al* [33], which was approximately 5.8 Å^{-1} at 30 K. It should be noted that the sample in the Fulton study was for polycrystalline Na, whereas the nature of Na in SiGNa is amorphous. Both this fact coupled with the lower temperature of our measurement would be concordant with a slightly narrower profile width. Fulton *et al* were unable to determine a change in profile width with phase on the EVS spectrometer, and it is therefore little surprise that our value lies within their limits.[3]

[3]Whether the VESUVIO instrument is now able to do this remains to be seen, but in light of results presented in the next section it is probable.

The value of ς_{Na} in bulk NaH is distinctly different from that in SiGNa, being noticeably higher, reflecting an increased localisation of the nucleus. This is expected from the increased potential experienced by the Na^+ nuclei in the ionic cubic hydride salt, compared to the metallic, amorphous state in SiGNa.

Of particular import is the value for ς_{Na} in SiGNaH, wherein the Na exists in two environments, with 50% existing as nanocrystaline NaH, and the other 50% remaining as amorphous Na metal. Since the profile width would give an average of these two environments, to witness a value half-way between the limits of bulk NaH and SiGNa lends great credence to the technique of stoichiometric fixing in DINS data analysis.

Further checks can be made for this technique, by examining values for profile widths of O and Si in the SiGNa and SiGNaH samples in table 5.1. Since the Si local environment does not change between the two gel samples, values for ς_{Si} may be expected to remain constant, and within error this does seem to be the case. The same cannot necessarily be said of the O environment, since there is some evidence for the ionisation of Na at the Na-Gel interface in SiGNa, which would lead to a net negative charge on the O of the Gel at this interface. The fact that a slightly higher value for ς_O is seen in SiGNa suggests that the average O nuclei in SiGNa are slightly more localised, in agreement with this net charge transfer, but it must be stressed that the difference in width is very slight. Any

grandiose claim of the significance of this difference, whilst concordant with the system model, should be taken with the proverbial grain of salt at this stage.

What is certainly evident from this section, is the applicability of DINS to systems containing multiple masses. It has been demonstrated that despite DINS being a technique able to examine the subtleties in the nuclear momentum states of the proton[4], a truly chemical reasoning can be linked to the momentum width of heavier masses if the stoichiometry of the sample is able to be fixed in the analysis.

[4]The opportunity should be taken here to reuse the term 'quantum snapshot'

4.3 LiF: The Accuracy of Stoichiometric Fixing

The previous section detailed a study on a complex, multi-mass system, whereby DINS was used to demonstrate not only a difference in proton momentum between bulk and nanoparticulate NaH, but to also refine the backscattering data to yield information on heavier masses. The standard protocols for data analysis on the VESUVIO instrument were followed, with the additional constraint that relative stoichiometry was not allowed to vary in the fitting of heavy-mass signal for each detector.

In a sense the SiGNaH study was a proof of concept, as chemical intuition was seen to agree with the measured momentum widths for these heavier masses. It must be stressed, however, that the results gave no idea of the overall accuracy in heavy-mass momentum widths, other than that for Na^0 being in close agreement with the previous study by Fulton *et al* [33]. In order to gain insight into the absolute accuracy of VESUVIO measurements and refinement protocols, a much simpler example has been designed, and tested in a more rigorous way than internal consistency.

As described in section 3.3, LiF is a simple, ionic archetype of the rock-salt, $Fm\bar{3}m$ space group. In the framework of a DINS study, there are two particular properties of LiF that are beneficial, in addition to its ostensibly simple structural and electronic characteristics. Firstly, ^{19}F is the only naturally occurring isotope of

fluorine, which when coupled with an isotopic enrichment of Li as ^{7}Li, results in the sample itself being binary in the sense of scattering species. The absorption cross section for each isotope is also negligible, particularly at the high incident neutron energies in DINS [155]. Secondly, the mass difference of the two isotopes renders them almost completely separable at backscattering angles, with overlap only in the regions of the wings of each gaussian in time-of-flight.

A DINS study of ^{7}LiF thus appears simple, but brings with it two complications. Firstly is the low total scattering cross-sections for both ^{19}F and particularly ^{7}Li, at 4.018 and 1.4 barn respectively. Furthermore, the sample environment of VESUVIO ensures that there is always a signal arising from Al, in particular for the sample can and cryostat (each predominantly Al and modelled well by a single, ^{27}Al peak). Thus this binary sample is in reality a 3-mass problem, with overlap of the ^{19}F and ^{27}Al signal.

4.3.1 Sample Environment

A large sample size of 10g of enriched LiF was used to compensate for the low total scattering cross sections of ^{7}Li and ^{19}F (henceforth referred to as Li and F, with isotopic enrichment assumed in the text). A single polycrystalline sample was used for all measurements, and was loaded within an Al can of flat geometry, standard for VESUVIO measurements. The sample environment was constant for each temperature, from cryogenic to ambient conditions, with the sample contained within an Al cryostat. Long runtimes of over 10 hours were conducted with an

average integrated proton currents for a given run being 1800 μAh. The sample temperature was measured separately to the cryostat for each case.

4.3.2 Multiple Scattering Corrections To the Raw Data

Due to the backscattering detectors on VESUVIO being comprised of ^{6}Li, they are not susceptible to γ-radiation from secondary gold foils during measurements, and thus the most crucial correction to the raw data is that for multiple scattering. In section 5.2 it was stated that multiple scattering contributions to the data are present as a non-zero background in forward scattering, with the shape at backscattering being essentially sample-independent for isotropic samples placed in the beam in a flat geometry [152, 154]. This is true for weak scatterers where $< 40\%$ of the incident beam is scattered by the sample. For all temperatures measured in this study, the transmission of the beam was measured as within the range $0.934 - 0.941$, where a value of 1.000 would represent total transmission of the beam. In order to maintain consistency for each temperature, an average value of 0.937 (6.3% scattering) was used for sample transmission in each multiple-scattering calculation. These calculations were done separately for each temperature, using the protocols detailed in reference [152].

Figure 4.8 demonstrates the contribution of multiple scattering for a given temperature, shown for 4 K. As can be seen, the multiple scattering appears as an asymmetric peak beneath the measured data. Contrary to that scattering documented within the proton peak, the shape of multiple scattering can thus be

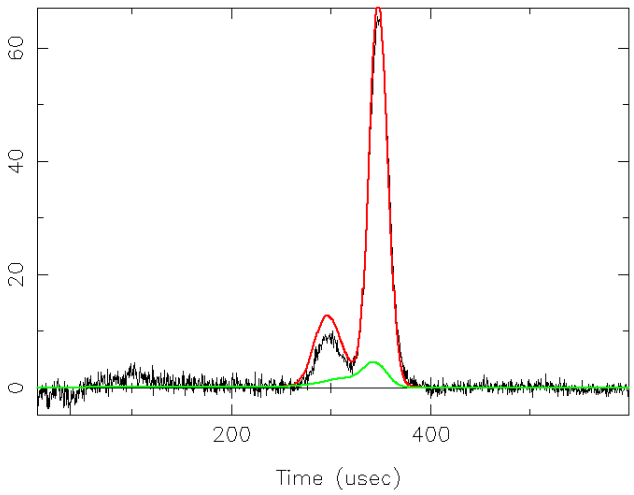

Figure 4.8: Example multiple scattering (MS) contribution to the raw data, showing calculated MS (green), calculated total scattering (red) and signal (black).

expected to be important to the eventual determination of momentum widths for heavier masses. This is particularly true for masses where scattering is weak, such as Li. However, as must be stressed, the contribution for multiple scattering has been kept uniform throughout this study, at a factor of 1.1 of that calculated by the Monte Carlo simulation. This is within error for the calculation. The secondary gold resonance at 100 μs can also be seen in figure 4.8.

4.3.3 Momentum Width Analysis

The stoichiometric fixing technique discussed in section 5.1.3 has been utilised in analysing the corrected backscattering data for LiF for various temperatures in the range 4 K-300 K. A nominal Al content has been determined by relaxation of the 4 K data, under the restriction that the Li:F ratio is fixed, and is itself subsequently fixed for higher temperatures. The choice of calculating the Al content

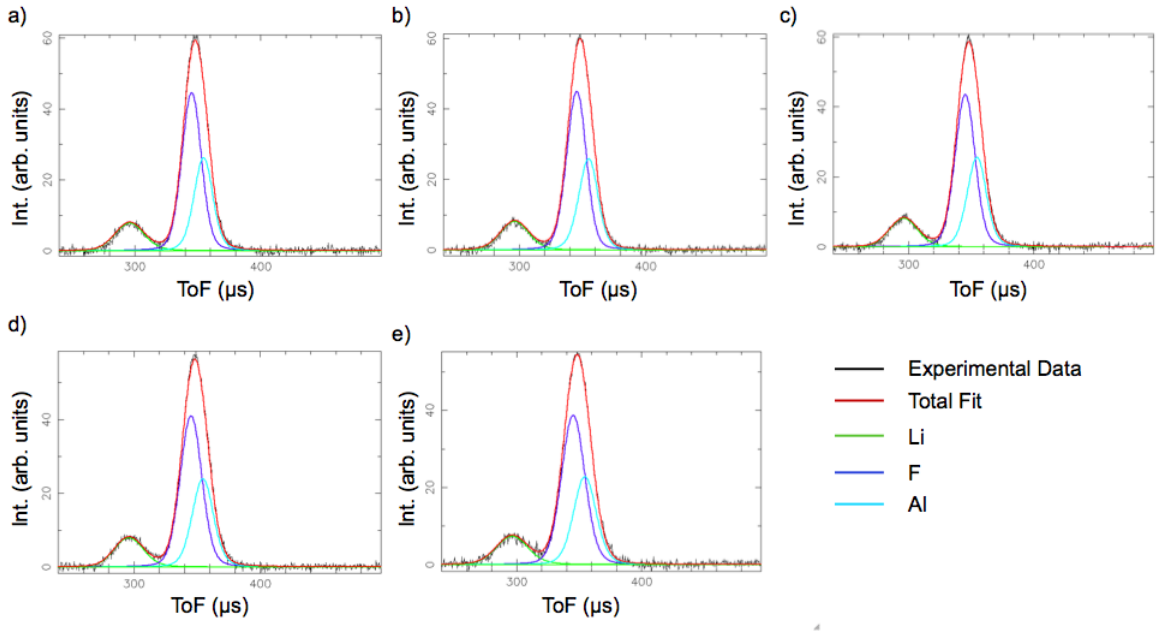

Figure 4.9: Total fits across all backscattering detectors for LiF at temperatures a) 4K, b) 50 K, c) 100 K, d) 200 K and e) 300 K.

for the 4 K data is due to the gaussian peaks for each mass being expected to have widths at their most narrow at this lowest temperature, and thus in principal be most accurately separable in the fitting process.

Figure 4.9 presents total fits across all detectors for LiF (plus the Al environmental contribution) for each temperature. It must be stressed that a summation across the total angular range of detectors is not strictly physical, in that the recoil line of each mass shifts to higher ToF at higher angle. Figure 4.9 is therefore presented merely as a guide to the eye for the accuracy of fit. As can be seen, the spectral data fit well with gaussian contributions from Li, F and Al. As currently stands,

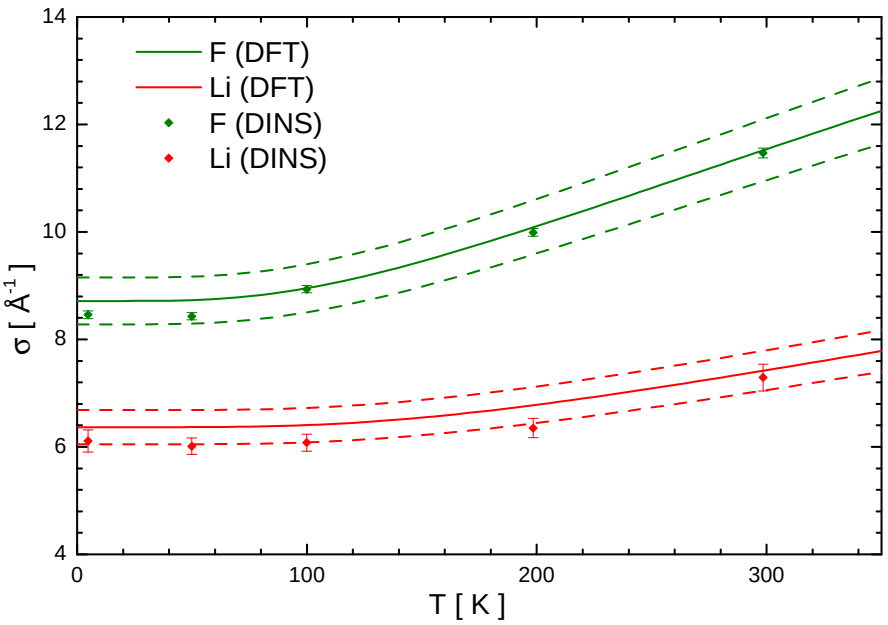

Figure 4.10: Measured and calculated neutron Compton profile widths for Li and F in LiF. Dotted lines indicate a 5% error on the calculated quasiharmonic values.

a full separation of Li signal from others is not readily calculable, due to overlap in gaussian tail regions with signal from F. Variation from gaussian behaviour in $J_{Li}(y)$ is thus also not possible. It should be noted, however, that the low σ for Li renders the statistics of measurement unlikely to measure such small variations as may be expected for deviations from harmonic behaviour.

The measurable variables of interest in this study are the momentum widths, ς_{Li} and ς_F, and these are collected together for each temperature in figure 4.10. It can be seen that across the temperature range from 4 K to 300 K there is little variation in ς_{Li}, within error, with noticeable increases only for 200 K and 300 K.

Variation in ς_F is more pronounced, and noticeable for values>50 K.

Also included in figure 4.10 are theoretical calculations for ς_{Li} and ς_F in LiF, at the level of fully periodic DFT and DFPT under a quasiharmonic approximation. These calculated values are independent of measured values, and do not represent a fit to the experimental data. Details of the calculation and accuracy can be found in Appendix A.[5]

Due to the complexity of calculating momentum states across temperature for even simple systems, a 5% error has been indicated by dashed lines in figure 4.10. This error margin was estimated based on the magnitude of the discrepancy between experimental and computed vibrational frequencies shown in figure A.1. The experimentally derived values agree well with calculation in both trend and absolute value, being within 1-6% for all temperatures. A result this close to theory for a polycrystalline sample of mixed masses, each of which is a poor scatterer of neutrons, is extremely promising for the application of DINS to masses heavier than H or He.

The ability to measure the momentum width, and thus mean kinetic energy of Li is particularly interesting. Li is a light nucleus, with low electron density for dynamical examinations by photon-based techniques, particularly when present in systems composed of heavier elements. In these systems a similar problem is

[5]All calculations on LiF have been performed by Dr. Michelle Ceriotti, University of Oxford

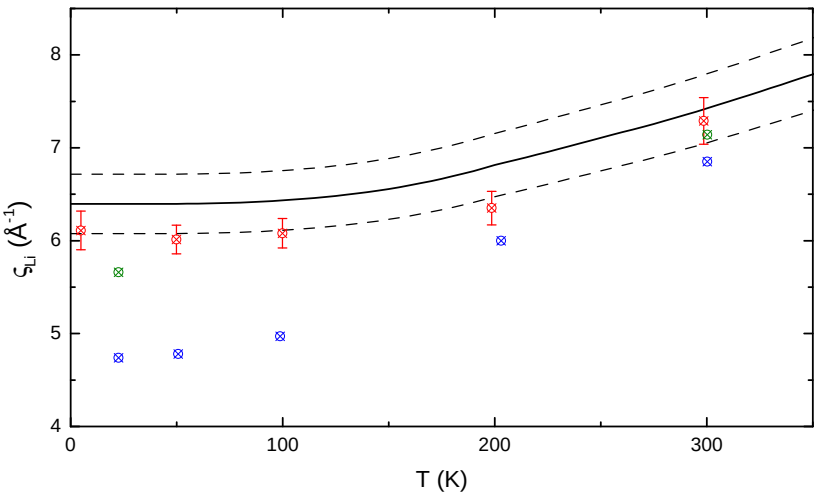

Figure 4.11: ς_{Li} in LiF (red, present study), LiH (green) and Li (blue). The black line represents a quasiharmonic calculation for LiF with 5% error indicated.

approached as that for protons. However, a total neutron scattering cross section of 1.4 barn is comparable to that of Al (1.503 barn), the element ubiquitous in neutron scattering machinery, coined as being 'virtual invisible to neutrons'. By virtue of its light mass, however, within the framework of DINS the Li signal should at the least be isolatable.

Figure 4.10 shows that for LiF, these is little variation in ς_{Li} across the ∼300 K temperature range measured, in agreement with theory. The slight increase above 100 K also matches calculation in both trend and absolute value. A simple question that must be asked, however, is whether these values for ς_{Li} are not unique to LiF, but common for the Li nucleus in general, considering the inherent error in

Table 4.2: *Mean Kinetic Energies (meV) and Effective Temperature (K) for Li and F in LiF*

T (K)	$\langle$ K.E. $\rangle_{Li}$	$\langle$ K.E. $\rangle_{F}$	T_{Li}^{eff}	T_{F}^{eff}
4.80	33.44±2.85	24.93±0.43	258.71±22.02	192.88±3.33
49.84	32.39±1.66	24.76±0.39	250.56±12.83	191.52±3.00
99.90	33.11±1.72	27.81±0.42	256.17±13.31	215.10±3.23
198.50	36.13±2.06	34.77±0.50	279.52±15.93	268.96±3.88
298.50	47.61±2.28	45.83±0.72	368.28±25.36	354.55±5.56

examining Li compared to H/D. Few measurements or theoretic calculations of ς_{Li} exist currently, but two in particular can be used to compare with the above LiF data, a DINS study of elemental ^{7}Li conducted on the original setup of VESUVIO (EVS) [32], and a theoretical paper on ^{7}LiH (isostructural to LiF) [156]. These results are collected in figure 4.11, and follow the expected trend LiF>LiH>Li.

Values for ς_M have been transformed into mean kinetic energies, $\langle$K.E.$\rangle_M$, for Li and F at each measured temperature according to equation 4.13, and these are detailed in table 4.2. Also listed are values for Effective Temperatures, T_M^{eff}, defined as the temperature of the particle computed purely from its momentum. At higher temperatures this converges with the sample temperature, but at lower temperatures T_M^{eff} is larger due to zero-point motion.

One note of caution has become apparent from measurements on LiF, and that is the sample environment contribution to S(q, ω). The measurements reported above were refined under the approximation that the sample can, cryostat and environmental contributions can be modelled as a single peak, for ^{27}Al, in ToF.

Each of these has very high Al-content, and thus the approximation holds.[6].

Measurements were obtained for an empty can within the cryostat at each temperature measured for LiF, with the initial aim of removing the sample can, as was done for the SiGNaH study. However, upon simple subtraction of these can spectra from the measured LiF data, the momentum widths for Li in particular were seen to not refine adequately. The fluorine widths were within error of the refinements with can included, with the same trend in width resulting. The Li:F stoichiometric ratio, however, was demonstrably low if allowed to refine freely and inconsistent throughout the temperature range, something that is obviously incorrect for a single, simple sample.

Current reasoning for the inaccuracy of can subtraction in LiF is simply due to the lower statistics of measuring such weak scatterers. Current plans are in place to run samples of stronger scatterers (in particular the N-containing binary salts, Li_3N and GaN) to determine the accuracy and limitation of Al-can subtraction.

[6]This has been demonstrated in unreported measurements at ISIS by both ourselves and Dr. Jerry Mayers.

4.4 Proton Momentum Distributions in $Li(NH_3)_4$

A brief background to the chemistry and physical properties (and indeed history) of the Li-NH_3 system was detailed in section 3.4. Previous neutron scattering experiments have characterised both the structure of the concentrated solid, $Li(ND_3)_4$ and common molecular motifs in the solutions of lower MPM [147, 142, 143]. Dynamical studies on the solid metal utilising cold neutrons have been centred around longer timescale processes, with Skipper *et al* demonstrating that in the solid phases IIa and IIb of $Li(NH_3)_4$ a stochastic, 3-fold rotational process occurs on the timescale of 2.0 ns and 7.3 ns respectively [146]. Interestingly, in the highest temperature phase (phase I, stable between 82 and 88 K) there is indication of diffusive motion in the quasielastic neutron scattering data, with a jump-length of approximately 2 Å. Phase I can therefore be designated a plastic phase of the molecular metal.

The aim of this section is to investigate whether the presence of three distinct phases in the 20 MPM solid (all of which occur at temperatures below 88.8K) give rise to differences in the momentum distributions of their protons. As such, this investigation does not strictly adhere to the principal of 'DINS as applied to heavy masses' theme of this chapter, but is included as an example of a standard application of DINS to the single particle dynamics of protons.

Initially, this study was planned to not only examine the proton environment

in each of the solid $Li(NH_3)_4$ phases, but also in the liquid phase and to compare with solid NH_3. Unfortunately, due to problems at the ISIS source during the experiment this was not possible, and only the solid phases of $Li(NH_3)_4$ were able to be measured.[7]

4.4.1 Sample Environment

As discussed in section 3.4, samples of $Li(NH_3)_4$ were prepared by the condensation of high purity NH_3 onto Li metal, within a clean, quartz container of flat geometry. The samples were frozen and sealed under vacuum, and were maintained at cryogenic temperatures at all times. Both the high purity of the sample, the inert quartz container and cryogenic sample temperatures ensured that no decomposition to $LiNH_2$ occurred, a thermodynamically favourable yet kinetically slow process. Runtimes for DINS measurements were of a minimum of 15 hours for each temperature measured, with total integrated proton currents of the order of 2700 μA h. A single sample of $Li(NH_3)_4$ was measured at temperatures of 22.8 K, 49.0 K, 74.3 K and 85.8 K.

4.4.2 Corrections to the Raw Data

Examination of proton dynamics is confined to forward scattering detector banks on VESUVIO, with no examination of heavier mass contribution to the scattering function being made for either forward or backscattering banks. The spread

[7]Initial measurements detailed here were performed March 2012. NH_3 measurements are rescheduled for May 2012.

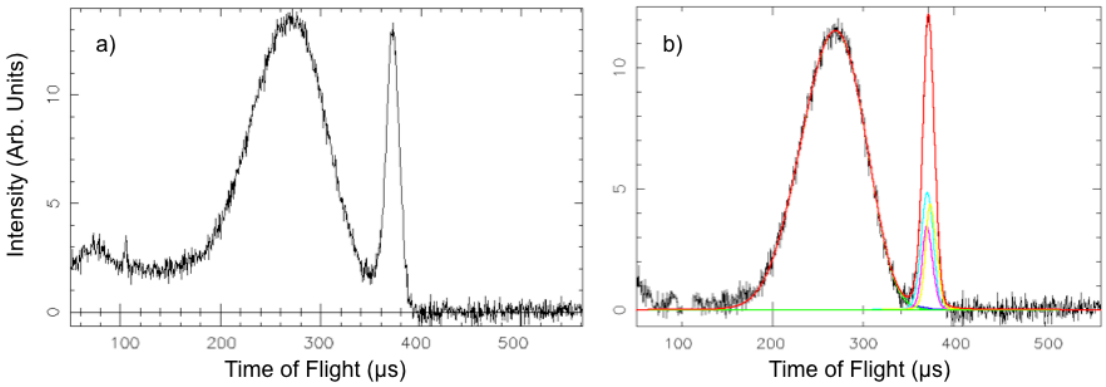

Figure 4.12: Forward scattering ToF spectra for solid phase I of $Li(NH_3)_4$. Data are for scattering angles 40-60° and depict (a) raw and (b) corrected data. Total fit to corrected data shown in red.

of light masses in $Li(NH_3)_4$ would make for an ideal multi-mass examination on VESUVIO, but the use of a quartz sample can rendered this impossible for this particular investigation, which instead focusses exclusively on the proton signal.

Figure 4.12a gives an example of the raw ToF data for $Li(NH_3)_4$, that of phase I at 82.5 K. It can be seen that due to the thickness of the sample, a significant amount of multiple-scattering can be seen in the spectra, shown by non-zero intensity below $150\mu s$. The sample was determined to scatter approximately 45% of the incident neutron beam. Within the framework of DINS, however, this multiple scattering is exhibited as a flat background beneath the proton signal in ToF, and is thus ostensibly simple to correct for. This has been performed for all temperatures independently, using the standard Monte-Carlo technique as implemented in VESUVIO data analysis [152, 154], with the only restriction being that the sample transmission was constant for each temperature.

The corrected ToF data are presented in figure 4.12b with example fits to the data demonstrated. Data have been corrected for both multiple-scattering and the sample independent gamma-background for VESUVIO [153], as discussed in both previous sections and the literature. Heavy mass gaussians are shown under the peak at higher ToF values, but at forward angles are not resolved and should not be assumed to have physical meaning.

4.4.3 Proton Momentum Distributions in $Li(NH_3)_4$

The neutron Compton profiles, $J(y)$, for the proton in $Li(NH_3)_4$ are presented in figure 4.13 for phases I, IIa, IIb and III, with the radial momentum distributions, $4\pi p^2 n(p)$, being presented in figure 4.14. It can be seen that in all cases the proton momentum distribution is indistinguishable, despite the differences in phase. This is something that is perhaps unexpected, particularly with the presence of slight translational diffusion as demonstrated in the QENS study in the literature. Whilst the timescales examined in DINS are orders of magnitude faster than those of stochastic processes (sub-femtosecond as opposed to nanosecond), a change in the zero-point motion of the proton may be expected to be seen for a translational contribution to the momentum distribution.

One thing that *is* clear from figures 4.13 and 4.14 is that the short-timescale proton dynamics are clearly dominated by an interaction that is independent of structural phase. At these temperatures the kinetic energy of the proton is deter-

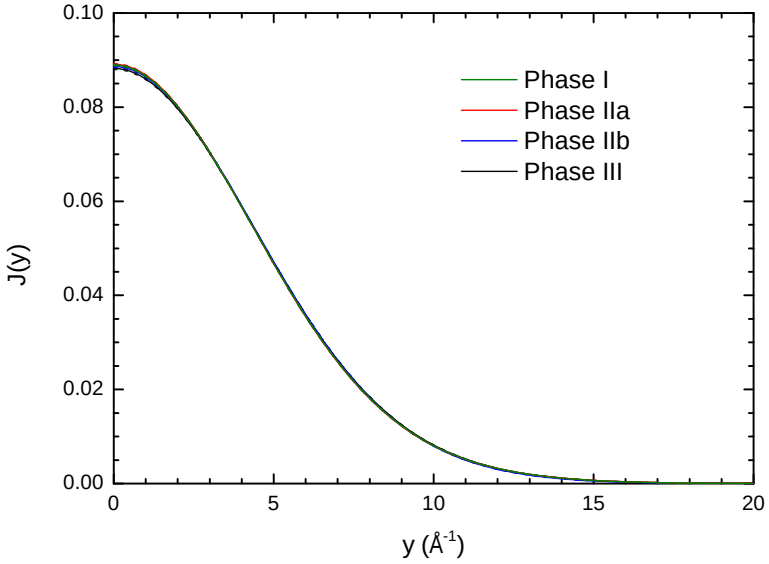

Figure 4.13: Neutron Compton profiles, $J(y)$, for $Li(NH_3)_4$ in each solid phase. Errors are shown as dashed line, but are too small to see.

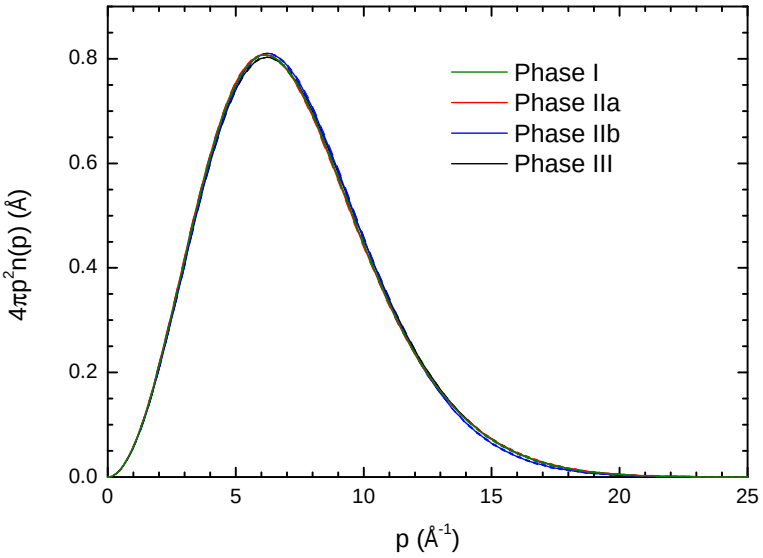

Figure 4.14: Radial momentum distributions for $Li(NH_3)_4$ in each solid phase.

Table 4.3: *Values of* ς_H, a_4 *and* $\langle$ *K.E.* $\rangle_H$ *for* $Li(NH_3)_4$ *solid phases*

Phase	ς_H (Å^{-1})	a_4	$\langle$ K.E. $\rangle_H$ (meV)
I	4.500 ± 0.015	0.139	126.978 ± 0.847
IIa	4.496 ± 0.013	0.093	126.752 ± 0.733
IIb	4.493 ± 0.016	0.152	126.583 ± 0.902
III	4.514 ± 0.016	0.125	127.770 ± 0.906

mined entirely by zero-point motion, and no discernible change in the momentum distribution is indicative of a single, overriding dynamical contribution. In order to determine in what way this contribution varies from that of the NH_3 molecule in the solid, a system of weak yet extensive hydrogen bonds, comparable DINS measurements are scheduled for the future.

A further point of interest in proton environment is in terms of harmonicity. The neutron Compton profiles are expanded in the form given in equation 4.14, whereby deviation from gaussian behaviour (arising from a single particle in a harmonic potential) is taken into account using the Gram-Charlier expansion of Hermite polynomials as detailed in equation (4.14). The total number and coefficients of these polynomials can be determined and subsequently fitted using a Bayesian approach, which in all cases for the $Li(NH_3)_4$ system included only the H_4 polynomial. This is commonly encountered in fitting of *J(y)* in DINS, and is a measure of the kurtosis of the momentum distribution, i.e. the degree to which the gaussian is 'peaked'. Values for ς_H and a_4 are given for each solid phase in table 4.3.

It is clear that not only do all phases contain effectively identical proton momentum distributions, but that these distributions deviate from gaussian behaviour to the same extent, with similar values for a_4. It is interesting to note that the Bayesian approach gave negligible contribution from a_2, which is demonstrated to be essential in modelling anharmonicity in H_2O liquid and ice. Taking the proton dynamics of NH_3 molecule to be dominated by the N-H bond, something that may be expected as in the case of H_2O [19], this difference in anharmonic contributions in $Li(NH_3)_4$ is itself interesting. A true comparison with NH_3 solid and liquid phases would be more enlightening in discussion of the single-particle dynamics of the proton, and determine further the extent of anharmonicity difference in solid $Li(NH_3)_4$. Increased electron density across the 'molecular surface', as indicated by molecular DFT and NMR studies of the system, may well be the determining factor of this anharmonicity [136, 141].

4.5 The Current State of DINS, VESUVIO and 'Further Work'

To specify further research that can grow from the results detailed in this chapter alone is not feasible. DINS is still an emerging neutron technique, a statement that may seem bizarre considering such measurements now span over two decades of research, but as such *all* DINS studies still reflect upon one another in a way that more established spectroscopic techniques do not. This is in part due to the DINS community being relatively small, but also due to controversies surrounding

the subject that will be briefly detailed here.[8]

VESUVIO is still the only operational spectrometer designed for DINS measurements, and as such there will always be some level of discontent amongst researchers (both in the field of high energy neutron scattering and the wider neutron community) as to the absolute validity and accuracy of such measurements. VESUVIO has undergone many changes in its physical setup and data analysis over the last decade, where factors such as non-Gaussian momentum distributions, multiple-scattering and questions pertaining to instrument resolution have come to light. The eventual construction of the ELVIS spectrometer at ORNL will be the greatest benefit (in this case used as a partial synonym for verification) to VESUVIO in terms of reproducibility of measurements for proton-containing and $^{3/4}$He systems [157]. There is also the ongoing issue of decreased proton cross-section as will be mentioned below.

The detection of high-energy neutrons is in itself an area of research tied to DINS, with the new YAP-based detectors on VESUVIO at forward scattering angles replacing the older ^{6}Li detectors.[158] The introduction of the double-difference technique in measurements has also led to improved resolution. There is certainly call for improving the detector banks at backscattering-angles, an interest in part bolstered by the work detailed in this chapter. Whilst we have shown that heavier

[8]Staunch opinion and conjecture are rarely allowed to enter ones thesis, and the opportunity should be grasped with both hands!

masses can be examined semi-quantitatively (SiGNaH) and indeed with impressive accuracy (^{7}LiF), the increasing separation of mass-specific peaks in ToF with angle calls for an increased anglular coverage above 150°. For simultaneous measurements of H and D it would also be beneficial to have lower angles (70-110°) monitored. There is also the issue of detector composition, with work currently underway to develop new detector types for high energy neutrons, such as improved diamond detectors instead of YAP.[159, 160]

The YAP detectors installed at forward scattering angles are essentially γ-detectors, with the background γ-radiation from secondary gold foils being removed as part of standard data analysis (*cf.* section 2.2.3). Whilst these detectors result in a far better instrument resolution, we encountered a rather significant problem when attempting to measure H_xWO_3. Our aim was to measure the proton and oxygen momentum distributions as they vary with x, but W gives rise to a nuclear resonance at the incident neutron energies of VESUVIO, giving rise to γ-release and resonance peaks in the forward scattering data, as shown in figure 4.15. The backscattering detectors, based on ^{6}Li are far less susceptible to this additional γ-radiation (though there is still some intensity witnessed), and thus a replacement of such with YAP-detectors would effectively limit the application of DINS to heavy-metal containing systems (most 3rd-row transition metals contain resonances in the measured ToF range for VESUVIO). These resonances occur at the same ToF values at all angles, and so in principal can be subtracted out from the measured spectra, but this has never been shown to work for reasons yet unknown.

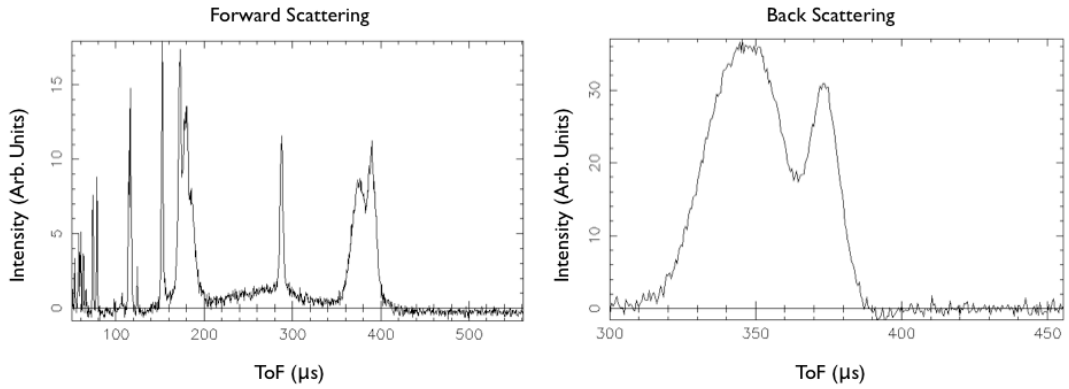

Figure 4.15: Raw ToF data for tetragonal H_xWO_3 (x∼0.3). W-resonances clearly seen in forward scattering, severely affecting the proton peak between 150-400 μs.

There is a conceptually new, model-independent analysis method being prepared by the group of Krzystyniak,[9] with principal applications in removing or isolating and analysing these resonances.

DINS has suffered from a lack of interplay with computational modelling, something that has been a particular problem to tackle due to the difficulty of computational calculation of momentum distributions for the proton. In the last couple of years, techniques such as ring-polymer molecular dynamics (RPMD) and Car-Parinello molecular dynamics (CPMD) have begun to model the quantum behaviour of this light nucleus,[161, 162] with the groups of Car and Parinello beginning to work alongside experimentalists to explore the interplay between measurement and theory. There are now also drives to further implement quasi-harmonic DFT calculations, as demonstrated within this thesis to characterise the

[9]From private correspondence

extent of anharmonicity in systems examined by DINS. Whether this will take the path of computation validating DINS measurements, or the latter being used to benchmark the former is still being discussed, but certainly there in a need for a closer collaboration between these two fields if the DINS technique is to grow further.

Our work on LiF demonstrated that there is substantial validity for DINS to be used to study heavier masses alongside theory, and we envisage one important progression from this. If a system is examined that contains protons in a particularly non-harmonic environment (such as the wealth of measurements on H_2O referenced in chapter 1) there is little reason not to simultaneously examine the momentum states of heavier masses in the system. Not only can this aid computation, but there is the intriguing possibility of examining whether the quantum effects in the proton are reflected in the momentum state of the heavier mass. The planned measurements on NH_3 mentioned in the preceding section are to be used to aid CPMD modelling of this system, where the librational characteristics are certainly expected to be anharmonic, and the extent of 'weak' hydrogen bonding can be investigated and further characterised. This would be a suitable step before finally developing an accurate computational model for the $Li(NH_3)_4$ system.

As a final note to this chapter, though it is always unfortunate to end on a point of contention, the furore over the possible existence, extent and cause of the 'anomalous cross-section' for the proton in DINS measurements must be noted. Details

as to the initial discovery,[44, 18] instrumental response [48, 47] and current theoretical handling [51, 49, 50] of the shortfall in proton signal on VESUVIO can be found in the literature. The importance of defining or explaining this effect became almost all-consuming for a few years in DINS, despite it being shown that its existence in no way affected the momentum width or neutron Compton profile measured. As such, the tag 'anomalous' came to be one of the most recognised associations with VESUVIO, and in the opinion of this author not something that aided expansion of the technique into a more accepted niche in neutron science. At this stage, the construction of ELVIS will verify the existence further, and most importantly *independantly* to VESUVIO (something of far greater importance than the reported finding of a similar effect in electron scattering experiments by Dreismann *et al*). Dreismann has also recently reported a decoherence effect in his measurements on liquid H_2 [163] that can not be reproduced by external analysis [164].

There are also the measurements of supercooled water by Andreani *et al* detailing a large moment in the momentum distribution corresponding to proton-delocalisation over two sites in the liquid [26], an effect that is visible in the raw data.[10] This property of supercooled water so far eludes computation,[11] despite RPMD models describing other dynamics in water very well, and unfortunately came at a time shortly after the 'anomalous cross-section' and reinforced the notion

[10]From private correspondence with R. Senesi, an author of the study
[11]Private correspondence with D. Manolopoulos

of VESUVIO as being an anomalous instrument. A reproduction of this particularly complicated and long experiment would be of great use in the verification of a moment in the proton momentum distribution of supercooled water. Unfortunately, this is not always possible due to the expense and time constraints of beamtime allocation.

With liberal use of opinion to conclude this section, there is great need for increased use of DINS *alongside* high level computation, and other neutron techniques such as IINS. DINS occupies a particularly powerful position in the study of proton dynamics, but as with all spectroscopic techniques there is great benefit from internal checks such as examination of heavier masses, and demonstrable agreement with calculation.

A constant leap towards the beauty of an 'anomalous' result can only continue for so long before pitchforks and flaming torches are seen amongst the detector arrays.

Chapter 5

The Dynamics of Coordinated NH_3 Within a Zeolite Host

Clap. Clap. Clap.

"Oh good. My slow-clap processor made it into this thing. So we have that..."

GlaDOS, Portal 2

This chapter details a number of neutron-based investigations into the dynamics of the ammonia molecule, NH_3, absorbed into and coordinated within a zeolite framework. In the strictest, chronological sense, this was the original problem set out to be tackled by this thesis, with experiments subsequently conducted alongside those high-energy neutron scattering developments detailed in the previous chapter. A number of interesting problems are encountered when examining neu-

tron data from coordinated, small molecules within a large framework, and the manner in which they exhibit themselves, their extent and the limitations thereof are the focus of most of the discussion found below. Initially the low-energy vibrational dynamics of NH_3 absorbed in zeolites NaA and CuA as examined by inelastic neutron scattering (INS) will be presented and discussed, followed by the longer-timescale processes probed by quasielastic neutron scattering (QENS).

Zeolites have long been of interest in spectroscopic fields, due to the necessity of separating or isolating signal from the large, host structure with that of an introduced species, or probe. This is often complicated in cases where the guest species is at low concentrations or containing light elements compared to the aluminosilicate framework. Spin-chemical techniques such as nuclear magnetic resonance (NMR) [165, 166] or electron spin/paramagnetic resonance (ESR/EPR) [167, 124, 126, 125, 168] can be applied in cases where the guest species can be isolated by virtue of its nuclear spin or paramagnetism. Certainly, the advent of complex pulse sequences in these techniques has led to the determination of structure and/or bonding between guest and host, but as with all techniques there are some inherent drawbacks or limitations.[1] In the case of techniques based on spin-resonance, the density of the spins of interest must be dilute in the system, which for zeolite investigations results in the necessity for the guest molecule being at the lowest possible concentrations. NMR techniques are limited to zeolites

[1] A seemingly difficult realisation when pursuing research in any spectroscopic discipline is that your technique cannot solve every problem thrown at it.

which do not contain open-shell extra-framework cations due to spin-spin relaxation (which are found commonly in catalytically active, d- and f-cationic zeolites) whereas EPR/ESR is limited to these cases alone. Then, of course, is the general necessity for the guest species to contain nuclei of non-zero spin themselves.

Conversely, neutron spectroscopy is, in general, a non-specific probe, compared to NMR/EPR. The adage is that 'neutrons see everything', which for the isolation of guest from host may seem problematic. For a guest species containing protons, however, this is overcome by its large incoherent scattering cross section, with the resultant incoherent spectra being weighted almost entirely by the proton signal. There is also the benefit of there being no limitation on concentration, host-guest electronic configuration or spin-states in a simple neutron spectroscopic measurement as there is with spin-resonance (unless of course the zeolite contains a nucleus with strong neutron absorption, which is rarely the case, and even this can invariably be overcome with longer counting times). This chapter is concerned with a system of both spin-0 and spin-active components, with the same techniques being applied to zeolite systems containing principal extra-framework cations of sodium and copper. Strictly a zeolite host is free of hydrogen, being an aluminosilicate framework, and this is virtually assured by the careful dehydration process described in section 3.1.1. Any inelastic or quasielastic neutron spectra will thus reflect the dynamic of the absorbed NH_3 molecules.

5.1 Ammonia Within Zeolite A

As briefly discussed in section 1.3, a majority of neutron spectroscopic studies of guest-zeolite systems have been concerned with either large molecules, or uncoordinated species that are simply confined by the porous network. The case of NH_3 is different to these studies in that coordination to extra-cations through the so called lone-pair on the nitrogen is possible. The dynamics of the molecule are therefore not necessarily isolatable, or decoupled from from that of the framework, as will be seen.

Studies of small molecules within a zeolite host are commonly conducted at high concentration, as has been previously stated in section 1.4, examining transport properties of what is essentially bulk behaviour. Relatively few studies have been conducted at *low* concentrations of these molecules, however; a case which may yield information on the initial coordination and dynamics of the molecule. This is important for the discussion of catalytic site occupation or modes of transport though the microporous system. There is also the interesting case of possible coordination sites exceeding the number of guest molecules, which raises the questions of preferential coordination or disorder throughout the system.

Few crystallographic studies exist for NH_3-loaded zeolites, and those that do are invariably conducted on large-pore frameworks such as MFI or FAU. For the first zeolite of interest in this thesis, zeolite NaA, only two studies exist, both conducted

by Seff *et al* [169, 170]. It was concluded that NH_3 can enter the zeolite up to a concentration of 32 molecules per unit-cell, existing in distinctly different environments. These coordinations are both to extra-framework cations, and secondary coordination to these bound NH_3 molecules through a hydrogen-network in the void-space of the zeolite. At the highest concentration, the β-cages of the zeolite are populated, but this has been shown to require both high-temperatures and pressures of NH_3 during the synthesis process [130]. One conclusion of Seff *et al* is that below a concentration of $8NH_3$ per unit cell, the distribution of NH_3 in the system is disordered and could not be refined by their methods.

For CuA there exist no crystallographic studies for NH_3 absorbed at low concenetrations, but along with EPR studies it has been suggested that at higher loadings the Cu-cation is removed from interation with the framework to form the tetrahedral $[Cu(NH_3)_4]^{2+}$ species within the α-cage of the zeolite [124, 126].

5.2 Sample Preparation and Environment

Following the methodology aid out in section 3.1.1 approximately 65 g of dehydrated zeolite NaA and CuA were prepared and dehydrated. Each sample was stored and handled under an inert, argon atmosphere, and at no point was exposed to an external atmosphere during sample loading or transport. For *in situ* measurements of NaA, approximately 5 g was loaded and sealed in a standard gas-loading, cylindrical aluminium can before being placed in the TOSCA instrument

for a background measurement at a temperature of 20 K. Doping with NH_3 was carried out *in situ* at a temperature of 298 K and equilibrated under 1 bar of NH_3 for 2 h. Excess ammonia was removed and the sample placed under low vacuum (10^{-1} mbar) before being cooled and re-measured. The CuA was ammoniated *ex situ* following the methodology outlined in section 3.1.2 for measurements on both TOSCA and MARI.

This chapter will follow a common nomenclature in zeolite science, in order to reflect the samples and NH_3 loadings. The unit cell of zeolite A was presented in figure 3.1 and shown to consist of a large central cage environment, termed the α-cage. Samples are referred to by their stoichiometric loading of NH_3 *per unit cell*, i.e. NaA·$x$$NH_3$ refers to a sample of the dehydrated Na form of zeolite A, into which an average of 4 molecules of NH_3 have been absorbed per α-cage.

5.3 Inelastic Neutron Spectroscopy: Low-Energy Vibrational Dynamics

5.3.1 INS of NaA and NaA·$(NH_3)_x$

Figure 5.1 shows the INS spectra collected on the TOSCA spectrometer for NaA·4NH_3. The spectra have undergone the standard treatments for TOSCA data, and the contributions for bare zeolite and can have been subtracted. It has thus been ensured that the measured spectra reflect the dynamics of the NH_3 molecules alone.

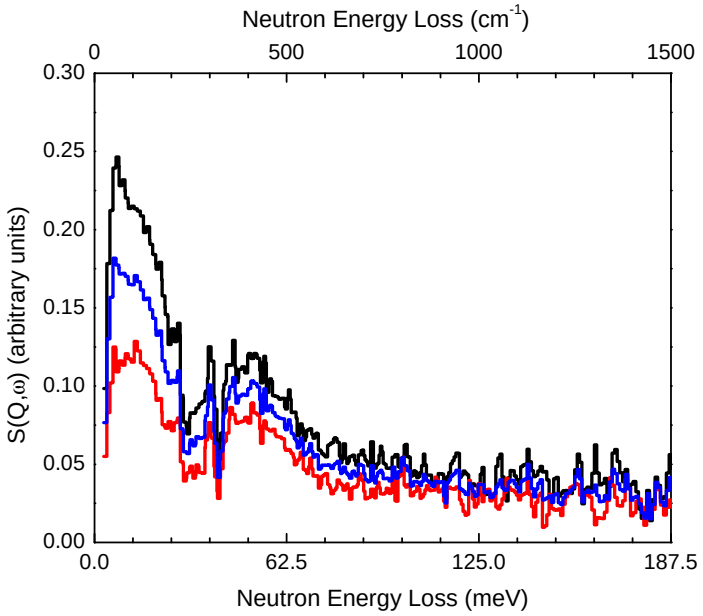

Figure 5.1: INS spectra for NaA·4NH_3, showing forward (red), back (black) and difference (blue) scattering.

The first conclusion from figure 5.1 is that the NH_3 molecules are coordinated to the zeolite in some manner, and do not exist as free species within the porous network. If this were the case, as it is to a certain extent with CH_4 [105] all that would be witnessed in the INS spectra would be a broad, gaussian peakshape extending over many hundreds of meV. This is a result of a freely recoiling molecular species under neutron impact [7, 171]. Whilst this may seem a simple thing to immediately observe, the existence of spectroscopic structure in figure 5.1 suggests that INS can be utilised in the studies of the dynamics of *coordinated* NH_3, and thus infer binding and structure at the low concentrations of these samples.

The resolution of TOSCA has already been stated in section 2.2.1 as being unparalleled for low-energy IINS, approximately 1.5% of the energy transfer, so the observation in figure 5.1 not of defined peaks, but of broadened collections of peaks is in itself interesting. These peak regions can be categorised as three features. The first is a supposition of peaks of decreasing intensity and appears in the INS spectra from 6-28 meV. A second broad peak region is witnessed from 43-66 meV and there is a sharp feature appearing between these broad regions at approximately 38 meV. Beyond these three features there is no additional structure witnessed at neutron energy losses in the INS spectra, and the signal can be classified merely as background/noise. The reason for a lack of defined peaks in the INS of this system will be presented shortly, but initially a methodology for the assignation of vibrational characteristics for each feature must be discussed.

Modern neutron spectroscopy is rarely encountered without some form of computational modelling used to verify or assign the physical data. This is especially true of INS measurements, where it is now standard to employ methods based on density functional theory (DFT) to model the system. As mentioned in chapter 1 of this thesis, unlike Raman or IR spectra, the relative intensities of peaks in an INS spectra can be readily modelled by *ab initio* techniques, being directly related to $\mathbf{u}(t)$ and thus atomic force constants. The reader is referred to some excellent references for the interplay between INS and DFT [7, 88, 172].

For zeolite systems there are a number of drawbacks to implementing DFT in

the calculation of either structure or phonon-states, primarily the simple fact that the systems are large. Even for the zeolite employed in this study, the small-pore zeolite NaA, there are 80 atoms in a given unit cell, with the lightest element being oxygen. Computationally this is particularly time consuming. Also, zeolites are known to have an ill-defined ground state energetically (*cf.* section 3.1), due to the inherent flexibility in the silyl (T-O-T) bridges [173, 53], and thus certain parameters in the calculations have to be relaxed to enable geometric and electronic convergence. This is particularly true for plane-wave (PW) techniques, considering a large volume of a zeolite unit-cell is void space [174]. However, modern computational packages have reached the level where, despite some strict approximations needing to be made, as described in section 5.3.3, fully periodic PW-DFT calculations are possible for such large systems.

Figure 5.2 shows some theoretical spectra for NaA.xNH_3 for x= 1, 3 and 4, modelled using the procedure discussed in section 5.3.3. In all cases the NH_3 molecule was seen to converge bound to the Na extra-framework cations of the system, with the molecule tilted to give a directional H-O orientation with the zeolite framework. The H-O distance was calculated as $\sim$1.8 Å, with the possibility of a hydrogen-bonding interaction being in agreement with previous NMR studies [165].

It can be seen from figure 5.2 that increasing the concentration of NH_3 from 1 to 3 or 4 molecules per unit cell results in three regions of peaks in the modelled INS

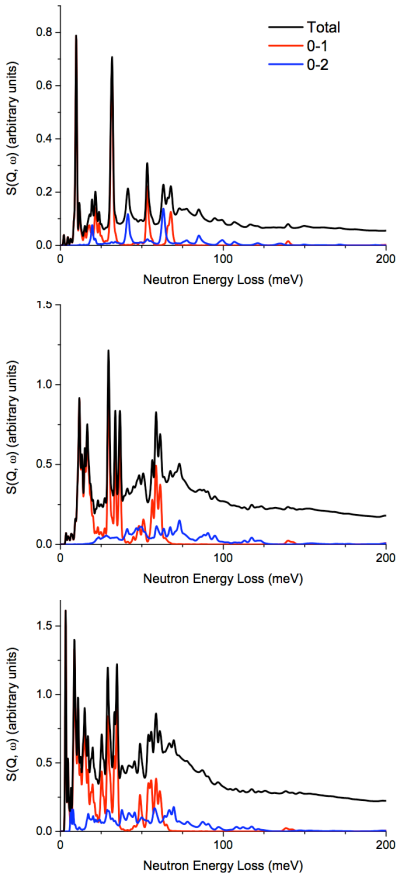

Figure 5.2: Model INS spectra for NaA·xNH$_3$ for x =1 (top), 3 (middle) and 4(bottom). Total (black), fundamental (red) and first overtone (blue) contributions are shown.

spectra. The lowest energy structures, up to 20 meV, correspond to translational motions of the NH_3 molecule perpendicular to the Na-N axis, and in the x=4 spectra this appears as a selection of peaks of decreasing intensity between 3-17 meV. The second broad peak seen in the x=4 case grows from a pair of peaks in the x=1 spectra (at 53 and 67 meV) and corresponds to a tilting motion of the NH_3 molecule with an invariant Na-N distance. The lower energy modes in this region correspond to a tilting that is tethered by the H-O interaction, with higher energy

tilting displacing the NH_3 protons from this preferential alignment.

Between these translational and tilting regions in the modelled INS spectra of NaA.·$x$$NH_3$ there are seen to be intense peaks which for the x=1 case is at 31 meV. These peaks are clearly distinguishable from the other peak regions, and correspond to a librational motion on the NH_3 molecule about its coordinating axis. A summary of these vibrational characteristics is shown schematically as part of figure 5.3. Also shown in figure 5.3 is a comparison between calculated and measured INS spectra for NaA·$4NH_3$.

It can be seen from figure 5.3 that despite the strict approximations inherent in the model calculations, there is good agreement with the experimental INS spectra. This is particularly true of the translational and tilting mode regions, where relative intensities and energies matched well the experimental spectra. However, the librational region, whilst occurring in the correct relative energy region of the spectra, is distinctly different in intensity. Also, whilst multiple peaks occur in the calculation, the measured INS exhibits but a single peak with greatest intensity at higher energy transfers. It remains to be theorised why such a distinct lack of intensity occurs in the experimental spectra, and why only the higher energy modes are witnessed.

The key to understanding such differences in the measured librational mode compared to calculation, considering the agreement of such with the translational and

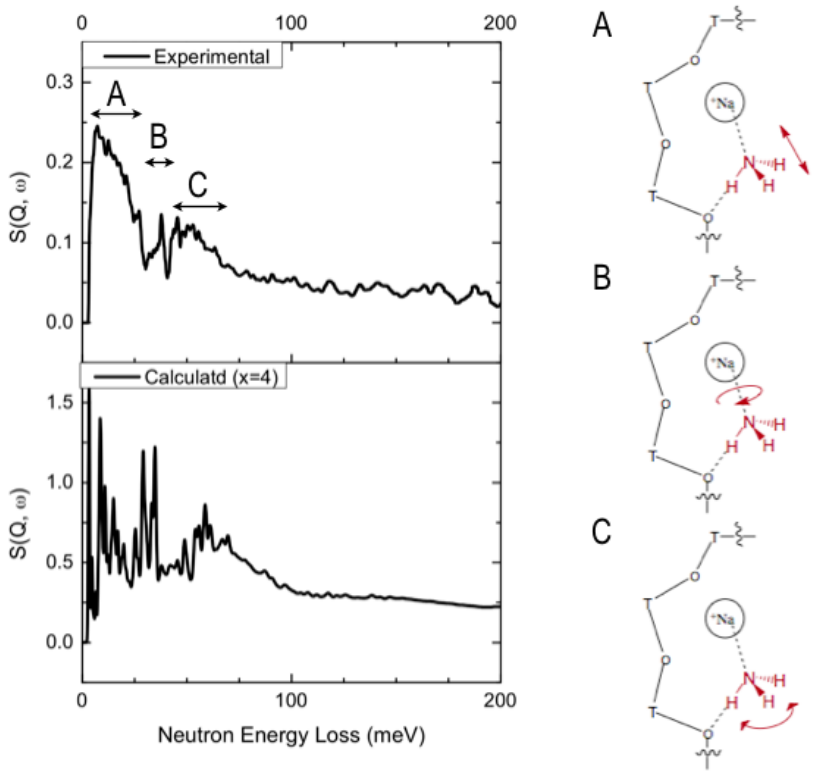

Figure 5.3: Left: Comparison between experimental and calculated INS spectra for NaA.xNH_3. Right: Schematic representation for the low-energy dynamics of coordinated NH_3 in zeolite NaA.

tilting modes, lies in the coordination of the NH_3 molecule and the effect of neutron impact. Recalling section 2.1.2 and equation (2.25), the exponential Debye-Waller factor was briefly introduced. The $2W$ term can be expressed, for a particular phonon mode, as

$$2W = \frac{\hbar}{2MN} \sum_s \frac{(\mathbf{q} \cdot \mathbf{u}_s)^2}{\omega_s} \coth(\frac{\hbar\omega_s\beta}{2}), \tag{5.1}$$

following the nomenclature of equation (2.25) with β defined as $\frac{1}{k_B T}$. The temperature dependance of the Debye-Waller factor through the coth term is the reason for INS measurement being confined to cryogenic temperatures (although some recent measurements on catalytic systems have been carried out at ambient temperature[2]). The effect of momentum transfer on atomic displacement vector, $\mathbf{u}_s$, is a great part of the reason for such librational discrepancies detailed above.

The effect of molecular recoil on INS spectra has been discussed in the literature, with the theoretical framework for such being detailed by Tomkinson [7, 171]. The transfer of momentum from neutron to target, if the target molecule is free to recoil about its lattice site, is a broadening of peakshape (with concordant loss in intensity) and shift to higher intensity, as the molecule is treated as a single particle of increased effective mass. This is true if the molecule is able to recoil freely, which is not the case for NH_3. The coordination along a single axis, with the molecule directed into the void space of the zeolite, enables a distinctly different response to momentum transfer if parallel or perpendicular to the coordinating axis. Greater recoil results in the latter, librational case, exhibited in the INS spectra as lower in intensity than other vibrational modes measured.

In addition to this, it must be noted that the method for calculating phonon-modes in the modelling process is done by a finite-displacement technique (section 5.3.3). This is not a particularly accurate way of describing librations, or modes

[2]Dr. S. F. Parker, private correspondence.

with larger atomic displacements, and will also effect the accuracy of calculated librational intensities. Due to the size of zeolite calculations, there is little way to compensate for this, but for the assignation of measured INS spectra this is not of great importance.

In order to demonstrate further the recoil of the NH_3 molecule, attempts were made to minimise the magnitude of momentum transfer, q, by conducting INS measurements across the same energy-transfer range on the direct geometry instrument, MARI. As discussed in section 2.2.1, fixing the incident neutron energy and allowing the detected, final energy to vary enables the sampling of **q**-space.

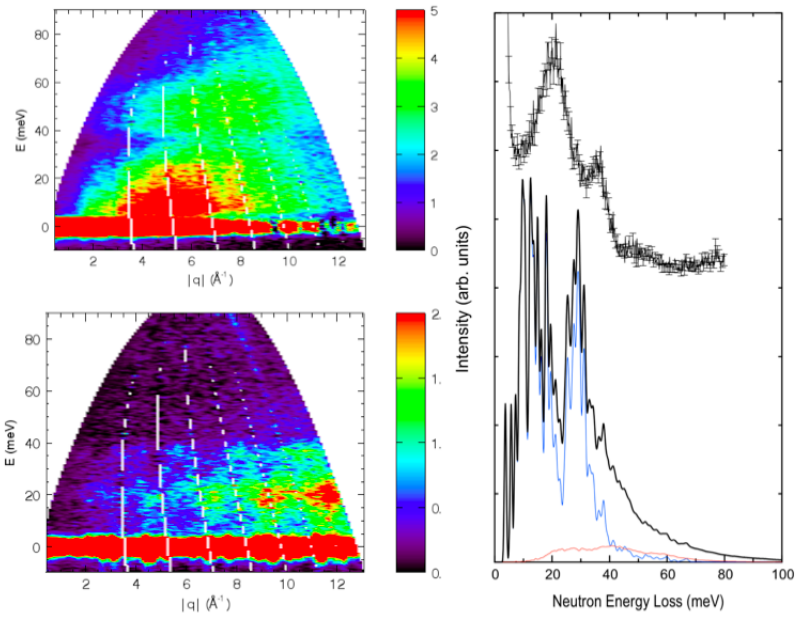

Figure 5.4: INS data collected on MARI with $E_i = 100\,\text{meV}$. Left: *above* NaA·4NH_3. *below* bare zeolite NaA. Right: Calculated INS for zeolite NaA compared to that measured on MARI ($4 < q < 10\,\text{Å}^{-1}$).

Figure 5.4 shows INS spectra collected on MARI for both NaA·4 NH_3 and bare zeolite NaA. For the same incident neutron energy of 100 meV, distinctly different behaviour is seen at a given q, with the vibrational modes in NaA·4 NH_3 seen to decrease at higher q values due to both the Debye-Waller factor and molecular recoil. It can also be seen that the low energy zeolite phonon modes, comprising framework flexing, occur across a large range of the NH_3 molecular dynamics, with riding modes therefore expected to further broaden the proton-weighted dynamics.

For the purpose of molecular spectroscopy (excluding materials exhibiting electronic excitations, for which MARI is ideally designed) MARI is used in conjunction with TOSCA, where there is the ability to maintain resolution at higher $\hbar\omega$, for example by going to lower q. TOSCA, as has been stated, is a variable q instrument with unparalleled resolution at low $\hbar\omega$. Due to the presence of molecular recoil in the NH_3 system, it was thought that by examining the lowest q values on MARI, even at the low energy phonon-modes, there would be an improved resolution. This proves not to be the case, as the magnitude of q is already low on TOSCA at these low energies. Thus the increased resolution of TOSCA outweighs the slightly lower q values available on MARI. Bar the simple demonstration of recoil, no additional information can be gleaned from the MARI data collected.

Included in figure 5.4 is a comparison between the measured INS on MARI, cut across a q-range of 4-10Å^{-1}, and that calculated by modelling of the NaA system. As can be seen there is good agreement between the measured and calculated

phonon energies.

As a final point of interest for the application of INS to this system, in addition to the stoichiometric loading NaA·4NH_3, a second *in situ* loading was performed on TOSCA to yield the NaA·8NH_3 system. Forward scattering data for both of these systems are shown in figure 5.5, and as can be seen, no additional structure is witnessed. The difference in scattering intensity is indicative of a purely recoil scattering, thus only the single coordination environment is witnessed in this system, that of a single NH_3 molecule bound to the extra-framework cationic species.

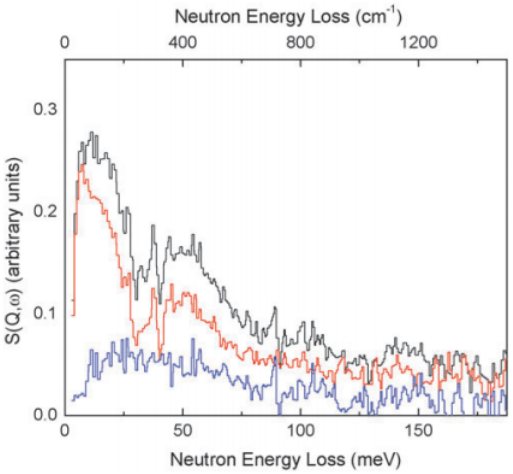

Figure 5.5: INS data collected on TOSCA for Na·4NH_3 (red), Na·8NH_3 (black) and the difference (blue)

5.3.2 INS of CuA and CuA·(NH_3)

The above results for the NaA.4NH_3 system demonstrated the ability for INS to examine the low-energy vibrational dynamics of NH_3 coordinated within a zeolite framework at low concentrations. Exchanging the extra-framework Na cations in NaA through the standard procedure outline in section 3.1.1 enables the synthesis of a predominantly Cu-containing system, denoted CuA. Chemically, such as system can be expected to interact with NH_3 entering the framework in a distinctly differently manner than to NaA, and the presence of unpaired electron states renders aforementioned NMR techniques unviable. INS is unaffected by such, and identical methodology as for NaA can be followed, in order to determine the dynamics and possible binding environments for the NH_3 molecule at low concentration.

Figure 5.6 shows INS spectra from TOSCA measurements for CuA·3NH_3. A simple comparison to the ammoniated NaA case, figure 5.1, demonstrates that whilst there is distinctly different structure in the CuA case, defined peaks have been broadened again into regions by a combination of recoil and riding-modes. At the lowest energies there is a collection of several peaks of increasing intensity up to a maximum at 20 meV. There appears to be a higher energy shoulder to this region, with lower intensity and centred at 27 meV. A number of low intensity peaks exist between 45-60 meV and then a final broad region that gives indication of two principal peaks at 80 and 90meV respectively. These higher energy modes

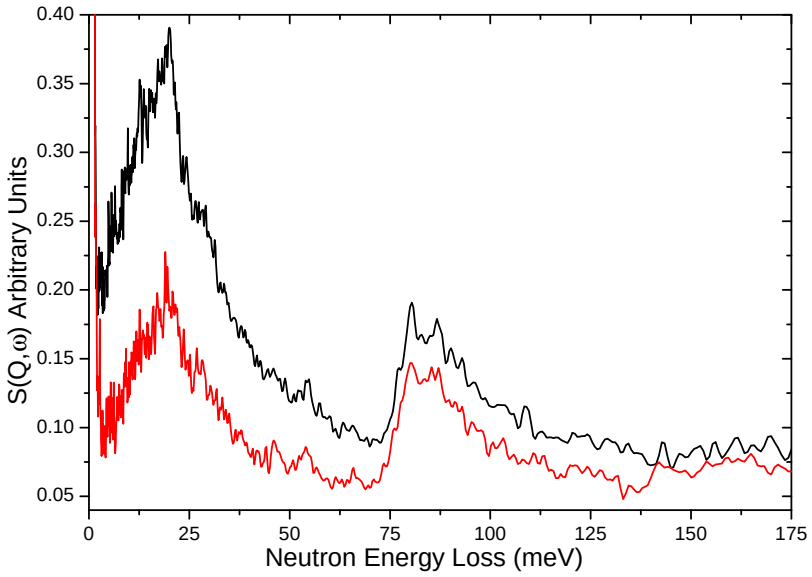

Figure 5.6: INS data collected onTOSCA for CuA·3NH_3 showing forward (black) and backscattering (red) data.

again suffer from a slight decrease in instrument resolution and recoil through the exponential Debye-Waller factor. No further structure was witnessed in the measured INS above these energies.

Whilst the application of INS to the CuA system is in principal no different than that of NaA, computationally this is not the case, as will be discussed in section 5.3.3. In order to understand coordination at the very low concentration of this study, a model system was created to reflect coordination of a single NH_3 molecule to a Cu cation, or dual coordination of 2 NH_3 molecules to the same Cu. Thus the simplest system of stoichiometry CuA·2NH_3 was modelled, as will be described in section 5.3.3, to determine whether the experimental CuA·3NH_3 spectrum was

composed of the single coordination environment, or a combination of the single and dual case.

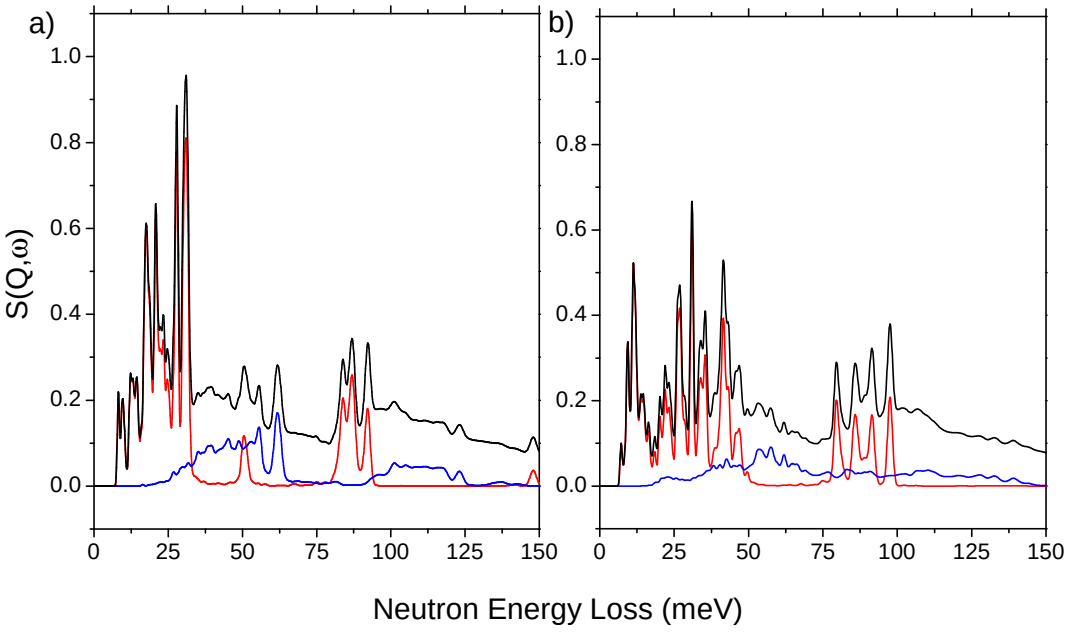

Figure 5.7: Modelled INS spectra for CuA.2 NH_3 with NH_3 bound to a) separate and b) a single Cu cation. Total (black), fundamental (red) and first overtone (blue) are shown.

The result of geometry optimisations on the model CuA.2 NH_3 system results in two converged structures, whereby the two NH_3 molecules are bound to the same Cu cation, or separately.[3] In the case of a single NH_3 molecule bound to an extra-framework Cu-cation, the geometry is distorted tetrahedral with reference to the

[3]It should again be stressed that definitive phonon calculations for these systems are not possible within the framework of DFT, but rather they can be incorporated to aid in the assignation of the experimental spectra.

Cu centre, with three O atoms of the zeolite 6-membered rings providing the remaining ligands. This has previously been suggested in a theoretical study for low concentrations of NH_3 within a zeolite host. For the case of dual binding to a single Cu, a four-coordinate planar arrangement resulted, with the framework enforcing a *cis*- arrangement for the two NH_3 and two framework O. Attempts to force a tetrahedral geometry relaxed to the planar arrangement in all cases. No system whereby three NH_3 molecules coordinated to the same Cu-cation were seen to converge to a ground state.

Figure 5.7 presents the modelled and annotated INS spectra for these CuA.2 NH_3 systems. For the case of coordination to separate cations, figure 5.7a, the modelled INS spectrum is seen to consist of a set of peaks of increasing intensity between 10-20 meV corresponding to translational movements of the NH_3 molecule about the Cu ion maintaing the Cu-N bondlength. The spread of peaks is due to coupling to framework motions whereby the Cu ion is displaced. The highest intensity peaks in figure 5.7a are the librational features of the two NH_3 molecules about their coordinating axis, occurring between 25-32 meV. These are followed by three low intensity peaks at 46, 55 and 65 meV. The first of these is a fundamental, and is the Cu-NH_3 stretching mode, whereas the latter two are overtones of the low energy vibrations. The final set of three peaks in figure 5.7a correspond to a rocking motion of the NH_3 molecule, whereby the protons displace parallel to the coordiniating axis.

The calculated INS spectrum for the case of two NH_3 coordinated to same extra-framework Cu cation is presented in figure 5.7b. The lowest energy region of the spectrum still conforms to translational displacements of the NH_3 molecules, but is distinctly different than that in figure 5.7a. Rather than a set of peaks with increasing intensity, there are distinct maxima at 12, 21 and 34 meV. These represent an out of plane bend of the NH_3 units, a translation of $Cu(NH_3)_2$ away from the framework and the in plane bend of the NH_3 units respectively. The strong rotational features in the INS spectrum occur at 26 and 31 meV. The Cu-N stretching region follows with an asymmetric mode at 43 meV and a symmetric stretch at 46 meV. The highest energy transfer region, corresponding to the rocking motion of the NH_3 units, occurs between 80-100 meV and consists of four distinct peaks of similar intensity.

As with the NaA case, direct comparison is made between the two geometries of NH_3 coordination in CuA and the experimental spectra in figure 5.8. It is clear that the case whereby coordination is to separate cationic centres matches the experimental INS much more closely than that to a single cation, as may be expected from the low concentration of NH_3 in the system. This is particularly good agreement for the translational, Cu-N stretching and rocking regions of NH_3 displacement. The energies of the librational region in figure 5.7a are concordant with the high-energy shoulder at 27 meV in the experimental spectra, and the stark intensity deficit is again in line with that same effect found in the NaA system. There is no evidence for the strong asymmetric and symmetric stretching modes

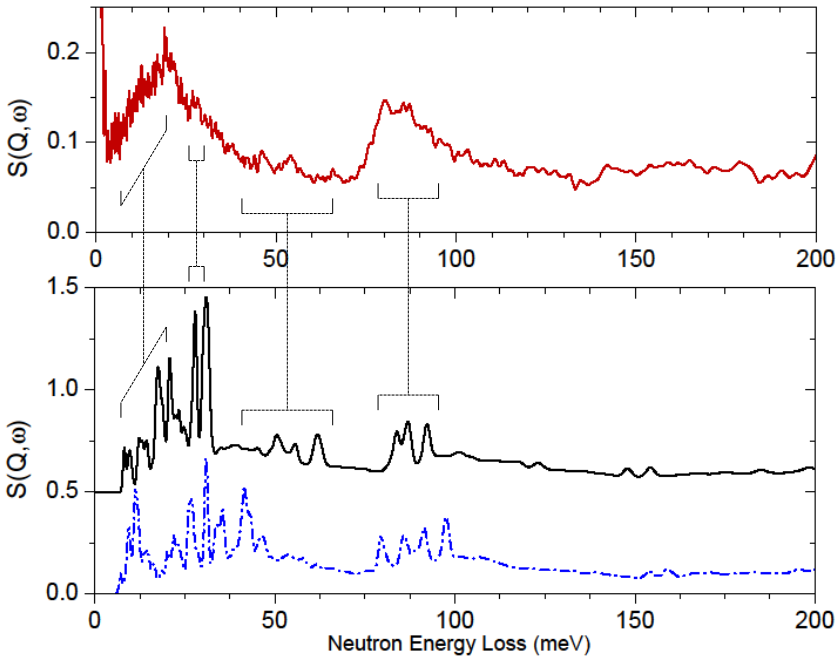

Figure 5.8: Comparison between experimental (red) and modelled INS spectra for the CuA·3NH_3 system. Modelled spectra are for 2 NH_3 coordinated to separate (black) and the same (blue) Cu cations.

of the -Cu$(NH_3)_2$ fragment at 43-46 meV, or of a fourfold splitting in the tilting region as was modelled in figure 5.7b. Coordination to a single Cu-cation is in agreement with a previous theoretical study, suggesting that at moderate concentrations of NH_3, the $CuO_3^{zeo}NH_3$ species is present [175].

Figure 5.9 again demonstrates the effect of q on the INS of NH_3 in the CuA system, as collected on MARI. As with the case of NaA no improvement in spectral resolution is gained over the TOSCA data. Comparison with figure 5.4 shows that the bare CuA and NaA spectra are essentially identical, expected from their

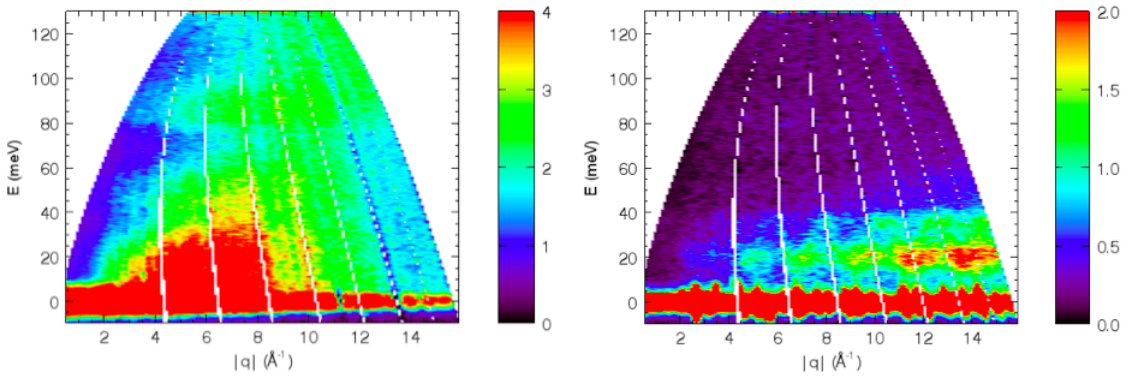

Figure 5.9: INS data collected on MARI with $E_i = 150\,\text{meV}$. Left: CuA·3NH_3. Right: bare zeolite CuA.

isostructural frameworks. This also exemplifies the likelihood of riding modes for the modes at translational and librational energies in the $\text{CuA} \cdot 3\,\text{NH}_3$ system.

5.3.3 Computational Detail

Modelling of all INS data was carried out using fully periodic PW-DFT as implemented in the CASTEP code [176]. As was explained in section 3.1, the adherence to the Löwenstein principle [114] for a Si:Al ratio of 1 in zeolite A results in a doubling of the framework unit cell parameter, which computationally leads to an unnecessary increase in complexity. To circumvent this, model unit cells were created with an increased Si:Al ratio of 2, whilst still adhering to the Löwenstein principle. Constructing a $Pm\bar{3}m$ framework for zeolite A, and distributing the Si and Al in tetrahedral sites accordingly, cationic species were introduced to the model zeolite to ensure charge-balance. The resulting model zeolite frameworks for this thesis were of stoichiometry $Na_8[Al_8Si_{16}O_{48}]$ (NaA) and $Na_4Cu_2[Al_8Si_{16}O_{48}]$

(CuA).

To attempt to expedite the optimisation of the framework in the NaA case, a pre-optimisation step was incorporated into the calculation. Each tetrahedral unit in the framework is matched to a template of 'ideal' geometry with the vertices of the real and template system joined by harmonic springs, and allowed to relax to minimise distortion from the ideal with no symmetry constraints. This geometric optimisation of the framework is implemented in the GASP code [177]. For any zeolite framework whereby the local geometry is influenced by the extra-framework cation, as is the case for Cu-containing zeolites, [116] such geometric pre-optimisation may be assumed to be redundant.[4]

Density functional geometry optimisations were carried out on the model systems under C1 symmetry, using the generalised gradient form of the exchange-correlation functional of Perdew, Burke and Ernzerhof (PBE) [178]. A plane wave cutoff of 500 eV was specified for all calculations, in accordance with the literature [174, 179], and all calculations were confined to the Γ-point. The unit cell parameters were fixed during the optimisation process (necessary for calculations of this size in systems predominantly void-space and with ill-defined ground states) as $a = b = c = 11.9$Å(NaA), 12.138Å(CuA) and $\alpha = \beta = \gamma = 90°$.

[4]Whether this geometric approach does in fact expedite DFT calculations is yet to be determined. It would be interesting to see whether this is more likely for codes utilising Slater-type orbitals rather than PW basis sets.

Once the framework was optimised sufficiently, NH_3 molecules were introduced in the proximity of extra-framework cations and the system as a whole allowed to subsequently re-optimise freely.

Phonon calculations were computed using the same plane wave cutoff as for geometry calculations in CASTEP, using the finite-displacement method, numerically calculating the second derivatives of the energy with respect to atom coordinates about their equilibrium position. From the density functional calculations (*cf* Appendix B) the atomic displacement vector, $\mathbf{u}_j$, can be computed for each transition, ω. These calculated results can be then transformed into model INS spectra using the aCLIMAX code designed specifically for this purpose [180], whereby $S(\mathbf{q},\omega)$ is given by

$$S(\mathbf{q},\omega) = \sum_j \sigma_j \left\langle \frac{(\mathbf{q}\cdot\mathbf{u}_j)^{2n}}{n!} \exp(-\mathbf{q}\cdot\mathbf{u}_j)^2) \right\rangle_{PowderAverage}. \tag{5.2}$$

The computed powder averaging of $S(\mathbf{q},\omega)$ is discussed in detail in reference [7]. In the above expression $\mathbf{q}$ is the neutron momentum transfer (in Å^{-1}), σ_j is the incoherent neutron scattering cross-section for atom j and n is the order of the transition such that $n = 1$ is the fundamental, $n = 2$ the first overtone etc.

5.3.4 Conclusions from INS

The above subsection has demonstrated the application of incoherent inelastic neutron spectroscopy to the case of NH_3 absorbed at low concentrations within a

zeolite framework. Studies have been shown for zeolite NaA and CuA.

Initially it was shown that, through the large incoherent scattering cross-section of hydrogen, only the dynamics of the NH_3 molecule itself are witnessed in the INS spectra, allowing for isolation of the guest species dynamics to those of the framework. Additionally, it was demonstrated that under neutron impact, the NH_3 molecule does not recoil freely as in the case of other small molecules at low concentration (such as CH_4) and thus the dynamics measured by INS are related to the binding of the NH_3 molecule to the zeolite.

Through modelling of the systems at the level of fully-periodic density functional theory, the dynamics of model systems can be calculated, and the regions of intensity in the experimental INS assigned for each. It has been shown that in the case of $NaA \cdot 4\,NH_3$ the experimental INS can be described as three regions of increasing energy, relating to translational, librational and tilting motions of the NH_3 molecule in relation to its coordinating Na-N axis.

For $CuA \cdot 3\,NH_3$ the INS spectra have been shown to agree with the case of single NH_3 molecules binding to Cu cations in the system, compared to dual binding to a single Cu. This preferential orientation is demonstrated by the energies of the Cu-NH_3 stretching and librational regions, and the shape of the translational and tilting features in the experimental INS.

For both the NaA and CuA systems it has been demonstrated that there is a consistent lack in intensity in the measured librational feature, compared to calculation, despite the energy of this feature and the relative intensities of other dynamical modes matching the calculation. Two effects have been suggested for this loss in intensity. Firstly, it has been noted that the method used for calculating atomic displacements and forces is not ideal for librational motions, although necessitated by the systems being large. Secondly, the differing effect of molecular recoil on different vibrational modes of of the NH_3 coordinated along a single axis has been discussed.

5.4 Quasielastic Neutron Spectroscopy: Longer Timescale, Stochastic Processes

5.4.1 QENS of NaA and NaA·3(NH_3)

Variable temperature QENS measurements were conducted on samples of NaA.3NH_3 in order to determine the presence and nature of longer timescale dynamics, i.e. the non-vibrational motions of the NH_3 molecules within the α-cage environments of the zeolite host.

Figure 5.10 demonstrates the existence of quasielastic intensity (intensity outside of the elastic line) in the QENS measurements from pyrolitic graphite (pg002) detectors on IRIS for NaA·3NH_3. Data have been presented on a log scale, with

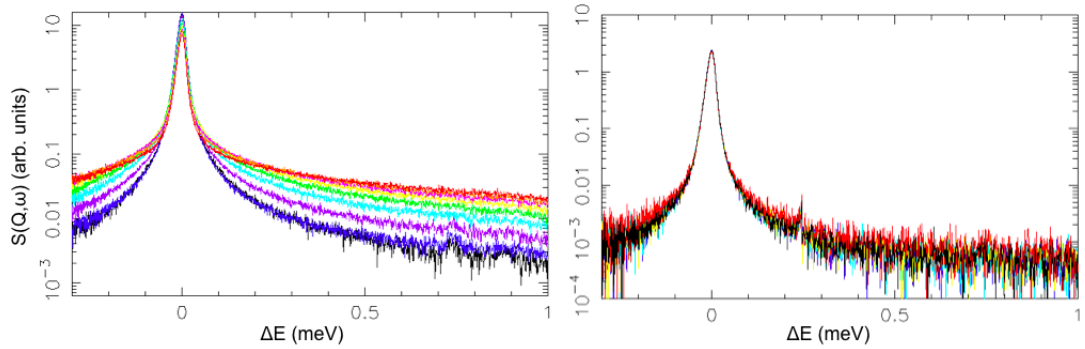

Figure 5.10: Total scattering across the quasielastic range for *left*: NaA.3NH_3 and *right*: NaA at temperatures of 4 K (black), 30 K (blue), 60 K (purple), 90 K (cyan), 120 K (green), 150 K (yellow), 180 K (magenta), 210 K (orange) and 250 K (red). *Note differing y-axis scales.*

all Q values summed for each temperature, at energy transfers far less than those measured in INS. Even a simple examination of this raw data is able to discern two important properties of the NaA.3NH_3 system; firstly is that even at 60 K there is quasielastic intensity and thus dynamical processes occurring at longer timescales than vibrational motion, and secondly that there is an absence of any inelastic features up to 1 meV.[5] Since rotational tunnel-splitting peaks occur in this region [10], their absence can rule-out the NH_3 molecules behaving as free-rotors within NaA.

In contrast, the raw QENS data for NaA exhibits no quasielastic broadening. Intensities are far lower than for the ammoniated case, due to the lack of protons in the system, and are so low that that the second pulse artefact can be discerned at ∼0.23 meV.

[5]Quick measurements were also made with pg002_offset chopper phasings on IRIS to check up to 1.5 meV. No inelastic features were witnessed

The greatest barrier in QENS measurements of zeolite materials, or indeed any large framework, is the presence of elastic intensity in the low Q ranges measured. In order to partly compensate for this, a separate QENS experiment was run on empty zeolite, and efforts made to subtract this signal, along with sample environment, from the measured, ammoniated case. However, some structure was still witnessed across some Q values in the range examined, and these have been omitted from the analysis.

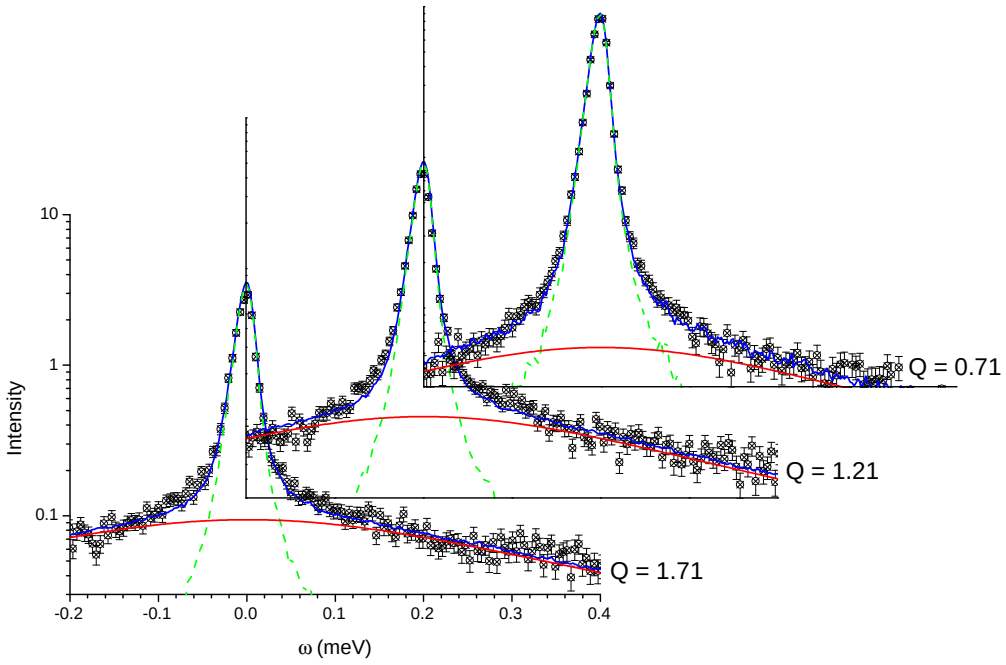

Figure 5.11: Example fits for $NaA \cdot 3\,NH_3$ at 250 K for three values of Q, detailing experimental data (black), elastic component (green), quasielastic component (red) and total fits (blue). Intensities are on a log scale.

Figure 5.11 displays some fits to the measured QENS data for $NaA \cdot 3\,NH_3$ at 250 K

and three measured Q values. Analysis of all QENS data was carried out using the Modes package [181], and a Bayesian approach has been adopted for fitting of the quasielastic contributions of the spectra. During the fitting procedures at all values of Q, the data fit well to a resolution broadened elastic δ-function and single quasielastic Lorentzian. This was checked by a separate, non-Bayesian approach using the DAVE software [182], and again no consistent fits resulted from using two quasielastic components. Thus on the timescale of these measurements, only a single quasielastic process is seen to occur. This infers a decoupling of translational and rotational motion in agreement with equation (2.28). The widths of the Lorentzian lines are seen to exhibit no pronounced Q^2 dependance, figure 5.12, which is indicative of a localised, rotational motion. For translational motions the Lorentzian widths would be seen to quickly increase with Q^2.

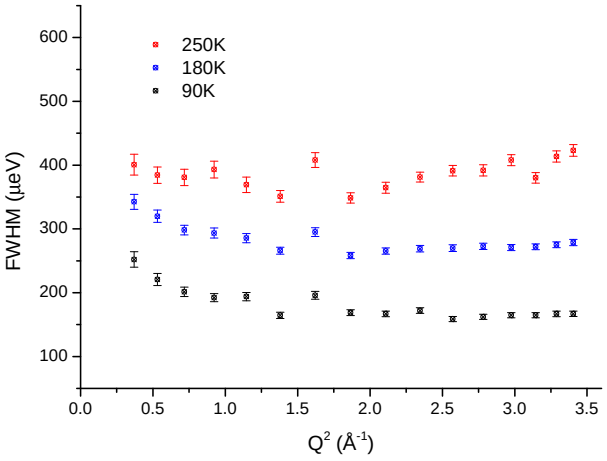

Figure 5.12: FWHM (Γ) for three temperatures of $NaA \cdot 3\,NH_3$ as varying with Q^2.

The nature and timescale of this rotational process can be demonstrated by an examination of the elastic incoherent structure factor (EISF) introduced in equations (2.26) and (2.27). Defining the scattering law for rotational motions as [66]

$$S_{rot}(Q,\omega) = \left(A_0(Q)\delta(\omega) + \sum_i A_i(Q)L(\Gamma_i,\omega) \right) \otimes R(Q,\omega), \tag{5.3}$$

which for a single rotational motion can be set as $i = 1$. In equation (4.2), $L(\Gamma_i,\omega)$ are the Lorentzian functions for the quasielastic signal with Γ_i defining the half-width at half-maximum (HWHM), $A_0(Q)$ and $A_i(Q)$ are the elastic and quasielastic incoherent structure factors respectively, and $R(Q,\omega)$ is the resolution function.

It is the EISF, $A_0(Q)$, that is of principal interest, as its dependance upon Q can give an indication of the nature and timescales of the rotational process. The EISF is a measurable quantity, defined as

$$A_0(Q) = \frac{I_{el}(Q)}{I_{el}(Q) + I_{qe}(Q)}, \tag{5.4}$$

where $I_{el}(Q)$ and $I_{qe}(Q)$ are the integrated intensities of the elastic and quasielastic signal, respectively. Modelling the NH_3 units as 3-fold rotors, whereby each molecule processes about its coordinating axis by 120° jump-rotations, $A_0(Q)$ can be specified as [66]

$$A_0^3(Q) = \frac{1}{3}\left[1 + 2j_0(Qr\sqrt{3})\right], \tag{5.5}$$

where j_0 is a 0^{th} order spherical Bessel function, and r is the hopping distance. A plot of the measured EISF is shown in figure 5.13 for three temperatures, alongside a model of the 3-fold jump model in equation (5.4).

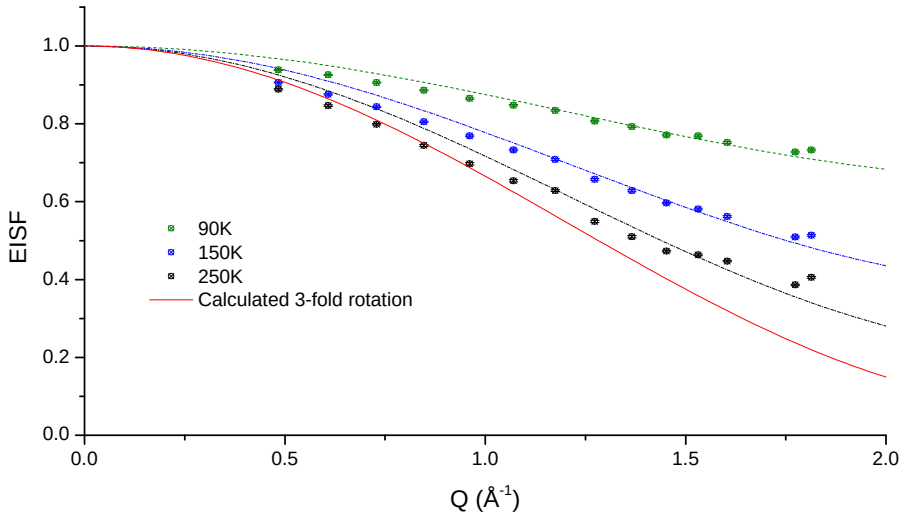

Figure 5.13: Measured EISFs for $NaA \cdot 3\,NH_3$ for three temperatures. A model 3-fold rotation with $r = 0.88\,$Åin equation (5.4) is shown. Dashed lines are fits for each temperature according to equation (5.6).

In figure 5.13 the dashed lines indicate a fit to a model system whereby only a percentage, p, of the NH_3 units are undergoing rotational precesses. For the same value of $r = 0.88\mathring{A}$ in this case, equation (5.5) becomes [183]

$$A_0^3(Q) = 1 - p + \frac{p}{3}\left[1 + 2j_0(Qr\sqrt{3})\right]. \tag{5.6}$$

Values for p are determined as approximately 85%, 66% and 37% at 250 K, 150 K and 90 K respectively. Whilst fits of this type may seem to be appropriate, the validity of such, and deviations from 3-fold behaviour will be discussed in section 5.5 towards the end of this chapter.

The Lorentzian widths across different temperatures can be used to calculate an activation energy and residence time for the measured localised process, using the relations

$$\Gamma = \Gamma_0 \exp\left(\frac{-E_a}{k_B T}\right), \tag{5.7}$$

and

$$\Gamma = \frac{3}{2}\hbar\tau^{-1}. \tag{5.8}$$

Equation (5.7) is an Arrhenius relation between Lorentzian width and activation energy, E_a, and τ in equation (5.8) being the mean residence time between instantaneous jumps in the rotational motion. The Arrhenius fit to experimental Lorentzian widths is presented in figure 5.14. As can be seen the data is fitted well by a linear expression for temperatures >150 K with a resultant activation energy for the process being calculated as 20.034 meV. At 250 K the measured residence time for the protons is 2.527 ps.

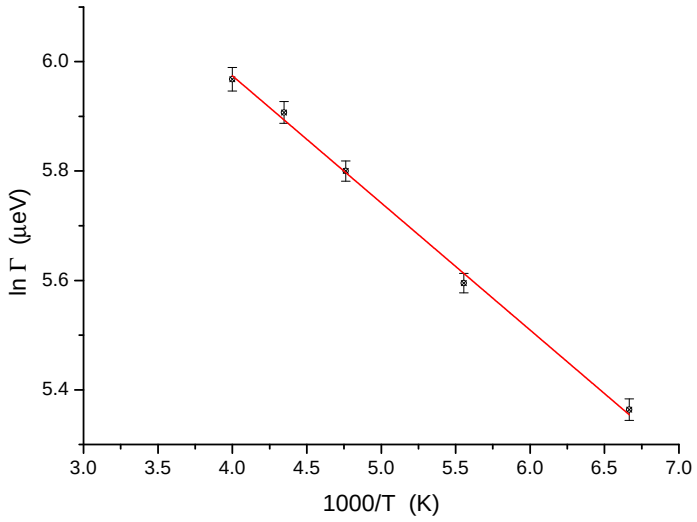

Figure 5.14: Plot of lnΓ against temperature for NaA $\cdot$ 3 NH_3 (black) with linear fit (red)

5.4.2 Conclusions from QENS

From this section it has been shown that QENS investigations using the IRIS spectrometer are able to examine longer timescale dynamics of coordinated NH_3 within zeolites NaA and CuA. From an initial statement that quasielastic broadening of the elastic line is apparent for the ammoniated zeolites, a Bayesian approach has been taken to fitting the quasielastic signal, which for NaA·3NH_3 yielded good fits incorporating only one quasielastic component. Examination of the measured EISF for this system showed that the single dynamical process was localised, i.e. essentially rotational in nature, and comparison was made to that of an ideal, 3-fold rotor. An Arrhenius plot of quasielastic width against temperature proved to be a suitable model at temperatures above 150 K, with a resultant activation

energy for the rotational process being calculated as 20.034 meV.

5.5 Discussion of the Dynamics of Coordinated NH_3 Within a Zeolite

The aluminosilicate framework of zeolite A has an effect on the dynamics of coordinated NH_3 molecules, despite these molecules being essentially bound to the extra-framework cation; a statement that should be taken as the overarching conclusion of all the detailed zeolite investigations in this chapter. In INS measurements this is immediately apparent from the spread of low-energy vibrational motions of the NH_3 molecules, with translational and librational modes in particular overlaping with framework-phonon modes of the zeolite. In QENS measurements it is clear from the measured EISFs of figure 5.13 that whilst the stochastic processes are localised, a fit to a 3-fold rotation (or indeed 6-fold or infinite jumps) around the NH_3 coordinating axis is not a sufficient model.

Examining figure 5.13 in a bit more detail, an insight to these deviations may perhaps be made. Let it be assumed for a moment that a fit with some percentage of NH_3 molecules being stationary, essential for agreement with the 3-fold model at higher Q, is incorrect. The observation that measured EISFs at 210 K, 230 K and 250 K seem to converge to the latter also suggests that this model in incomplete. The measured EISF is in agreement with the 3-fold model at low-Q, with stark differences at high-Q, although it should be noted that some discrepancy at high

Q is not unusual for zeolite studies.

The modelled EISF is strictly for rotation about a fixed axis, but from the INS measurements it is seen that there are very low energy modes for molecular motion perpendicular to this axis. At longer timescales each residence point for the NH_3 protons will not be specified by points on a circular path, but rather take a distribution about their energetic minima. Whilst model EISFs have been calculated for rotational motion about mobile axes (whereby the axis is itself undergoing stochastic rotational or diffusive motion) none exist that describe this particular situation, to the author's knowledge.

The next point of interest concerning molecular rotation of the NH_3 molecules in zeolite NaA is that the activation energy calculated from the QENS measurements, 20.034 meV, is lower than the energy of the librational band in both the INS measurements and modelled phonon spectra, 37 meV. The Arrhenius plot in figure 5.14 is for temperatures between 150-250 K, whereas the INS measurements are taken at 20 K, necessitated by the Debye-Waller factor. There are no quasielastic components to the elastic line at this temperature. At temperatures above 100 K the low energy framework phonons and NH_3 displacements will be populated, and it could be suggested that an alternative mechanism to purely rotational motion comes into play, whereby rotation is phonon-mediated or thermally activated. It must be restated that there is no indication of rotational tunnelling processes in the QENS spectra.

5.6 Further Work, Some Initial Findings and Comments on Solid Ammonia

Ostensibly, the utilisation of neutron spectroscopies in the study of hydrogen-containing, small molecules within a zeolite host is both simple and highly advantageous. These are techniques whereby the guest species is immediately distinguishable from the host, with resulting spectra being weighted by the former to such a degree as to be totally specific. The above studies have demonstrated, however, that for coordinated molecules, the low energy dynamics are affected by the host, with complications from such arising in both INS and QENS.

There is scope for continuation of these types of zeolite investigations, despite these complications, and in particular it would be interesting to develop *in situ* methodology for achieving extremely low concentrations of guest species (currently limited by too large a required sample size for the IGAn equipment [6]), and to take advantage of selective deuteration for larger molecules. The rotational dynamics of CH_3ND_2, for example, would be particularly interesting, with QENS being able to examine whether the methyl group acts as a free rotor within the framework despite molecular coordination to the host through the deuterated nitrogen. Conversely, the vibrational modes of CD_3NH_2 protons could be isolated.

[6]The IGAn is an as yet unpublished intelligent gravimetric analysis device, able to be used for *in situ* neutron experiments (currently exclusively crystallographic).

The efforts to achieve very low Q values at higher $\hbar\omega$, particularly around the librational region of the INS spectra, using MARI were demonstrated to suffer from decreased resolution compared to TOSCA. However, the spectrometer BRISP (designed as a quasielastic spectrometer with a large Q-range [184]) based at the ILL would possibly be able to achieve this kinematic regime with sufficient resolution to truly examine the effect of momentum transfer on the librational characteristics of NH_3 within a zeolite host.

A variable temperature QENS investigation of $CuA \cdot 3\,NH_3$ was attempted as part of this work, with the aim of determining whether diffusive processes occur in addition to localised dynamics, their respective natures and timescales. Unfortunately, the resultant data are currently not understood, with a repeat of experiment at extremely low loadings of NH_3 being required. Certainly, at higher loading the $Cu(NH_3)_4$ unit is expected to diffuse freely through the system, but for a host-coordinated $Cu(NH_3)$ species, as one would expect from our loading of $\sim$3 NH_3/unit cell the framework would play a similar role as in the NaA case detailed. Again, we witnessed a single quasielastic Lorentzian with Q-independant widths, suggesting a single, purely localised dynamic, but the EISF determined did not seem to fit any model known, and thus the work is not detailed here.

Promising work is currently underway to examine NH_3 itself in more detail in the solid phase. Initial INS measurements were taken to compare with NH_3 in alternative systems, including the above studies within a zeolite host. This can serve

as a simple check that NH_3 has not crystallised around or on the surface of the host, which it was indeed seen to have not. Simple density functional calculations on a supercell of NH_3 were seen to model the translational, low-energy phonon modes very well, as seen in figure 5.15. The librational contribution to the INS spectra are far removed from that calculated, and the calculated peak is seen to shift depending on the magnitude of atomic displacement in the phonon-calculation. This is indicative of particular anharmonicity in the librational dynamics of the solid, which are being further investigated by path-integral calculations and DINS studies.

We have also begun to examine whether any stochastic processes are evident in variable temperature QENS, as was initially mentioned by Skipper *et al* as part of their Li-NH_3 solution studies.[146] We can confirm the existence of quasielastic intensity above 150 K, but with particularly narrow Lorentzian widths, close to the resolution of the IRIS spectrometer mica006 phasing. Repeat measurements using the mica004 phasing also demonstrates this intensity, with further measurements using the IN13 instrument based at the ILL reactor source are planned. It is clear that the weakly hydrogen-bonded network in the solid gives rise to interesting dynamical processes, which are being further explored.

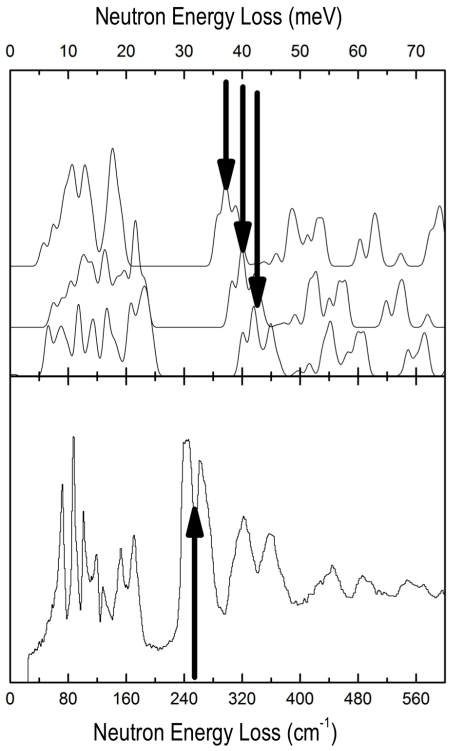

Figure 5.15: Initial INS measurements on solid NH_3 (bottom) and calculated spectra (top) demonstrating principal librational feature in each case. Calculated spectra are for displacements of decreasing amplitude (highest to lowest)

Chapter 6

Summary and Conclusions

"I run to the wind, I run to the river, there's blood on me. It's your memory... It's the smile of insanity."

Toyah, *Angel & Me*

This thesis is composed in the manner of individual neutron-based experiments, divided into two groups. Firstly, investigations detailing the application of DINS to systems of mixed masses are detailed, with the aim of exploring the limitations and applications of this technique into more applied, chemical directions. Lower energy neutron experiments on a single system are then detailed, that of NH_3 absorbed at low concentrations into zeolite A. This (relatively brief) chapter aims to summarise results of each of these two pursuits, discussing both the achievements and wider import of each in their respective fields.

6.1 DINS of Mixed Masses

The results detailed in chapter 4 are perhaps the most significant of this thesis, and certainly those that have currently seen most discussion and excitement when presented to the community of neutron spectroscopy. As was detailed in section 4.6, DINS is still an emerging technique, and the application of such to mixed and heavy masses is a new departure for the field.

Initially, results were presented for the system of NaH nanoparticulates within a silica gel matrix, SiGNaH. As part of this study both bulk NaH and amorphous Na within silica gel, SiGNa, were also investigated. This study was the initial catalyst from which the study of mixed masses on VESUVIO has sprung, and is the first study of the technique to look at multiple masses $>$ 4amu by DINS. Initially, the analytical technique of 'stoichiometric fixing' is detailed, with the validity of such as it arises within the impulse approximation being discussed. The proton signal for bulk NaH and SiGNaH was analysed using the forward scattering detector banks on VESUVIO, with the neutron Compton profile and radial momentum distribution function showing slight discrepancies, with a shift to higher momentum states in the nanoparticulate, encapsulated system.

The profile widths for heavier masses (O, Na and Si) for NaH, SiGNa and SiGNaH were determined by applying the stoichiometric fixing method for backscattering

spectra, with a clear distinction resulting between Na in the ionic state and amorphous metal. The value for SiGNaH was seen to lay almost exactly between these two, which is expected for the system composed of a 1:1 distribution of Na^0 and Na^+. The profile widths for Si were unchanged in the gel samples, reflecting their constant environment, and that of O exhibited only a slight decrease in the SiGNa system with respect to SiGNaH. This is consistent with increased O-encapsulate interaction. There results were compared with previous studies on Na metal (DINS) and NaH (INS) and were seen to agree well with these findings, lending credence to the stoichiometric fixing method for heavy mass analysis in DINS.

The second study detailed in chapter 4 is that of ^{7}LiF. This investigation was designed to test the absolute accuracy of DINS measurements of heavier masses, and particularly for weak scatterers that are unable to be examined by alternative neutron techniques. Measurements of both ^{7}Li and ^{19}F profile widths were extracted simultaneously from the VESUVIO backscattering data, for five temperatures between 4-300 K. This was again achieved by fixing the relative Li:F:Al stoichiometries, and have been compared to quasiharmonic density functional calculations of the system. In all cases the measured profile widths were seen to lay withing $\sim$5% of calculated values, which is astonishingly promising for the future application of DINS, particularly for the study of Li-containing compounds. These momentum widths were compared with a theoretical study of LiH and an early DINS examination of ^{7}Li, with the expected trend for Li momentum, and thus

kinetic energy being witnessed.

Chapter 4 concludes with a study of $Li(NH_3)_4$. This study is perhaps particularly interesting due the distinct *lack* of difference exhibited in the neutron Compton profiles and radial momentum distributions of each solid phase of $Li(NH_3)_4$. This is a compound of light elements, with high proton density, having multiple structural phases below 88.8 K yet demonstrating negligible change in the momentum distribution of the proton. Sadly, comparison with the proton momentum distribution of solid and liquid NH_3 cannot be made at this time. The anharmonic components of the neutron Compton profile for the proton in $Li(NH_3)_4$ are seen to lack an a_2 component, fitting well to a similar value for a_4 for each phase, which is likely a reflection of the increased electron density and absence of hydrogen bonding in the metal, as compared to that present in NH_3.

Certainly this distinctly odd result requires further verification, with a sample of $Li(NH_3)_4$ being prepared *in situ*, within a container capable of isolating the Li and N component of the scattering law. An examination of the liquid phase would enable a demonstration of how the intramolecular potential affects the proton dynamics in DINS.

6.2 The Dynamics of NH_3 at Low Concentration Within a Zeolite Host

Chapter 5 details a number of lower-energy neutron spectroscopic studies on NH_3 absorbed at low concentrations within zeolite NaA and CuA. At the level of loadings for these systems, between 3-4 molecules of NH_3 per unit cell (specifically α-cage) of the zeolite host.

INS measurements are presented for NH_3 within both NaA and CuA. In the case of NaA, the NH_3-weighted INS spectrum was seen to consist of three low energy regions: two broad collections of peaks with an interstitial sharp-peak feature. By modelling the system at the level of fully periodic density functional calculation, these low energy modes were assigned as translational, librational and a rocking displacement of the NH_3 molecule as it coordinates to a extra-framework Na-cation. The greatest discrepancy between calculation and measurement, considering the difficulty of DFT implementation for low-energy phonon calculation, was the intensity deficit in the librational region, which is discussed. In the case of CuA, measured INS spectra are compared with model calculations for NH_3 coordinated to separate Cu cations, or to the same Cu cation, with the remaining ligands provided by the zeolite framework. Agreement is seen to a far greater extent in the former case, for the system $Cu(NH_3)O_3{}^{zeolite}$ in a distorted tetrahedral geometry. The features in the measured INS have thus been assigned to stretching, bending, librational and tilting regions. Again, a deficit in the signal from the librational

mode is witnessed in the measured INS.

QENS measurements for the NaA·NH_3 system were detailed to investigate longer-timescale dynamics. Data were collected using the IRIS spectrometer in the temperature range 5-250 K, with subsequent fits being satisfactory for an elastic component and single quasielastic Lorentzian. Examination of the widths of these Lorentzians led to the conclusion that the single dynamical process examined was localised in nature, rather than diffusive. Temperatures above 150 K were used to demonstrate the Arrhenius nature of this process, with a resultant activation energy being thus determined. However, examination of the measured EISF for the system shows deviance from that of a 3-fold rotor, which combined with the low activation energy suggests an appreciable role in framework dynamics in mediating the NH_3 rotation.

6.3 Acta Est Fabula...[1]

The achievements of this thesis are varied, but of particular import in the eyes of the author is the work on DINS. There is great excitement in being involved in a technique that is constantly being redefined in terms of its place in the wider spectroscopic community, and any development that can be specifically targeted, such as the extension to heavier masses, is fascinating. The simple investigation of ^{7}LiF, for example, was particularly enlightening, with a number of subsequent

[1] Plaudite

studies being planned by both ourselves and collaborators in the field to further test the limits of sensitivity to Li in particular. As was stated in the introduction to this thesis, it is immensely satisfying to still be able to ask "what happens if we try *this*?", particularly when it then (surprisingly) works.

Bibliography

[1] M Mladenovic. *Institute of Physics Publishing*, The defining years in nuclear physics, 1932-1960s, 1998.

[2] *https* : *//www.nobelprize.org/nobel_prizes/physics/laureates/*1938/.

[3] *https* : *//www.nobelprize.org/nobel_prizes/physics/laureates/*1994/.

[4] SW Lovesey. *Oxford Scientific Publications*, Theory of Neutron Scattering from Condensed Matter, Volume 1, 1984.

[5] GL Squires. *Dover*, Introduction to the Theory of Thermal Neutron Scattering, 1978.

[6] DS Sivia. *Oxford University Press*, Elementary Scattering Theory, 2011.

[7] PCH Mitchell, SF Parker, AL Ramirez-Cuesta, and J Tomkinson. *World Scientific*, Vibrational spectroscopy with neutrons, 2005.

[8] *Figure adapted from that of D. Colognesi.*

[9] NIST Center for Neutron Research. *Neutron News Vol 3*, 3:29–37, 1992.

[10] CJ Carlile and M Prager. *Int. J. Modern Phys.*, 7:3113–3151, 1993.

[11] PC Hohenberg and PM Platzman. *Phys. Rev.*, 152:152, 1966.

[12] C Andreani, D Colognesi, J Mayers, GF Reiter, and R Senesi. *Adv. Phys.*, 54:377–469, 2005.

[13] C Andreani, C Pantalei, and R Senesi. *Phys. Rev. B*, 75:064515, 2007.

[14] RN Silver. *Phys. Rev. B*, 39:4022–4029, 1989.

[15] R Senesi, C Andreani, D Colognesi, and M Nardone. *Phys. Rev. Lett.*, 86:4584, 2001.

[16] R Senesi, C Andreani, AL Fielding, J Mayers, and WG Stirling. *Phys. Rev. B*, 68:214522, 2003.

[17] C Andreani, D Colognesi, and E Pace. *Phys. Rev. B*, 60:10008, 1999.

[18] CA Chatzidimitriou-Dreisman, T Abdul-Redah, and M Krzystyniak. *Phys. Rev. B*, 72:054123, 2005.

[19] A Giuliani, F Bruni, MA Ricci, and MA Adams. *Phys. Rev. Lett.*, 106:255502, 2011.

[20] C Pantalei, R Senesi, C Andreani, P Sozzani, A Comotti, S Bracca, M Beretta, PE Sokol, and GF Reiter. *Phys. Chem. Chem. Phys.*, 13:6022–6028, 2011.

[21] SE Pagnotta, F Bruni, R Senesi, and A Pietropaolo. *Biophys. J.*, 96:1939–1943, 2009.

[22] V Garbuio, C Andreani, S Imberti, A Pietropaolo, GF Reiter, R Senesi, and MA Ricci. *J. Chem. Phys.*, 127:154501, 2007.

[23] T Abdul-Redah, m Krzystyniak, and CA Chatzidimitriou-Dreismann. *Phys. Rev. B*, 72:052202, 2005.

[24] C Pantalei, A Pietropaolo, R Senesi, S Imberti, C Andreani, J Mayers, C Burnham, and G Reiter. *Phys. Rev. Lett.*, 100:177801, 2008.

[25] GF Reiter, JC Li, J Mayer, T Abdul-Redah, and P Platzman. *Brazil. J. Phys.*, 34:142–147, 2004.

[26] A Pietropaolo, R Senesi, C Andreani, A Botti, MA Ricci, and F Bruni. *Phys. Rev. Lett.*, 100:127802, 2008.

[27] A Pietropaolo, R Senesi, C Andreani, and J Mayers. *Brazil. J. Phys.*, 39:318–321, 2009.

[28] GF Reiter, AI Kolesnikov, SJ Paddison, PM Platzman, AP Moravsky, MA Adams, and J Mayers. *Phys. Rev. B*, 85:045403, 2012.

[29] V Garbuio, C Andreani, S Imberti, A Pietropaolo, GF Reiter, R Senesi, and MA Ricci. *J. Chem. Phys.*, 127:154501, 2007.

[30] G Reiter, C Burnham, D Homouz, PM Platzman, J Mayers, T Abdul-Redah, AP Moravsky, JC Li, CK Loong, and AI Kolesnikov. *Phys. Rev. Lett.*, 97:247801, 2006.

[31] GF Reiter, R Senesi, and J Mayers. *Phys. Rev. Lett.*, 105:148101, 2010.

[32] A Evans, J Mayers, and D Timms. *J. Phys. Condens. Matter*, 6:4197–4212, 1994.

[33] A Fulton, RA Cowley, and AC Evans. *J. Phys. Condens. Matter*, 6:2977–2984, 1994.

[34] I Peek, DA ad Fujita, MC Schmidt, and RO Simmons. *Phys. Rev. B*, 45:9680–9687, 1992.

[35] MP Paoli and RS Holt. *J. Phys. C; Solid State Phys.*, 21:3633–3639, 1988.

[36] D Colognesi, AJ Ramirez-Cuesta, M Zoppi, R Senesi, and T Abdul-Redah. *Physica B*, 350:e983–e986, 2004.

[37] AC Evans, DN Timms, J Mayers, and SM Bennington. *Phys. Rev. B*, 53:3023–3031, 1996.

[38] T Abdul-Redah, PA Georgiev, DK Ross, M Krzystyniak, and CA Chatzidimitriou-Dreisman. *J. Alloy. Compd.*, 404:787–789, 2005.

[39] D Colognesi, A Pietropaolo, R Senesi, and AJ Ramirez-Cuesta. *Phys. Rev. B.*, 76:174206, 2004.

[40] A Pietropaolo and R Senesi. *Nucl. Instrum. Meth. A*, 584:377–382, 2008.

[41] D Homouz, G Reiter, J Eckert, J Mayers, and R Blinc. *Phys. Rev. Lett*, 98:115502, 2007.

[42] GF Reiter, J Mayers, and J Noreland. *Phys. Rev. B*, 65:104305, 2004.

[43] L Kosidowski, AV Powell, and J Mayers. *Physica B*, 241:335–337, 1998.

[44] CA Chatzidimitriou-Dreisman, T Abdul Redah, RMF Streffer, and J Mayers. *Phys. Rev. Lett.*, 79(15):28394, 1997.

[45] T Abdul-Redah and CA Chatzidimitriou-Dreisman. *Physica B*, 350:e1035–e1–38, 2004.

[46] T Abdul-Redah, PA Georgiev, DK Ross, M Krzystyniak, DK Ross, and CA Chatzidimitriou-Dreisman. *Physica B*, 385:57–59, 2006.

[47] RA Cowley and J Mayers. *J. Phys. Condens. Matter*, 18:5291–5301, 2006.

[48] J Mayers and T Abdul-Redah. *J. Phys. Condens. Matter*, 16:4811–4832, 2004.

[49] EB Karlsson and SW Lovesey. *Phys. Rev. A*, 61:062714, 2000.

[50] EB Karlsson. *Phys. Rev. Lett.*, 90:095301, 2003.

[51] GF Reiter and PM Platzman. *Phys. Rev. B*, 71:054107, 2005.

[52] CS Cundy and PA Cox. *Chem. Rev.*, 103:663–701, 2003.

[53] DS Wragg, RE Morris, and AW Burton. *Chem. Mater.*, 20:1561–1570, 2008.

[54] C Baerlocher, WM Meier, and DH Olson. *Elsevier*, Complete atlas of zeolite framework types, 2007.

[55] C Baerlocher and McCusker. Database of Zeolite Structures: http://www.iza-structure.org/databases, 2011.

[56] C Martinez and A Corma. *Coord. Chem. Rev.*, 255:1558–1580, 2011.

[57] JH Li, HZ Chang, and L Ma. *Catal. Today*, 175:147–156, 2011.

[58] Z Wang, J Yu, and R Xu. *Chem. Soc. Rev.*, 41:1729–1741, 2012.

[59] C Marcilly. *J. Catal.*, 216(1-2):47–62, 2003.

[60] J Cejka, A Corma, and S Zones. *Zeolites and Catalysis, Vol. 2*, Wiley-VHC, 2010.

[61] W Grochala and PP Edwards. *Chem. Rev.*, 104:1283–1315, 2004.

[62] P Moriarty and D Honery. *Int. J. Hydrogen Energ.*, 34(1):31–39, 2009.

[63] RE Morris and PS Wheatley. *Angew. Chem. Int. Ed.*, 47(27):4966–4981, 2008.

[64] PA Anderson. Storage of hydrogen in zeolites. *Solid State Hydrogen Storage*, pages 223–260, 2008.

[65] PV Blarigan. *Hydrogen Program Reviews*, U.S. Dept. Energy technical report, 2000.

[66] M Bee. *IOP Publishing Ltd*, Quasielastic Neutron Scattering, 1987.

[67] GT Kokotailo, SL Lawton, DH Olson, and WM Meier. *Nature*, 272:437–438, 1978.

[68] H Jobic, M Bee, and GJ Kearley. *Zeolites*, 9:312–317, 1989.

[69] H Jobic, M Bee, and GJ Kearley. *Zeolites*, 12:146–151, 1992.

[70] LN Gergidis, DN Theodorou, and H Jobic. *J. Phys. Chem. B*, 104:5541–5552, 2000.

[71] ML Costenoble, WJ Mortier, and JB Uytterhoeven. *J. Chem. Soc. Faraday Trans.*, 72:1877–1883, 1976.

[72] DH Olson. *J. Phys. Chem.*, 74:2758–2764, 1970.

[73] I Deroche, G Maurin, BJ Borah, S Yashonath, and H Jobic. *J. Phys. Chem. C*, 114:5027–5034, 2010.

[74] E Pantatosaki, GK Papadopoulos, H Jobic, and DN Theodorou. *J. Phys. Chem. B*, 112:11708–11715, 2008.

[75] BJ Borah, H Jobic, and S Yashonath. *J. Chem. Phys.*, 132:144507, 2010.

[76] H Jobic, J Karger, and M Bee. *Phys. Rev. Lett.*, 82:4260–4263, 2008.

[77] D Blanchard, MD Riktor, JB Maronsson, HS Jacobsen, J Kehres, D Sveinbjornsson, EG Bardaji, A Leon, F Juranyi, J Wuttke, BC Haubeck, M Fichner, and T Vegge. *J. Phys. Chem. C*, 114:20249–20257, 2010.

[78] P Martelli, A Remhof, A Borgshulte, R Ackermann, T Strassle, JP Embs, M Ernst, M Matsuo, SI Orimo, and A Zuttel. *J. Phys. Chem. A*, 115:5329–5334, 2011.

[79] A Tekin, JS Hummelshoj, HS Jacob, D Sveinbjornsson, D Blanchard, JK Norskov, and T Vegge. *Energy Environ. Sci.*, 3:448–456, 2010.

[80] J Voss, Q Shi, HS Jacobsen, M Zamponi, K Lefmann, and T Vegge. *J. Phys. Chem. B*, 111:3886–3892, 2007.

[81] NJ Hess, MR Hartman, CM Brown, E Mamontov, A Karkamkar, DJ Heldebrant, LL Daemen, and T Autrey. *Chem. Phys. Lett.*, 459:85–88, 2008.

[82] AK Tripathi, A Sahasrabudhe, S Mitra, NM Mukhopadhyay R and, Gupta, and VB Kartha. *Phys. Chem. Chem. Phys.*, 3:4449–4455, 2001.

[83] AK Tripathi, A Sahasrabudhe, AK Tripathi, R Mukhopadhyay, and NM Gupta. *Phys. Chem. Chem. Phys.*, 5:3066–3075, 2003.

[84] E Kemner, IM de Schepper, AJM Schmets, H Grimm, AR Overweg, and RA can Santem. *J. Phys. Chem. B*, 104:1560–1562, 2000.

[85] R Mukhopadhyay, A Sayeed, S Mitra, AV Anil Kumar, MN Rao, S Yashonath, and SL Chaplot. *Phys. Rev. E*, 66:061201, 2002.

[86] VK Sharma, S Gautam, S Mitra, MN Rao, Tripathim AK, SL Chaplot, and R Mukhopadhyay. *J. Phys. Chem. B*, 113:8066–8072, 2009.

[87] BS Hudson. *Vib. Spectrosc.*, 42:25–32, 2006.

[88] SF Parker, SM Bennington, JW Taylor, H Herman, I Silverwood, P Albers, and K Refson. *Phys. Chem. Chem. Phys.*, 13:7789–7804, 2011.

[89] TJ Udovic, RR Cavanagh, JJ Rush, AJ Wax, GD Stucky, GA Jones, and DR Corbin. *J. Phys. Chem.*, 91:5968–5973, 1987.

[90] WPJH Jacobs, RA van Santen, and H Jobic. *J. Chem Soc. Faraday Trans.*, 90:1191–1996, 1994.

[91] TO Brun, LA Curtiss, LE Iton, P Kleb, JM Newsam, RA Bayerlein, and DEW Vaughan. *J. Am. Chem. Soc.*, 109:4118–4119, 1987.

[92] GN Greaves, F Meneau, O Majerus, DG Jones, and J Taylor. *Science*, 308:1299–1300, 2005.

[93] H Jobic. *Spectrochimica Acta.*, 48A:293–312, 1992.

[94] NW Ockwig, RT Cygan, MA Hartl, LL Daemen, and TM Nenoff. *J. Phys. Chem. C*, 112:13629–13634, 2008.

[95] C Corsaro, V Crupi, D Majolino, SF Parker, V Venuti, and U Wanderlingh. *J. Phys. Chem. A*, 110(3):1190–1195, 2006.

[96] H Jobic, A Tuel, M Krossener, and J Sauer. *J. Phys. Chem.*, 100:19545–19550, 1996.

[97] AJ Ramirez-Cuesta, PCH Mitchell, DK Ross, PA Georgiev, PA Anderson, HW Langmi, and D Book. *J. Mater. Chem.*, 17:2533–2539, 2007.

[98] PA Georgiev, A Albinati, BL Mojet, J Olivier, and E Juergen. *J. Am. Chem. Soc.*, 129:8086–8087, 2007.

[99] NT Cheok, FR Trouw, and LE Iton. *J. Phys. Chem. A*, 108:4737–4743, 2004.

[100] R Juarez, SF Parker, P Concepcion, A Corma, and H Garcia. *Chem. Sci.*, 1:731–738, 2010.

[101] IA Beta, J Herve, E Geidel, H Bohlig, and B Hunger. *Spectrochim. Acta A*, 57(7):1393–1403, 2001.

[102] R Schenkel, A Jentys, SF Parker, and JA Lercher. *J. Phys. Chem. B*, 108:7902–7910, 2004.

[103] AM Davidson, CF Mellot, J Eckert, and A Cheetham. *J. Phys. Chem. B*, 104:432–438, 2000.

[104] H Jobic, A Renouprez, A Fitch, and HJ Lauter. *J. Chem Soc. Faraday Trans.*, 83:3199–3205, 1987.

[105] H Jobic. *Chem. Phys. Lett.*, 170:217, 1990.

[106] R Hempelmann. *Oxford Science Publications*, Quasielastic Neutron Scattering and Solid State Diffusion, 2000.

[107] JJ Blostein, J Dawidowski, and JR Granada. *Phys. Rev. B*, 71:054105, 2005.

[108] D Colognesi, M Celli, F Ciloco, RJ Newport, SF Parker, V Rossi-Albertini, F Sacchetti, and J Tomkinson. *Appl. Phys. A*, 74:S64–S66, 2002.

[109] SF Parker. *J. Neutron Res.*, 10:173–177, 2010.

[110] KH Andersen. *Nucl. Instr. Methods A*, 371:472–479, 1995.

[111] CJ Carlile and MA Adams. *Physica B*, 182:431–440, 1992.

[112] J Mayers and MA Adams. *Rutherford-Appleton Laboratory Technical Report*, RAL-TR-2009-22, 2009.

[113] TB Reed and DW Breck. *J. Am. Chem. Soc.*, 78:5972–5977, 1956.

[114] W Lowenstein. *Am. Mineral.*, 39:92, 1954.

[115] JJ Pluth and JV Smith. *J. Am. Chem. Soc.*, 102:4704–4708, 1980.

[116] SM Seo, WT Lim, and K Seff. *J. Phys. Chem. C*, 116:963–974, 2012.

[117] AA Amaro and K Seff. *J. Phys. Chem.*, 77:906–910, 1973.

[118] RY Yanagida, AA Amaro, and K Seff. *J. Phys. Chem.*, 77:805–809, 1973.

[119] RY Yanagida and K Seff. *J. Phys. Chem.*, 77:138–139, 1973.

[120] F Weinhold and R West. *Organomettalics*, 30:5815–5824, 2011.

[121] JB Nicholas, EW Randall, RJ Harrison, LE Iton, LA Curtiss, and AJ Hopfinger. *J. Phys. Chem.*, 96:7958–7965, 1992.

[122] RW Thompson and MJ Huber. *J. Cryst. Gr.*, 56:711, 1982.

[123] GT Kerr. *Inorg. Chem.*, 5:1537, 1966.

[124] MW Anderson and L Kevan. *J. Phys. Chem.*, 91:4174–4179, 1987.

[125] JS Yu and L Kevan. *J. Phys. Chem.*, 98:12436–12441, 1994.

[126] PJ Carl, SL Baccam, and SC Larsen. *J. Phys. Chem. B*, 104:8848–8854, 2000.

[127] UD Joshi, PN Joshi, SS Tamhankar, VV Joshi, and VP Shiralkar. *J. Phys. Chem. B*, 105:10637–10647, 2001.

[128] CY Liu and K Aika. *J. Japan Petrol. Inst.*, 46:301–307, 2003.

[129] B Boddenberg, GU Rakmatkariev, A Wozniak, and S Hufnagel. *Phys. Chem. Chem. Phys.*, 6:2494–2501, 2004.

[130] V Kanazirev and N Borisova. *Zeolites*, 2(1):23–28, 1982.

[131] M Shatnawi, G Paglia, JL Dye, KC Cram, M Lefenfeld, and JL Billinge. *J. Am. Chem. Soc.*, 129:1386–1392, 2007.

[132] JL Dye, KC Cram, SA Urbin, MY Redko, JE Jackson, and M Lefenfeld. *J. Am. Chem. Soc.*, 127:9338–9339, 2005.

[133] A Sartbaeva, SA Wells, M Sommariva, MJT Lodge, MO Jones, AL Ramirez-Cuesta, G Li, and PP Edwards. *J. Cluster. Sci.*, 21:543–549, 2010.

[134] J Thewlis. *Acta. Crystallogr.*, 8:36–38, 1955.

[135] JC Thopson. *Electrons in Liquid Ammonia*, Clarendon Press, Oxford, 1976.

[136] E Zurek, PP Edwards, and Hoffmann R. *Angew. Int. Ed.*, 48:8198–8232, 2009.

[137] JL Dye. *Sci. Am.*, 237:92–105, 1977.

[138] PP Edwards. *J. Phys. Chem*, 84:1215–1230, 1980.

[139] PP Edwards. *J. Phys. Chem*, 84:3772–3780, 1984.

[140] K Maeda, MTJ Lodge, J Harmer, JH Freed, and PP Edwards. *J. Am. Chem. Soc.*, accepted for publication April 2012.

[141] E Zurek, XD Wen, and Hoffmann R. *J. Am. Chem. Soc.*, 133:3535–3547, 2011.

[142] H Thompson, JC Wasse, NT Skipper, CA Howard, DT Bowron, and AK Soper. *J. Phys. Condens. Matter*, 16:5639–5652, 2004.

[143] H Thompson, JC Wasse, NT Skipper, DT Hayama, S Bowron, and AK Soper. *J. Am. Chem. Soc.*, 125:2572–2581, 2003.

[144] S Hayama, NT Skipper, JC Wasse, and H Thompson. *J. Chem. Phys*, 116:2991–2996, 2002.

[145] N Mammano and MJ Sienko. *J. Am. Chem. Soc.*, 90:6322–6324, 1968.

[146] H Thompson, NT Skipper, JC Wasse, WS Howells, M Hamilton, and F Fernandez-Alonso. *J. Chem. Phys.*, 124:024501, 2006.

[147] RM Ibberson, AJ Fowkes, MJ Rosseinsky, WIF David, and PP Edwards. *Angew. Chem. Int. Ed.*, 48:1435–1438, 2009.

[148] J Mayers. *User guide to VESUVIO data analysis programs for powders and liquids*, Rutherford Appleton Laboratory.

[149] Windsor, Taylor, and Francis. *Pulsed Neutron Scattering*, London, 1981.

[150] R Senesi. *Nucl. Inst. Meth. A*, 661:70–76, 2012.

[151] M Krzystyniak, MA Adams, A Lovell, NT Skipper, SM Bennington, J Mayers, and F Fernandez-Alonso. *Faraday Discuss.*, 151:171–197, 2011.

[152] J Mayers, AL Fielding, and R Senesi. *Nucl. Inst. Meth. A*, 481:258, 2002.

[153] J Mayers. *Meas. Sci. Technol.*, 22:015903, 2011.

[154] J Mayers. *User guide to VESUVIO data analysis programs for powders and liquids.*, RAL Technical Reports:RAL:TR–2001–003, 2011.

[155] VF Sears. *Neutron News*, 3(3):29–37, 1992.

[156] M Krzystyniak and F Fernandez-Alonso. *Phys. Rev. B*, 83:134305, 2011.

[157] G Reiter. *Development Proposal for an Electron Volt Inelastic Spectrometer (ELVIS).*

[158] M Tardocchi, A Pietropaolo, R Senesi, C Andreani, and G Gorini. *Nucl. Inst. Meth. A*, 518:259–260, 2004.

[159] A Pietropaolo, C Andreani, M Rebai, L Giacomelli, G Gorini, E Perelli Cippo, M Tardocchi, A Fazzi, G Verona Rinati, C Verona, M Marinelli, E Milani, CD Frost, and EM Schooneveld. *Europhys. Lett.*, 94:62001, 2011.

[160] M Rebai, C Andreani, A Fazzi, CD Frost, L Giacomelli, G Gorini, E Milani, E Perelli Cippo, A Pietropaolo, G Prestopino, E Schooneveld, M Tardocchi, C Verona, and G Verona Rinati. *Nucl. Phys. B*, 215:313–315, 2011.

[161] JA Morrone and R Car. *Phys. Rev. Lett.*, 101:017801, 2008.

[162] Lin Lin, JA Morrone, R Car, and M Parrinello. *Phys. Rev. Lett.*, 105:110602, 2010.

[163] CA Chatzidimitriou-Dreismann, EA Gray, and TP Blach. *AIP Adv.*, 1:022118, 2011.

[164] J Mayers and GF Reiter. *AIP Adv.*, 1:049101, 2011.

[165] GP Holland and TM Alam. *Phys. Chem. Chem. Phys.*, 7(8):1739–1742, 2005.

[166] GP Holland, BR Cherry, and TM Alam. *J. Phys. Chem. B*, 108:16420–16426, 2011.

[167] D Biglino, R Erickson, A Lund, H Yahiro, and M Shiotani. *Phys. Chem. Chem. Phys.*, 1:2887–2896, 1999.

[168] RA Schoonheydt, P Peigneur, and JB Utterhoeven. *J. Chem. Soc. Faraday Trans.*, 12:2550–2561, 1989.

[169] RY Yanagida and K Seff. *J. Phys. Chem.*, 76(18):2597, 1972.

[170] RY Yanagida and K Seff. *J. Phys. Chem.*, 77(1):138–139, 1973.

[171] J Tomkinson. *Chem. Phys.*, 127:445–449, 1988.

[172] SF Parker, K Refson, RI Bewley, and G Dent. *J. Chem. Phys.*, 134:084503, 2011.

[173] AR Al Derzi, A Gregusova, K Runge, and RJ Bartlett. *Int. J. Quantum Chem.*, 108:2088–2096, 2008.

[174] G Poulet, P Sautet, and E Artacho. *Phys. Rev. B*, 68:075118, 2003.

[175] A Delabie, K Peirloot, MH Groothaert, BM Weckhuysen, and RA Schoonheydt. *Micropor. Mesopor. Mat.*, 37:209–222, 2000.

[176] SJ Clark, MD Segall, CJ Pickard, PJ Hasnip, MJ Probert, K Refson, and MC Payne. *Z. Kristallogr.*, 220(5-6):567–570, 2005.

[177] S Wells, M Dove, and M Tucker. *J. Appl. Crystallogr.*, 37:536–544, 2004.

[178] JP Perdew, K Burke, and M Ernzerhof. *Acd. Sym. Ser.*, 629:453–462, 1996.

[179] R Astala, SM Auerbach, and PA Monson. *J. Chem. Phys. B*, 108:9208–9215, 2004.

[180] AJ Ramirez-Cuesta. *Comput. Phys. Commun.*, 157(3):226–238, 2004.

[181] WS Howells, VG Sakai, F Demmel, MTF Telling, and F Fernandez-Alono. *The MODES User Guide v3*, RAL technical Reports, 2010.

[182] RT Azuah, LR Kreller, Y Qui, PLW Tregenna-Piggot, CM Brown, JRD Copley, and RM Dineo. *J. Res. Natl. Inst. Stan. Technol.*, 114:341, 2009.

[183] D Blanchard, JB Maronsson, MD Riktor, J Kheres, D Sveinbjörnsson, EG Bardaji, A Leon, F Juranyi, J Wuttke, K Lefmann, BC Haubeck, M Fichtner, and T Vegge. *J. Phys. Chem. C*, 116:2013–2023, 2011.

[184] A Orecchini, WC Pilgrim, C Petrillo, JB Suck, and F Sacchetti. *Condens. Matter Phys.*, 53:19–28, 2008.

[185] M Springborg. *Density-Functional Methods in Chemistry and Materials Science*, Wiley, 1997.

[186] W Koch and MC Holthausen. *A Chemist's Guide to Density Functional Theory*, Wiley-VCH, 2007.

[187] P Hohenberg and W Kohn. *Phys. Rev.*, 136:B864, 1964.

[188] W Kohn and LJ Sham. *Phys. Rev.*, 140:A1133, 1965.

Appendix A

Computational Details for Calculations of ^{7}LiF

Modelling of the ^{7}LiF system detailed in section 4.3 was performed by Dr. Michele Ceriotti. Calculations were performed using the QUANTUM ESPRESSO package, utilising DFT and DFPT under the quasiharmonic approximation.

A $4 \times 4 \times 4$ k-point grid and planewave cutoff of 200 Ry were used for Brillouin zone sampling, and normconserving pseudopotentials were used to describe the core F electrons in the system. Li 1s electrons were included explicitly. Vibrational density of states were computed by DFPT, evaluating the dynamical matrix over symmetry-independant points of an $8 \times 8 \times 8$ phonon wave-vector grid, subsequently Fourier-interpolated on a $50 \times 50 \times 50$ grid.

Interstingly, the local density approximation (LDA) was seen to outperform a generalised-gradient approximation functional (PBE), for both resultant structural data and vibrational density of states, shown in figure A.1

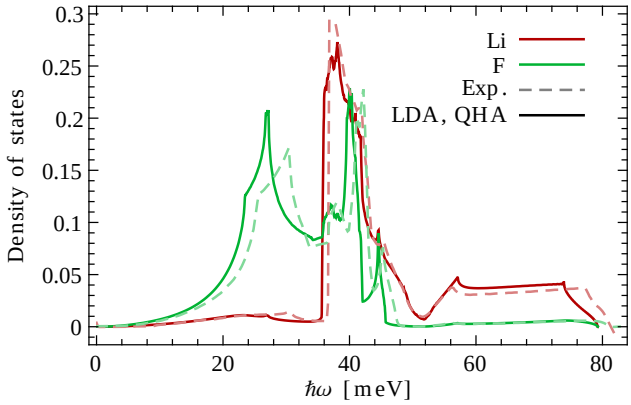

Figure A.1: Atom-projected DoS calculated within a quasiharmonic and local-density approximation (continuous lines), compared to neutron scattering experiment (dashed lines)

Momentum profile widths were then calculated by integration of the atom-projected DoS ($D_i[\omega, V_{eq}(T)]$) thus

$$\sigma_i^2 = \frac{m_i}{\hbar^2} \int D_i[\omega, V_{eq}(T)] \frac{\hbar\omega}{2} \coth \frac{\hbar\omega}{2k_B T} d\omega, \tag{A.1}$$

where $V_{eq}(T)$ is the temperature-dependant equilibrium volume computed within the quasiharmonic approximation.

Appendix B

Density Functional Theory

Density functional theory (DFT) has become a standard tool for the electronic modelling of condensed matter systems. The reader is referred to a number of references for the theoretical background and applications of DFT [185, 186], with a very brief comment on the theory behind model calculations in this thesis being reproduced here.

Fora system of N atoms and N_e electrons, the Schrödinger equation for eigenstates ψ_i is given by

$$\hat{H}\psi_i(\mathbf{r_1}, ..., \mathbf{r_N}, \mathbf{x_1}, ..., \mathbf{x_{Ne}}) = E_n\psi_i(\mathbf{r_1}, ..., \mathbf{r_N}, \mathbf{x_1}, ..., \mathbf{x_{Ne}}), \tag{B.1}$$

where E_n can be expressed within the frameworks of the Born-Oppenheimer approximation and DFT as a functional dependant on electron density, n, alone

$$E[n] = K[n] + E_{ee}[n] + \int d\mathbf{x} V_{ext}(\mathbf{x}) n(\mathbf{x}) + V_{nn}, \tag{B.2}$$

where $K[n]$ and $E_{ee}[n]$ are the kinetic energy and electron-electron interaction energies respectivey. These are dependant solely on the electron density, and not to the external potential V_{ext} experienced by the electron. $K[n]$ and $E_{ee}[n]$ are thus universal, but unknown. V_{nn} and the integral term in equation (B.2) define the nuclear coulombic term (constant in the BO approximation) and nucleus-electron interaction.

Hohenberg and Kohn showed, in two theorems [187], that electron density maps directly only a single Hamiltonian, and that the ground-state electron density $n_0(\mathbf{x})$ for a given V_{ext} minimises the total energy functional. $n_0(\mathbf{x})$ determines *all* ground state properties of the system.

The kinetic energy term in equation (B.2) is for a correlated electron density, but can be separated into a term for an non-interactive system, $K_{KS}[n]$ and a further term given by $(K[n] - K_{KS}[n])$. Likewise, $E_{ee}[n]$ can be separated into a Hartree term, $E_J[n]$ and exchange term $(E_J[n] - E_J[ee])$. Since $K_{KS}[n]$ and $E_J[n]$ can be known exactly, the remaining, unknown terms are collected together to define an exchange-correlaction functional, $E_{XC}[n]$.

$$E[n] = K_{KS}[n] + E_J[n] + E_{XC}[n] + \int d\mathbf{x} V_{ext}(\mathbf{x}) n(\mathbf{x}) + V_{nn}. \tag{B.3}$$

The Kohn-Sham approach [188] to the above is to apply the variational principle, using non-interaction orbitals, ϕ_i, and an external potential such that

$$n(\mathbf{x}) = \sum_{i}^{N_e} \phi_i * (\mathbf{x})\phi_i(\mathbf{x}) = n_0(\mathbf{x}). \tag{B.4}$$

In this manner it can be shown that

$$\begin{aligned} -\frac{1}{2} \bigtriangledown_i^2 \phi_i + (V_J + V_{ext} + V_{XC})\phi_i &= \epsilon_i \phi_i \\ -\frac{1}{2} \bigtriangledown_i^2 \phi_i + V_{eff}\phi_i &= \epsilon_i \phi_i. \end{aligned} \tag{B.5}$$

From the above it can be seen that these single-particle equations contain one unknown, the exchange-correlation functional, and is dependant on the electron density. The Kohn-Sham equations must therefore be solved iteratively.

The forms of $E_{ext}[n]$ (explicitly $\int d(\mathbf{x})n(\mathbf{x})V_{XC}(\mathbf{x}, n)$) is of paramount importance in the application of DFT, and formalisations range from that of a truly local density approximation (LDA) through generalised-gradient (GGA) and hybrid forms [178].

Periodic systems contain translational symmetry, where the application of a translational operator $\hat{T}_i$ on ϕ_i yields, by the application of Bloch's theorem, the Kohn-Sham orbitals of a periodic supercell

$$\phi_{i\mathbf{k}}(\mathbf{x}) = e^{(2\pi i k_i)} u_{i\mathbf{k}}(\mathbf{x}), \tag{B.6}$$

where the function $u_{i\mathbf{k}}(\mathbf{x})$ has the periodicity of the lattice. Thus it can be shown that for a periodic system, equation (B.5) becomes

$$-\frac{1}{2}(\bigtriangledown_i + i\mathbf{k})^2 u_{i\mathbf{k}}(\mathbf{x}) + V_{eff} u_{i\mathbf{k}}(\mathbf{x}) = \epsilon_i u_{i\mathbf{k}}(\mathbf{x}). \tag{B.7}$$

The application of DFT for a periodic system is undertaken in reciprocal space, and the Kohn-Sham equations are thus a Fourier transform of the above equation (B.7). The resulting formalism is not reproduced here, as it is sufficient to state that due to this transform, the basis-functions for solving the Kohn-Sham equations are a set of plane-waves such that

$$u_{i\mathbf{k}}(\mathbf{x}) = \sum_{\mathbf{G}}^{|\mathbf{G}|\langle G} u_{i\mathbf{k}}(\mathbf{G}) e^{2\pi i \mathbf{G}\cdot\mathbf{x}}, \tag{B.8}$$

where $\mathbf{G}$ is the reciprocal lattice vector, the magnitude of which relates to the cutoff energy of the plane-wave basis set such that $|\mathbf{G}| < \sqrt{2E_{cut}}$.

For the mathematical machinery ingrained within any program designed for DFT calculations, the reader is referred to the specific documentations (for this thesis, the CASTEP program is used [176]). Calculations follow the approach of initial geometric optimisation of the system, whereby the atomic coordinates are allowed to vary to minimise the energy of the system

$$\frac{\delta E}{\delta \mathbf{r_i}} = -\mathbf{F_i} = 0, \tag{B.9}$$

where

$$\mathbf{F}_i = \left\langle \phi_0 \left| \frac{\delta}{\delta \mathbf{r_i}} \hat{H} \right| \phi_0 \right\rangle, \tag{B.10}$$

i.e. the atomic forces must equal zero for each atomic species i in equilibrium.

The normal mode displacement vectors, $\mathbf{u}$ for a harmonic system can be determined from the second derivative of the energy, or the second term in a taylor expansion given by

$$E(\mathbf{u}_1 ... N) = \frac{1}{2} \sum_{ij} \left(\frac{\delta^2 E}{\delta \mathbf{u_i} \otimes \delta \mathbf{u_j}} \right) \mathbf{u_i} \cdot \mathbf{u}_j = \frac{1}{2} \sum_{ij} k_{ij} \mathbf{u_i} \cdot \mathbf{u}_j, \tag{B.11}$$

where the force constant matrices can be computed directly in the finite-displacement method as implemented in CASTEP.

Appendix C

Papers Currently Published From This Work

To date, three papers from the work detailed in this thesis have been submitted for publication in peer-reviewed journals. These are included in this appendix, and in reverse chronological order are:

- A.G. Seel, M.Ceriotti, J.Mayers and P.P.Edwards; *J. Phys. Condens. Matter* Accepted July 2012
- A.G. Seel, A.Sartbaeva, J.Mayers, A.J.Ramirez-Cuesta and P.P.Edwards; *J. Chem. Phys.*; **134**; 114511 (2011)
- A.G.Seel, A.Sartbaeva, A.J.Ramirez-Cuesta and P.P.Edwards; *Phys. Chem. Chem. Phys.*; **12** (33); 9661-9666 (2010)

Appendix D

And Then We Danced...

No science is undertaken without a constant stream of music, be it for data collection, analysis or merely for inspiration (a kind of auditory-pseudopotential above which the process of turning caffein into knowledge is much expedited). As such, there are listed here a few tracks in particular that have aided the work detailed in this thesis.

- Chapter 1
  - *Toyah* - Jungles of Jupiter
  - *Amanda Palmer* - Guitar Hero
  - *The Visions Bleak* - Kutulu!
- Chapter 2
  - *VNV Nation* - Space & Time
  - *Siouxsie and the Banshees* - Icon
  - *Tarja* - I Feel Immortal
- Chapter 3
  - *Nina Hagen* - Born in Xixax

  - *Peter Murphy* - The Prince & Old Lady Shade
  - *Rammstein* - Haifisch

- Chapter 4
  - *Mind.In.A.Box* - The Last Ninja
  - *Blutengel* - Reich Mir die Hand
  - *VNV Nation* - In Defiance

- Chapter 5
  - *Siouxsie and the Banshees* - Love Out Me
  - *Dreadful Shadows* - Beyond the Maze
  - *Die Apokalyptischen Reiter* - Hammer Oder Amboss

- Chapter 6
  - *Toyah* - Angel & Me
  - *Siouxsie and the Banshees* - Silver Waterfalls
  - *Nina Hagen* - My Way

Working as a researcher and continuing to study science is a truly wonderful way to spend time. Being allowed to keep this appendix as part of a DPhil thesis is a suitable reflection of the last 4 years of preparing this document, and can only be described as freaking awesome.

\m/